University of Nevada, Reno

# Dynamic atmospheric signal analysis for improving mine safety and health

A dissertation submitted in partial fulfillment of the requirements for the degree of

Doctor of Philosophy in Geo-engineering

by

William Kofi Asante

Dr. George Danko/Dissertation Advisor

August, 2017

THE GRADUATE SCHOOL

We recommend that the dissertation
prepared under our supervision by

**WILLIAM KOFI ASANTE**

entitled

**Dynamic atmospheric signal analysis for improving mine safety and health**

be accepted in partial fulfillment of the
requirements for the degree of

DOCTOR OF PHILOSOPHY

George Danko, Ph.D., Advisor

Charles Kocsis, Ph.D., Committee Member

Matteo Aureli, Ph.D., Committee Member

Javad Sattarvand. Ph.D., Committee Member

Robert Watters, Ph.D., Graduate School Representative

David W. Zeh, Ph. D., Dean, Graduate School

August, 2017

## Abstract

There are a number of contaminants generated from strata and equipment usage in underground mines including poisonous and combustible gases, as well as heat. Mine ventilation is utilized to dilute the gases and cool the mine to provide conducive environment for mine workers. In order to ensure that contaminant levels are within acceptable regulatory limits, various sensors are installed in strategic places in the mine for monitoring.

Continuous atmospheric monitoring is one of the tools used to achieve health and safety limit compliance and to ensure the quality of air conditions in underground mines. It is challenging to interpret monitoring sensor signal for accident prevention due to different contributing factors. The possibility of contaminant accumulation can be dangerously high as the concentration pulse traveling in the air moves from one location to another. This can be attributed to the inherent delay processes associated with the concentration pulse as it travels with the air velocity. As such, the identification of the delay hazard processes is of prime importance in predicting and preventing any future contaminant concentration increase in the traveling front.

An increase of hazardous contaminant concentrations can be predicted by signal pattern recognition, root-cause analysis of rapid changes toward deterioration and forward prediction in time using algorithms and numerical models. This study focuses on analyzing signal patterns to recognize dangerous trends due to delayed processes by predicting contaminant concentrations for safety checking in underground mines. Efficient numerical ventilation model with contaminant simulation components is needed for the analysis of

real-time atmospheric monitoring data. Examples of signal analysis and forward prediction of concentration are demonstrated in mine examples and the new results are presented for the application to improve mine safety and health.

## Dedication

To my family.

## Acknowledgements

I would like to express my deepest gratitude to my advisor Dr. George Danko for his guidance and support during the course of my study. I am also, very grateful to Dr. Javad Sattarvand, Dr. Matteo Aureli, Dr. Charles Kocsis, and Dr. Robert Watters for serving on my committee and providing me with very valuable comments. The support from Dr. Davood Bahrami for software applications is much appreciated.

The research funds from Alpha foundation, USA and NIOSH, USA, is gratefully acknowledged.

# Table of Contents

# List of Tables

# List of Figures

## List of Acronyms and Symbols

| | |
|---|---|
| AMS: | Atmospheric Monitoring System |
| APPS: | Air Parameter Predictor Simulator |
| BC: | Boundary Condition |
| CFD: | Computational Fluid Dynamics |
| CFR | Code of Federal Regulation |
| CWA | Cycle weighted average |
| EWP: | Early Warning Predictor |
| EWS: | Early Warning System |
| GUI: | Graphical User Interface |
| LHD | Load haul dump |
| LS | Left side |
| MF: | MULTIFLUX |
| MPD: | Mine Production Data |
| NIOSH: | National Institute for Occupational Safety and Health |
| NTCF: | Numeral Transport Code Functionalization |
| PMHC | Porous-Media Hydrothermal Code |
| ppm | Part Per Million |
| RMS: | Root Mean Square |
| RS | Right side |
| RSM: | Roof Stability Monitoring |
| RPM | Revolution per minute |
| SFST | State-flux, space-time |
| SME: | Society of Mining and Metallurgical Engineers |
| STEL | Short term exposure limit |
| TLV | Threshold limit value |
| TWA | Time weighted average |
| VAM: | Ventilation Air Model |
| VOD: | Ventilation On Demand |
| DPM | Diesel Particulate matter |
| fpm | Feet per minute |
| $\mu g/m^3$ | Microgram per meter cube |
| µg/kg/s | Microgram per kilogram per second |
| kg/hr | Kilogram per hour |
| $D$ | Dispersion coefficient |
| ft | Feet |
| $L$ | Length |
| $m$ | meter |

| | |
|---|---|
| $s$ | second |
| $t$ | time |
| $v_{air}$ | Travel velocity of air |
| $v_{LHD}$ | Travel velocity of LHD machine |
| $x$ | Distance |
| $\Delta x$ | Change in distance |

# 1.0 Chapter 1 - General Introduction

## 1.1 Introduction

Atmospheric Monitoring Sensors (AMS) are utilized by modern underground mines for evaluating compliance with regulatory limits for critical air parameters such as hazardous concentrations of gas pollutants, particulate contaminants (dust or diesel particulate matter), and climatic properties (velocity, airflow, barometric pressure, temperature, relative humidity, and density). It is important to recognize hazardous conditions to mine safety in time before the advancement into a safety or health hazard or even an accident. The role of mine monitoring systems in problem recognition is very important. However, there are certain safety hazardous conditions that may cause a delayed increase in contaminant concentration levels and recognition of such hazards from the sensors is difficult because of the complex and dynamic nature of the information from atmospheric monitored data.

It is difficult to foresee the possible outcomes of intertwined signatures of various problems by continuous human observation. For instance, a sudden drop in barometric pressure from a monitoring sensor may induce continuous methane from the gob. Such a situation could be problematic in future time (Danko et al., 2013). Time-dependent models can be used to predict the concentrations due to barometric pressure variations. As a results, several concepts have emerged to analyze atmospheric signals for safety checking. Statistical analysis has been used to access the influence of barometric pressure changes on ventilation conditions in deep mines in Poland using a two year continuously measured barometric pressure data (Wasilewski, 2014). It was concluded from the study that methane

concentrations changed significantly due to pressure changes. Also, principle component analysis (PCA) and artificial neural network (ANN)-based models is used to predict the ventilation methane emission rates of U.S. longwall mines (Karacan, 2008).

A calibrated ventilation air model can be used to predict a likely methane concentration variation in future time as a function of previous and new air pressure as well as air velocity (Danko, et. al., 2013). Also, gob breathing induced barometric pressure fluctuations have been studied using computational fluid dynamics (Lolon et al, 2016). The results showed that barometric pressure directly affected methane inflow from the gob which helped in assessing the methane ignition and explosion risks related to atmospheric pressure changes. Such a future trend, however, cannot be seen from the raw measurement data. Belle evaluated the effect of daily barometric pressure changes on longwall tailgate gas levels using a gas mass balance model and measurement data (Belle, 2014). Therefore, time-dependent variations of contaminant concentrations from measurement data require continuous evaluation for the recognition of problem causing trends.

The focus of this study is mine safety improvement, by recognizing the emergence of safety hazards through numerical modeling techniques for supporting ventilation management in mitigating such hazardous causes and avoiding disaster.

A new concept of applying ventilation and contaminant transport models to support mine ventilation management in recognizing warning trends was studied in a research project supported by the Alpha foundation (Danko et al, 2016). As part of this project, my research work encompassed hazardous scenario identification and critical analysis of the dynamic signature of contaminant concentrations by simulations, interpretation of the monitored signal anomaly, relating it to a root cause as a boundary condition, predicting

concentrations from that cause and finally establishing the gain time for issuing an early warning. A system is developed to pick up the warning signals and make a predictive forecast. An Early Warning Predictor (EWP) is developed to provide effective recognition of a hazardous condition during its evolution; and to signal for preventive actions without delay for effective resolution of the hazardous scenario. The hazardous condition is checked and the accident scenario is evaluated during its evolution to display a warning for preventive measure before a potential accident occurs in order to avoid it.

Safety improvement can be achieved by the recognition of early trends that indicate potential safety hazards. This may provide the time for putting adequate measures in place in response to signal trends that could lead to an accident. The study of past mine accident scenarios related to mine ventilation (Page, et.al, 2012), shows that the accidents were preventable. However, recognition of early trends in time can be used as a tool for preventing such accidents. This will help in addressing the complex problem of recognizing safety hazards from a raw measurement data for accident prevention.

Another example of underground mine contaminant that adversely affects human health and safety is diesel particulate matter (DPM), which is termed as a human "carcinogen" by the World Health Organization (WHO, 1996), National Institute of Occupational Health and Safety (NIOSH, 1988), International Agency for Research on Cancer (IARC, 1989 and 2012), and National Toxicology Program (NTP, 2000 and 2011). Various monitoring sensors of DPM by direct measurements in underground mines are available. However, capturing the true time-integral of contaminant concentration by sensors can be challenging due to the complex and dynamic nature of diesel exhaust emission transport as well as the concentration variation around a moving machine (Asante, 2014). The method of

determining the actual mine worker's exposure to DPM concentration by direct atmospheric measurement is expensive and retroactive. Alternatively, a mine verification model may be used to evaluate the average concentration exposure value of the DPM for compliance analysis without real-time, complicated DPM measurements, relying basically on tailpipe smog test, fuel consumption and a contaminant transport model, incorporated in the mine ventilation model (Asante, 2014; Danko, 2016; Danko and Asante, 2017).

As part of the dynamic atmospheric signal interpretation for checking safety, diesel emission variation is studied both experimentally and numerically in a ventilated underground working area with a moving loader machine.

### 1.2 Delayed hazard mechanisms

Figure 1-1 depicts a delayed hazard mechanism of methane ($CH_4$) concentration pulse traveling from location 1 to location 2 in an airway (Danko et al, 2016). The methane concentration at location 2 is expected to be lower than in location 1 caused by advection-diffusion as the pulse travels with the air velocity, shown in Figure 1-1(a). Therefore, if the concentration at location 1 is not dangerous, likewise will be the concentration at location 2. If the traveling concentration front encounters another concentration build up from a distributed source, it leads to gas accumulation hazard with delay time that may cross the threshold, shown in Figure1-1(b). A simple summation of the concentrations values from two or three distributed sources can be performed to determine the concentration build up at a downstream location. A model will be required to analyze this occurrence automatically at any time, running as a real-time simulator. Delayed mechanisms in a mine may be caused by numerous distributed sources with different airflows and velocities

which may contribute to gas accumulation at a downstream location. Therefore, the mixing equation becomes more complex beyond a simple summation and as such it is necessary to have a calibrated, mine-wide numerical model capable of handling such scenarios.

Another delayed mechanism is shown in Figure 1-2 depicting methane inflow from the gob into the airway associated with a response delay as a result of pressure-driven methane liberation (Danko et al, 2016). Although no problem may be caused by methane release due to slow barometric pressure changes under normal weather conditions, sudden change may induce methane from the gob into the airway as demonstrated by numerical studies (Danko and Bahrami, 2014). Gas concentrations in the mine airway always change and these changes are related to different disturbances. These changing concentration values might soon reach a threshold limit value. Therefore, a concentration value at a monitored location might not be critical but build-up at other locations may become critical. This will lead to a threshold value crossing at a different location other than the monitored location. Threshold crossing may be due to the continuous downstream addition of concentration to the increasing level as a result of cascading. As such, changes which trigger continuous increase of gas level with a time delay must be modeled caused by e.g., sudden gas in burst, roof collapse, fan malfunctioning, barometric pressure changes and fire load. Only a mine-wide verification model can determine how the dynamic signature of gas concentration is affected in the mine airway.

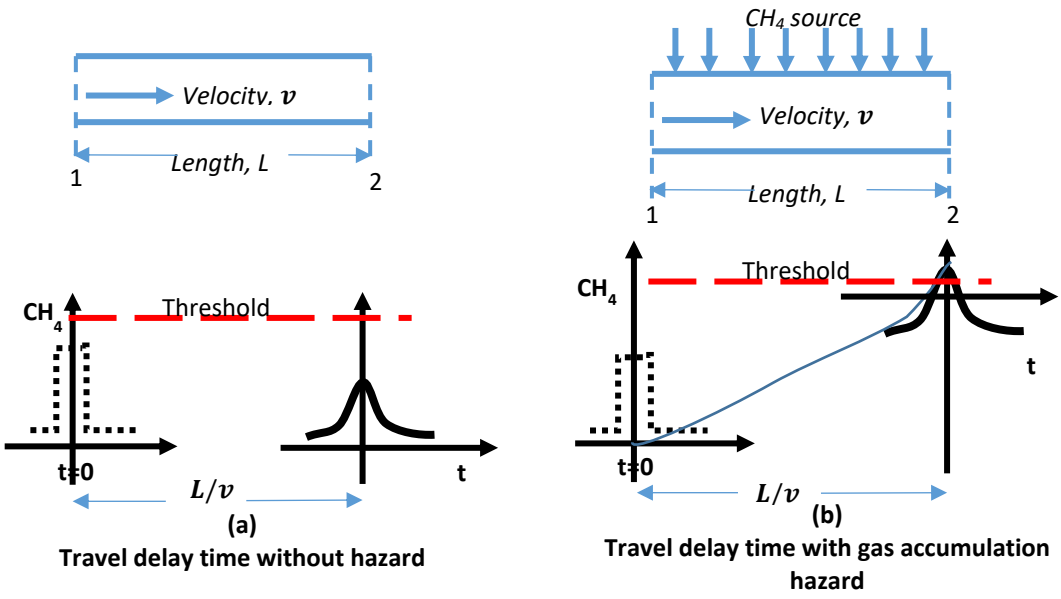


Figure 1-1. Methane concentration pulse with (a) travel delay time without hazard and (b) travel delay time with gas accumulation hazard.

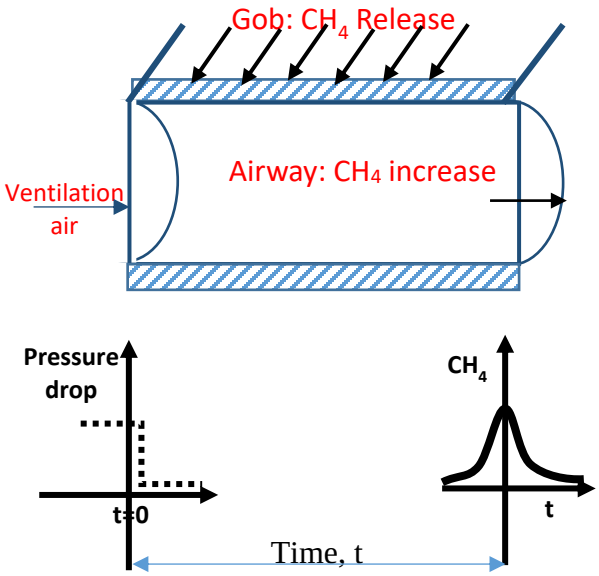


Figure 1-2. Pressure drop induces methane inflow from gob into airway showing response delay.

### 1.3 Problem statement

Contaminants that are generated from the strata and equipment usage in underground mines include poisonous gases, combustible gases, dust, diesel particulate matter (DPM) and heat. Mine ventilation is utilized to dilute the gases and cool the mine to provide conducive environment for mine workers. Modern underground mines are equipped with Atmospheric Monitoring Sensors (AMS) for evaluating compliance with regulatory limits for critical air parameters such as hazardous concentrations of gas pollutants, dust, or climatic properties. Recognition of hazardous conditions to health in mines is of prime importance for the well-being of the workers. Furthermore, it is important to recognize hazardous conditions to mine safety in time before they evolve into an accident. Mine monitoring has been widely used for these tasks with increasing success. Problem identification plays a significant role in using the data from the monitoring system of a mine.

Retrospective analysis and evaluation of atmospheric parameters is utilized for checking compliance with mine safety regulations. However, changes in the mining and ventilation conditions and parameters may present hazardous transient scenarios that require immediate preventive actions. Current atmospheric monitoring and evaluation practices regarding the ventilation network data are mainly retrospective and lack forecasting evaluation capabilities such as identifying scenarios that may lead to an accident. Three problems arise:

a. Dangerous locations may not be monitored
b. A detected cause may trigger a delayed hazardous effect

c. Dangerous trends with hidden consequence must be recognized before they may cause an accident

### 1.4 Hypotheses

Delayed hazard mechanisms associated with the ore body, mining operation, and the transport processes of mine ventilation may cause hazardous conditions in the mine. There is a delay time in each hazardous situation that can be used to prevent a potential safety hazard. If the hazardous situation is identified in advance from the atmospheric sensor data through signal analysis and a forward predictive model, a possible early warning signal can be issued before the evolution of a hazardous scenario into an accident.

### 1.5 Objectives

a. To analyze signal patterns from real-time dynamic atmospheric monitoring data using numerical ventilation model with contaminant simulation components.
b. To recognize dangerous trends caused by contaminant accumulation as a result of delay hazard mechanisms as well as to forward predict the critical parameters that may affect mine safety.
c. To identify the delay time required to prevent potential safety and health hazards in a dynamic mining environment from the combination of monitored and simulated data.
d. To apply a ventilation and contaminant transport models to support mine management in recognizing early warning trends and provide a warning signal for flagging imminent or near-future safety hazards.

## 2.0 Chapter 2- Literature Review

Health and safety of underground mine workers have become paramount in modern mining operations. Different poisonous gases, pollutants, dust, DPM, heat and hazardous climatic conditions underground present threats to the safety and health of miners. Various health diseases and safety conditions are associated with these contaminants. There are a number of migration controls that are implemented to reduce the exposure of mine workers to such contaminants. These include engineering controls, management and administrative controls, work practices, and monitoring. Also, different regulatory limits for these contaminants are to the maintained by underground mines to limit over exposure by miners. In order to ensure compliance to the regulatory limits, monitoring sensors are strategically installed at critical locations to check the concentration levels of the contaminants in the mine.

### 2.1 Mine contaminants in underground mines

Hazardous gases in the ventilating air include carbon monoxide, carbon dioxide, oxides of nitrogen, sulfur dioxide, hydrogen sulphide and methane. Exhaust fumes are especially hazardous from diesel engines in underground mines. Modern mechanized mines increasingly use diesel equipment producing CO, $CO_2$, $NO_x$, and DPM. Other sources of mine gases include emission from the strata, oxidation, fire, explosion, blasting and human respiration. Coal mines may liberate methane from the deposit, one of the most hazardous to mine safety; coal dust, dangerous to mine blast and fires; and silica dust, dangerous to respiratory health.

## 2.2 Safety and health effects of underground mine contaminants

### 2.2.1 Carbon dioxide ($CO_2$)

Carbon dioxide gas is mostly found on the floor of underground environment as a result of its higher density (1.805 kg/$m^3$) than that of air (1.2 kg/$m^3$). The physiological effect of $CO_2$ on mine workers varies depending on the concentration level as determined by (Strang and MacKenzie-Wood, 1985) as shown in Table 2-1.

Table 2-1. Physiological effects of carbon dioxide (McPherson, 1993)

| Percent carbon dioxide in air | Effects |
|---|---|
| 0.037 – 0.038 | None, normal concentration of carbon dioxide in air. |
| 0.5 | Lung ventilation increased by 5 percent |
| 2.0 | Lung ventilation increased by 50 percent |
| 3.0 | Lung ventilation doubled, panting on exertion |
| 5 to 10 | Violent panting leading to fatigue from exhaustion, headache |
| 10 to 15 | Intolerable panting, severe headache, rapid exhaustion and collapse |

### 2.2.2 Carbon monoxide (CO)

Carbon monoxide is a mine contaminant gas that is colorless, odorless, tasteless, and highly toxic. With its density (1.149 kg/$m^3$) almost the same as air (1.2 kg/$m^3$), CO mixes well with air making it a very dangerous gas. Carbon monoxide existence in the blood stream forms a stable substance known as carbonoxyhaemoglobin (COHb). Different concentration levels of COHb in the blood stream have different physiological effect on the mine worker due to its difficulty in decomposition (McPherson, 1993), depicted in Figure 2-1.

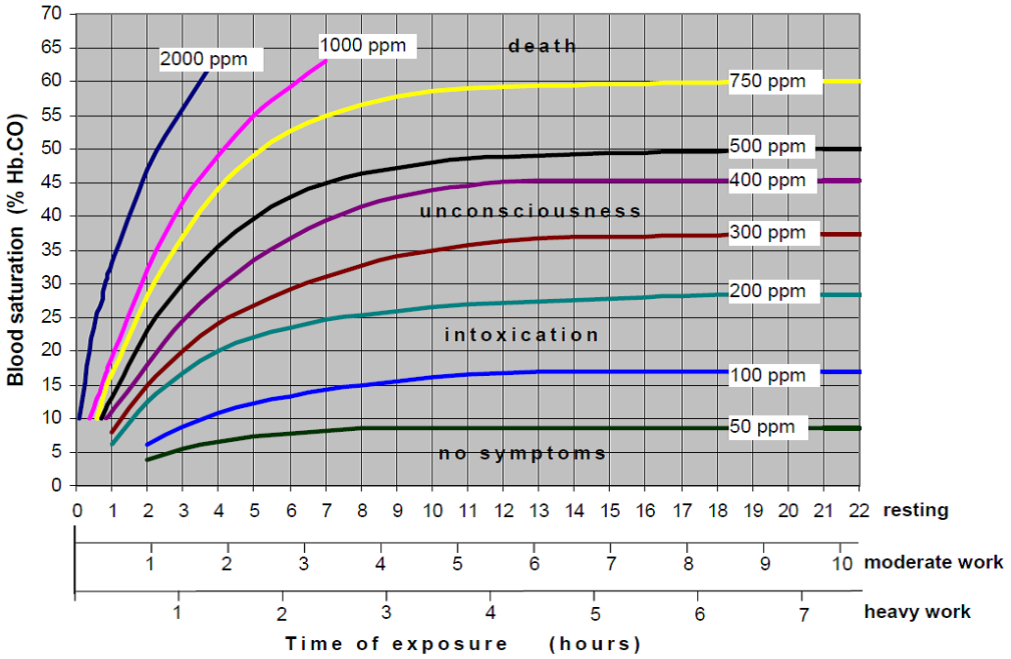


Figure 2-1. Physiological effects of carbon monoxide developed from Strang and Wood, 1985 (McPherson, 1993).

### 2.2.3 Sulphur dioxide ($SO_2$)

Sulphur dioxide gas is colorless and nonflammable. It is formed by the combustion of sulphur compounds (Hartman et al, 1997). It has a burning sensation and acidic taste, making it easy to detect by mine workers. It is a highly toxic gas in underground mines and its physiological effect on worker is presented in Table 2-2.

Table 2-2. Physiological effects of sulphur dioxide (McPherson, 1993)

| Concentration of sulphur dioxide ppm | Effects |
|---|---|
| 1 | Acidic taste |
| 3 | Detectable by odor |
| 20 | Irritation of eyes and respiratory system |
| 50 | Severe burning sensation in eyes, nose and throat. |
| 400 | Immediately dangerous to life. |

### 2.2.4 Oxides of nitrogen (NOx)

Oxides of nitrogen are formed during blasting and diesel combustion which can be very toxic. Nitric oxide (NO), nitrous oxide ($N_2O$), and nitrogen dioxide ($NO_2$) are the most predominant ones. The exposure effects of oxides of nitrogen are depicted in Table 2-3.

Table 2-3. Exposure effects of oxides of nitrogen (Hartman et al, 1997)

| Concentration ppm | Effects |
|---|---|
| 3 | Current threshold limit value – time weighted average (TLV-TWA) |
| 60 | Least amount causing immediate throat irritation |
| 100 | Least amount causing coughing |
| 100-500 | Dangerous even for short exposure |
| 200-700 | Rapidly fatal |

### 2.2.4 Hydrogen sulphide ($H_2S$)

Hydrogen sulphide gas has a rotten egg smell making it easily detectable. It is highly toxic formed from decomposition of sulphur compounds. The physiological effects of exposure to this gas is shown in Table 2-4.

Table 2-4. Exposure effects of hydrogen sulphide (Hartman et al, 1997)

| Concentration | Symptoms |
|---|---|
| 0.025 ppm | Threshold of odor |
| 0.005-0.010% | Slight symptoms such as eye and respiratory-tract irritation after 1 hour |
| 0.010% | Loss of odor after 15 minutes exposure |
| 0.02-0.07% | Increase eye irritation, headache, dizziness, nausea, dryness, and pain in nose, throat, and chest |
| 0.07-0.10% | Unconsciousness, cessation of respiration and death |
| 0.10% | Death in a few minutes |

### 2.2.5 Methane

Methane is a nontoxic and highly flammable gas mostly found in coal mines with evidence of it also in some noncoal mines. Methane is lighter than air and this causes it to accumulate along the roof in the mine. The high flammability of methane makes it prone to catching fires and explosion in mines. The explosive range of methane is 5-15% with a minimum oxygen requirement of 12% (Hartman et al, 1997). Past events and accidents show that methane explosion can be very dangerous and devastating. There have been 10,419 fatalities resulting from 421 methane gas explosions in U.S underground coal mines from 1900-2012 (Griffin, 2013). Figure 2-2 demonstrates the fatalities and explosions from 1978-2012 (Griffin, 2013).

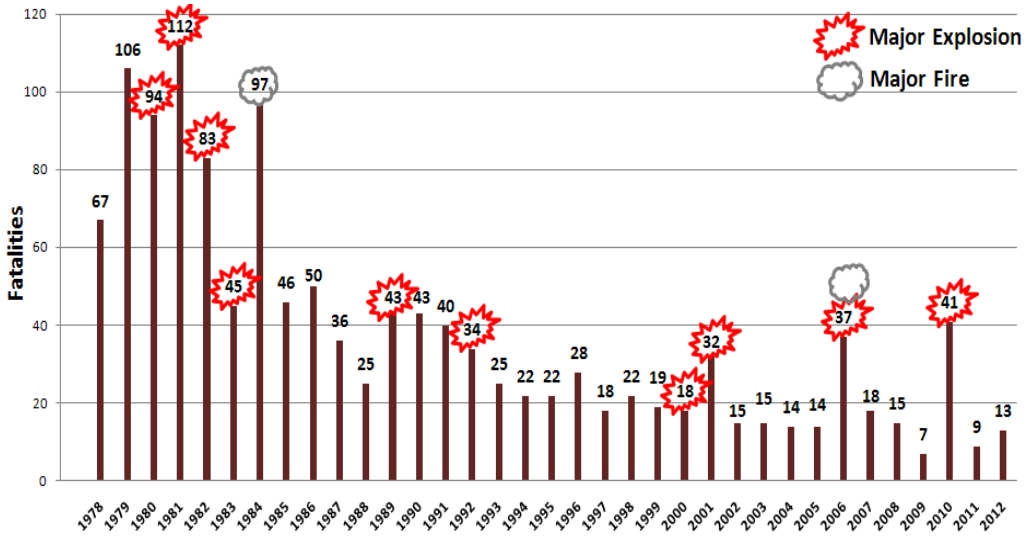


Figure 2-2 United States Underground Coal Mines Fatalities (Griffin, 2013)

#### 2.2.5.1 Effects of barometric pressure variations on methane in underground mines

Various research work have established the effects of barometric pressure variations on methane inflow from the gob or strata (Carter and Dust, 1955; Boyer, 1964; and Stevenson, 1968). The continuous and periodic variation of atmospheric pressure causes mine air pressure pumping which affects the volume of methane gas which is subject to the laws of gases (McIntosh, 1957). The pulsation mixes methane with air due to methane inflow induced from the gob into the airway. Methane concentration increase may be established in the mine air and such an increase may results in gas explosion. The relationship between coal mine explosion and time of weather frontal passage analyzed for 259 coal mine explosions is depicted in Figure 2-3 (McIntosh, 1957). Methane concentration increase is high for columns -2, -1, and 0, which represent a period of decreasing pressure when most of the explosions occurred. The explosions claimed 622 lives of miners as indicated in Figure 2-4.

Gas explosion due to variations in barometric pressure dates as far back as 1868 when 49% of 525 firedamp explosions from 1868-1870 in Britain was concluded by Robert Scott and William Galloway to be caused by rapid and significant drops in pressure (Fauconnier, 1994). Similar analysis proved that 59 explosions in South Africa mines from 1970-1989 could be attributed to barometric pressure changes, for which 26 and 33 explosions occurred in coal mines and metal mines, respectively (Fauconnier, 1994). The analysis showed that the explosions occurred randomly in the year and most of the 59 explosions were due to longer than 1 day drop in barometric pressure.

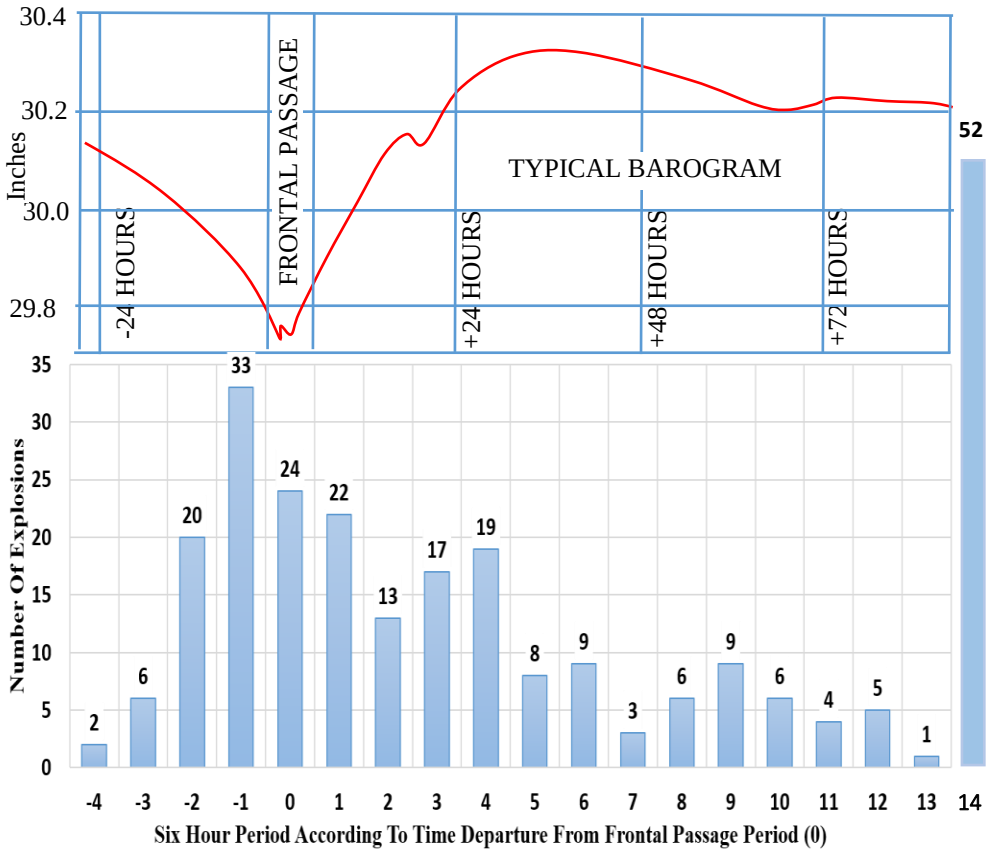


Figure 2-3. Explosion frequency in relation to time of weather frontal passage (McIntosh, 1957)

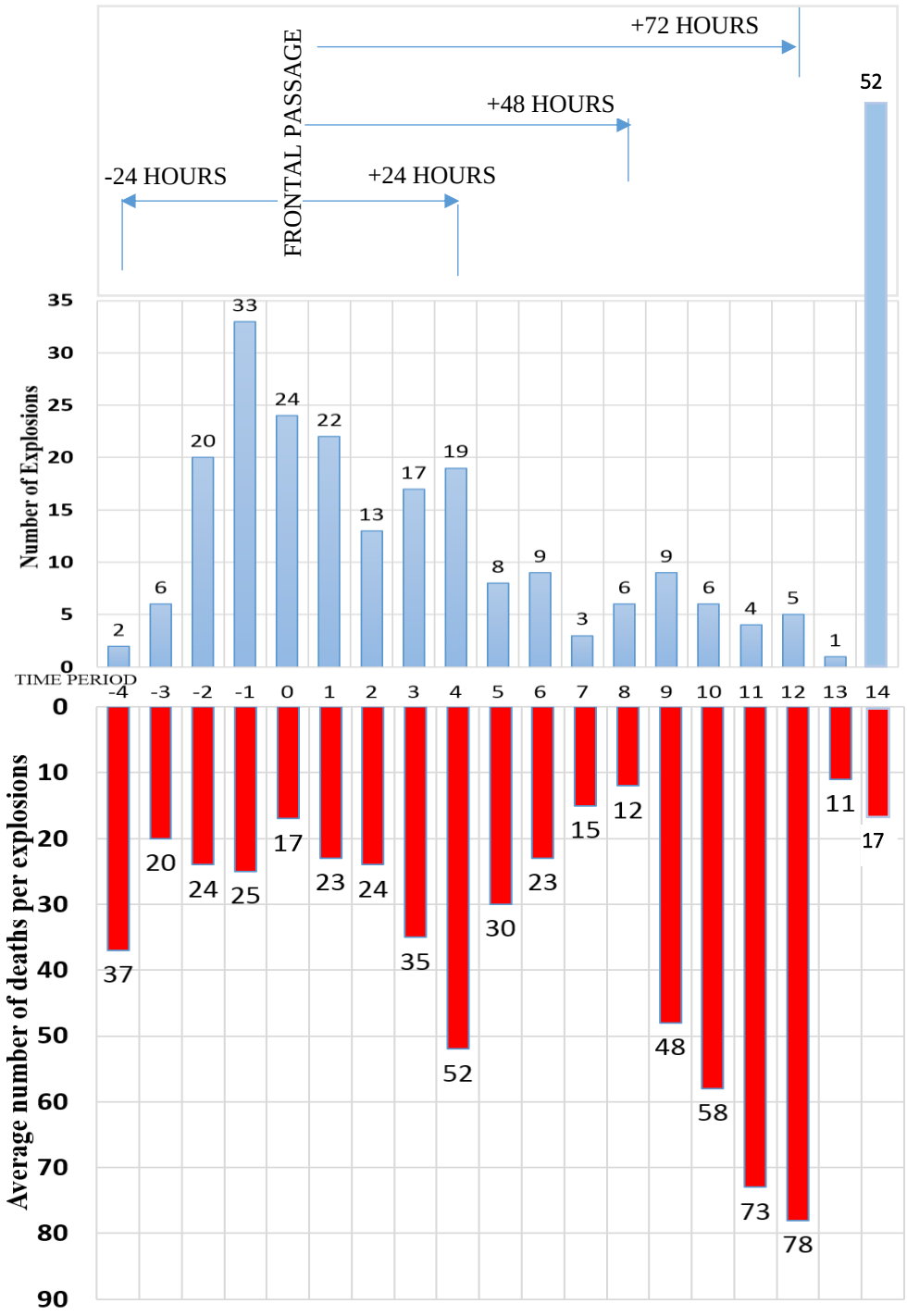


Figure 2-4. Average number of explosion deaths in relation to time of weather frontal passage (McIntosh, 1957)

### 2.2.6 Diesel particulate matter (DPM)

Diesel particulate matter is a constituent of diesel exhaust emissions as a result of using diesel powered equipment in underground mines. The U.S. Environmental Protection Agency (U.S. EPA) defines DPM based on the measurement procedures summarized in the Code of Federal Regulations, (CFR 40:86 N) as any material being emitted from a diesel engine that can be collected on a filter through cooled and diluted exhaust with the temperature held below 52$^{o}$C (126$^{o}$F) (EPA 2002). The composition of diesel aerosols include elemental carbon (EC), organic carbon (OC), sulfur compounds, and ash. EC is the solid carbon soot created as a result of fuel burning at higher temperatures in the absence of oxygen (EPA 2001) in fuel rich regions during fuel combustion. Most EC, after its formation, is subsequently oxidized and the residue exhausted in the form of solid agglomerates (Kittelson, 1998).

Organic carbons are unburned hydrocarbons in fuel and lubricating oil within lean regions. Organic carbon compounds appear as volatile and soluble materials which will change in both composition and phase during emission.

The downside of using diesel engines in underground mines is occupational health and safety due to the exposure of workers to the complex mixture of gaseous and particulate contaminants in the working environment.

Growing evidence is showing up in the literature that exposure to DPM adversely affects human health in both acute and chronic terms. It is suspected and/or rated as human carcinogen by a number of organizations including World Health Organization (WHO, 1996), National Institute of Occupational Health and Safety (NIOSH, 1988), International Agency for Research on Cancer (IARC, 1989 and 2012), and National Toxicology Program

(NTP, 2000 and 2011). Underground mine workers stand the risk of being affected. Other gases such as carbon dioxide, carbon monoxide, oxides of nitrogen as result of diesel powered equipment are also hazardous to the safety and health of mine workers.

### 2.2.7. Mine Dust

Dust is the solid particles in the air. The normal atmospheric dust has a size range of 1-20 $\mu$m (Hartman et al, 1997). It is generated from the various mining activities such as blasting, crushing, machine and air movements. Mine dust can be harmful to the health of mine workers and a threat to their safety. Respirable dust with an upper particle size of 7 $\mu$m (McPhersons, 1993) can cause all sort of ailments when inhaled into the human lungs. Examples of such diseases as a result of over-exposure to mine dust are pneumoconiosis from coal dust and silicosis from silica dust. Also, coal dust when ignited can lead to fires and secondary blast in the mine. Dust suppression techniques and wearable respirators are some of the measures instituted to prevent over-exposure to dust by mine workers.

## 2.3 Standards and regulatory limits for underground mine contaminants

### 2.3.1 Atmospheric monitoring systems

The standards for atmospheric monitoring systems (AMS) in underground coal mines are described in code of federal regulation (CFR) title 30 §75.351. It enlists the mandatory safety standards that are required to be complied with for the operation of AMS in underground coal mines. For instance, AMS sensors should have visual and audio alerts. The AMS specifically for methane is provided in CFR 30 §57.22301.

### 2.3.2 Exposure limit for mine contaminants

The exposure limits for airborne contaminants for underground metal and nonmetal mines are specified in CFR 30 §57.5001 which states that "With the exception of asbestos, exposure to airborne contaminant shall not exceed, on the basis of threshold limit values-time weighted average (TLV-TWA) adopted by American Conference of Governmental Industrial Hygienists (ACGIH), 1973." The TLVs recommended by ACGIH are presented in Table 2-5.

The regulatory limit for preventing mine workers' exposure to DPM is provided in CFR 30 §57.5060 which states that "Effective May 2008, a miner's personal exposure to DPM in an underground mine must not exceed an average eight hour equivalent full shift airborne concentration of 160µg of total carbon (TC) per cubic meter of air (TC µg/$m^3$)."

Table 2-5. Threshold limit values for mine contaminant gases (McPherson, 1993)

| | Threshold limit values (TLV) | |
|---|---|---|
| Contaminant | Time weighted average (TWA) | Short term exposure limit (STEL) |
| carbon dioxide | 0.5% | 3.0 % |
| hydrogen sulphide | 10 ppm | 15 ppm |
| sulphur dioxide | 2 ppm | 5 ppm |
| carbon monoxide | 50 ppm | 400 ppm |
| Nitrogen oxide | 25 ppm | - |
| Nitrous oxide | 50 ppm | - |
| Nitrogen dioxide | 3ppm<br>ceiling: 5ppm | - |
| Methane | 1% isolate electricity,<br>2% remove personnel | - |

- Not available

### 2.3.3 Exposure monitoring for mine contaminants

Exposure monitoring of contaminants in underground metal ad nonmetal mines is described in CFR 30 §57.5002. Also, the exposure monitoring specific to DPM is provided in CFR 30 §57.5071. This is to ensure that exposure of mine workers to these contaminants do not exceed the regulatory limits.

### 2.3.4 Exposure control for mine contaminants

Exposure control to airborne contaminants for underground metal and nonmetals mines are stipulated in CFR 30 §57.5005. Actions for excessive methane is described in CFR 30 §75.323. In this standard, no work is permitted in the working areas if methane concentration reaches 1% and workers must be removed from the affected area if the concentration reaches 1.5%.

Diesel particulate matter reduction strategies and exposure controls are listed in CFR 30 subsection D. The mining industry has adapted various diesel exhaust emission reduction strategies such as modern cleaner engines, improved or increased regular maintenance, alternative fuels like bio-diesel, and exhaust after-treatment technologies (MSHA, 2009) to curtail the amount of diesel exhaust fumes emitted into the mine environment. Also, DPM exposure controls are implemented in underground mines to limit mine workers exposure to the DPM. This includes effective ventilation to dilute the DPM concentration, environmental enclosed cabins to isolate miners from constant exposure to the exhaust emissions, and good work practices such as minimizing engine idling, keeping traffic downstream from miners who work outside of cabs, routing haul trucks in return air

especially when they are loaded and ascending ramps, and limiting horsepower based on available air flow (Mischler and Colinet, 2009).

## 2.4 Monitoring mine atmospheric conditions

In order to ensure safe working conditions in underground mine environment, various air parameters and mine contaminants are monitored. Monitoring also helps with regulatory limit compliance for mine contaminants.

### 2.4.1 Mine air parameters monitoring

#### 2.4.1.1 Air velocity

Several instruments are available for measuring mine air velocity including, smoke tube, vane anemometer, velometer, Pitot tube, rotameter, thermometer and hot wire anemometer, and Kata thermometer (Hartman et al, 1997). Amongst all of these instruments, the vane anemometer is the commonly used. The typical velocity range measured by the vane anemometer is 2,000-10,000 fpm (10.16-50.8 m/s), Hartman et al, 1997).

New technologies have emerged used for continuous velocity monitoring as such ultrasonic anemometer (Caster et al, 1995), thermo mass flow (Heldman, 2003) and vortex shedding (Hennessy, 2005 and Giosen, 2008). The maximum air velocities recommended for underground mines are depicted in Table 2-6.

Table 2-6. Recommended maximum air velocities (McPherson, 1993)

| Area | Velocity (m/s) |
|---|---|
| Working faces | 4 |
| Conveyor drifts | 5 |
| Main haulage routes | 6 |
| Smooth lined main airways | 8 |
| Hoisting shafts | 10 |
| Ventilation shafts | 20 |

#### 2.4.1.2 Psychrometric properties

Effective dilution of mine contaminants through ventilation can be achieved by monitoring the mine conditions such as the psychrometric properties and adjusting ventilation accordingly. Psychometry properties include wet-bulb temperature, dry-bulb temperature, and humidity, barometric pressure, and density. Various sensors have been developed to measure psychometry properties in underground mines. Such sensors include mercury barometer, aneroid barometer or the special feature barometer (Hartman et al, 1997). Differential pressure measurements are performed between two points in the mine using manometers. Dry-bulb and wet-bulb temperatures are measured using sling psychrometer, dew point hygrometer, and static hydrometer (McPhersons, 1993).

### 2.4.2 Mine contaminants monitoring

The most common detection principles for mine contaminants as delineated by (McPherson, 1993) are as follows;

a. Filament and catalytic oxidation (pellistor) detectors.

   These devices are used primarily for the measurement of methane and other gases that will burn in air such as carbon monoxide, hydrogen or the higher gaseous hydrocarbons

b. Flame safety lamps

   These lamps were introduced early in the nineteenth century for the purposes of providing illumination from an oil flame without igniting a methane-air mixture

c. Thermal conductivity and acoustic gas detectors

At 20°C and at normal atmospheric pressures, the thermal conductivity of methane is 0.0328W/m °C compared with 0.0257 W/m °C for air.

d. Optical methods

Three types, interferometers which utilize the refraction of light that occurs when a parallel beam is split, one half passing through the sample and the other through a sealed chamber containing pure air. The nondispersive infra-red gas analyzer is one form of absorption spectrometer that is frequently used for mine gas analysis. Identical beams of slowly pulsating infra-red radiation pass through two parallel chambers, one containing a gas that does not absorb infra-red (typically nitrogen) and the other fed by a stream of the sample. Laser spectroscopy is another means of air analysis that has considerable potential for subsurface application.

e. Electrochemical methods

Very small concentrations of many gases can be detected by their influence on the output from an electrochemical cell.

f. Other devices are the mass spectrometers, paramagnetic analyzers, gas chromatography, semiconductor detectors, and stain tubes.

Two sampling method, manual and automatic, are employed for measuring contaminant concentrations in underground mine.

The manual method consist of grabe samples which involves the collection of air or gas volume for laboratory analysis to determine its contaminants concentration. Also personal samples which continuously monitor contaminant concentrations is used. It may be equipped with alarm capability.

The automatic and remote method includes permanent environment monitors that are placed in critical locations in the mine to monitor most gas contaminants, machine mounted gas monitors that are placed on coal cutting machines to measure methane concentration from the strata during operation and the tube bundle system.

### 2.5 Signal processing techniques

It is necessary to use time series analysis and other methods to smoothen and also characterize variations in the primary data in order to distinguish critical changes from the normal signal trends. Time series analysis comprises methods for analyzing time series data in order to extract meaningful statistics and other characteristics of the data. Time series forecasting is the use of a model to predict future values based on previously observed values. Two techniques are used for time series analysis, namely, parametric and non-parametric. The parametric approaches assume that the underlying stationary stochastic process has a certain structure which can be described using a small number of parameters (for example in autoregressive or moving average models). In these approaches, the task is to estimate the parameters of the model that describes the stochastic process. Non-parametric approaches explicitly estimate the covariance or the spectrum of the process without assuming that the process has any particular structure (Jianqing and Qiwei, 2003).

Different time series statistical models represent different stochastic processes which are applicable in filtering the primary data such as auto regression, integral, and moving average models (Shumway and Stoffer, 2010). These models are used to filter the noise and analyze the trends.

### 2.5.1 Useful algorithms for data filtering including Matlab implementation for signal processing.

The mine air parameters and concentrations have fluctuating signals with time due to disturbances from ambient conditions as well as from mining operations. The existence of measurement errors must be filtered in order to dampen the noise, describe the signal trends and also characterize variations in the primary measured data to distinguish critical changes from the normal signal trends. There are a number of signal processing filtering algorithms that can be used to smoothen signals with noise. Some useful ones are delineated as follows (Gray ad Davisson, 2000);

a. Low pass filters

   These are filters used to eliminate all frequencies above a specific cutoff frequency allowing only frequencies below the cutoff frequency to pass. The amount of reduction in the signal depends on the range of signal which is of interest.

b. High pass filters

   This is the opposite of low pass filter which allows all frequencies above a cutoff frequency to pass and remove those below.

c. Autoregressive filters

   A stochastic process used in statistical calculations in which future values are estimated based on a weighted sum of past values. An autoregressive process operates under the premise that past values have an effect on current values, therefore, the output values are calculated based on regressions of the previous output values. The process model is in the form:

   $$y(n) = \sum_{m=0}^{M} b_m x(n-m) + x(n) \qquad (2\text{-}1)$$

where; *y(n)* is the output of the model, *x(n)* is the input of the model, and *x(n - m)* are previous samples of the model output value and $b_m$ is equation coefficient.

d. Moving average filter

Moving average is replacing each data point in the signal with the average of adjacent points within the span known as the smooth width. It is represented by the equation below,

$$y_S(i) = \frac{1}{2+N}[y(i+N) + y(i+N-1) + \ldots + y(i-N)] \qquad (2\text{-}2)$$

where $y_s(i)$ is the smoothed value for the ith data point, $N$ is the number of adjacent data points on either side of $y_s(i)$, and $2N+1$ is the span.

Figures 2-5 and 2-6 demonstrate the "moving average window" evaluation chart for usage of time series analysis in filtering and evaluating the primary data for identifying the root cause of the change which is used to forward predict future outcomes.

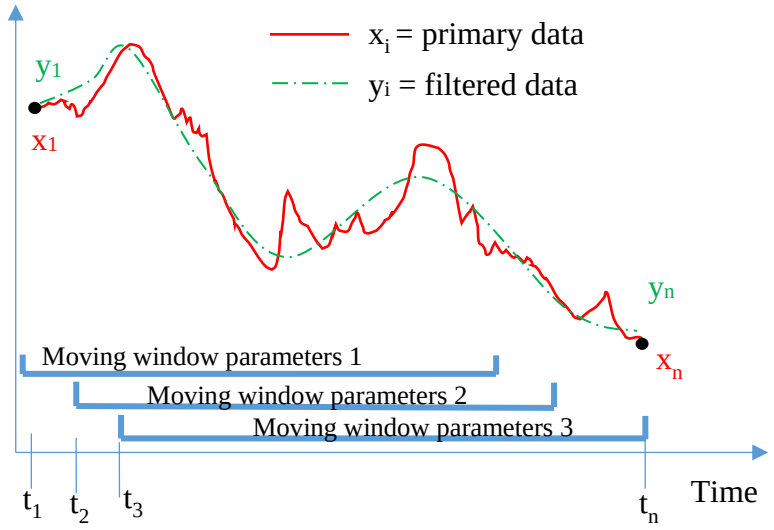


Figure 2-5. "Moving window" evaluation of the signal flow (Danko et al, 2016).

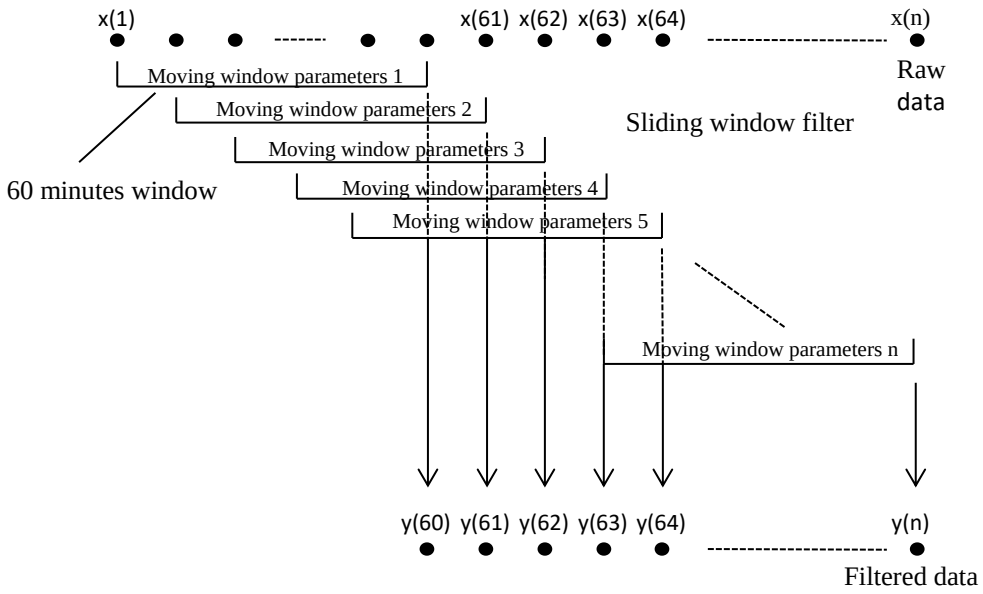


Figure 2-6. “Moving window” filter processing schematic (Danko et al, 2016).

e. Savitzky-Golay filter (Press et al, 1988)

The Savitzky-Golay algorithm was originally developed for spectroscopy, but works well for other high frequency signals since it does not distort the high frequency component of the signal. This algorithm averages the points in a data set by deriving the filter coefficients by performing an unweighted linear least-squares fit using a polynomial of a given degree (Press et al, 1988). Compared to the sliding-average smooths, the Savitzky-Golay smooth is less effective at reducing noise, but more effective at retaining the shape of the original signal. The Savitzky-Golay algorithm is more complex. Example of a filtered signal using this filter is shown Figure 2-7.

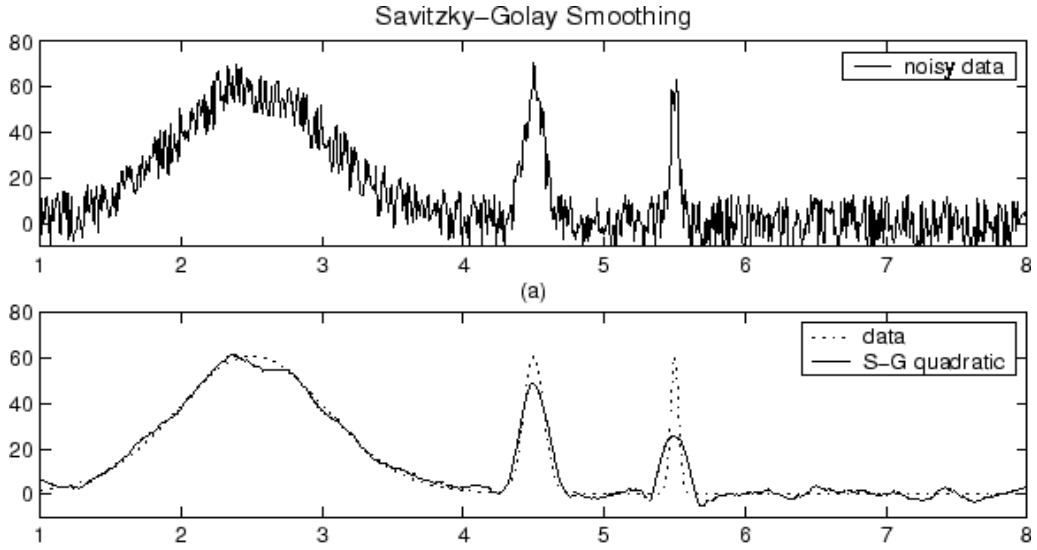


Figure 2-7. Plot (a) noisy data (b) filtered data (Press et al, 1988)

f. Correlation of signals

This is a measure of the degree of similarities between two signals. Given two real-valued signals x(n) and y(n) for n samples. The cross correlation, is given as;

$$r_{xy}(l) = \sum_{n=-\infty}^{\infty} x(n)y(n-l) \quad (2\text{-}3)$$

where; $l$ is the shift parameter.

The autocorrelation is the cross correlation of a signal with itself given as;

$$r_{xy}(l) = \sum_{n=-\infty}^{\infty} x(n)x(n-l) \quad (2\text{-}4)$$

All the above filtering techniques can be processed in Matlab with various solutions. Therefore, Matlab can be utilized for filtering the primary mine measurement data using the different filtering techniques discussed above to eliminate the noise from the signal and the most useful filter would be implemented in my research work.

### 2.5.2. Fault detection as applied to recognizing a hazard scenario

Faults in the measurement signals can be detected by searching for disturbances in the signatures for the various air parameters, fan powers, and the production and their signal properties identified from the filtered data. Most important mathematical properties to be considered for the signals are the sliding average values for various window size; the Root Mean Square (RMS) values; and the upper and lower limits. The periodic trends such as the hourly, daily, weekly monthly and yearly sliding averages for the history of signals need to be identified.

# 3.0 Chapter 3- Research Concept and Methodology

This chapter is taken from the final report for an Alpha foundation funded project (Danko et al, 2016) for which I worked as a research assistant for two and half years and was instrumental in the report write up.

## 3.1 Research concept

Safety problems such as gas concentrations in underground mines change and these changes are related to different disturbances. These changing gas concentrations values might soon reach a threshold limit value. Therefore, a concentration value at a monitored location might not be critical but these changes can cause it to be critical at a later time. This will lead to a threshold value crossing at a different location other than the monitored location.

The threshold crossing will be due to the continuous downstream addition of concentration to the increasing level as a result of cascading. As such, changes which trigger continuous increase of gas level at a time delay including sudden gas in burst, roof collapse, fan malfunctioning, barometric pressure changes and fire load can be modeled to check how it affects the dynamic signature of gas concentration in the mine airway.

An Early Warning System (EWS) is developed to forecast and forward predict gas concentration increase caused by various disturbances and provides useful management decision protocol for flagging imminent or near-future safety hazards.

The new and innovative components are (Danko et al, 2016):

(1) The EWS uses real-time monitoring signals for forecasting in accelerated, simulation-time from the data to predict any likely event in the near future that may compromise safety; and

(2) The EWS uses the mine layout to forecasts in space, in order to evaluate safety at any critical working area, even at a place where no monitoring station is installed.

Figure 3-1 illustrates the concept of the EWP for a methane concentration example at an assumed critical location, critical workplace that is different from the AMS location.

The air parameters and their changes are simulated by the EWP model in forward predicting mode calculating gas concentrations at critical (forecasted) locations and critical (forecasted) time in the near future. The simulation time is much shorter (shown in dashed lines), by orders of magnitude less than the mine's assumed signal at critical location in real-time, giving an advantage in time for warning message for accident prevention. The air parameters and the changes are "sensed" by the EWP model all over the mine including places where there are no sensors.

Figure 3-2 depicts the schematic layout of monitored and critical locations for the explanation of the 'forecast in space' concept. The criteria used to determine a critical location is based on the areas that may have high concentration of gases that could lead to threshold crossing. Note that all nodes are modeled, but only a few are monitored; the critical location (C,m) may not have a monitor and a hazardous concentration may be 'sensed' without a model. This is a new and innovative element in using the EWP system, improving a serious limitation in current monitoring systems that hamper their direct usefulness in disaster avoidance. One must ask: how can a sparsely monitored system sense e.g., sudden gas in-bursts and concentration spikes at the critical location close to the source

if no sensors are installed near that location? The innovative EWP provides the answer and solution to this question by evaluating the critical concentrations, temperatures, velocities, pressures, etc. at all locations and matching the spatial distribution of the solution with those from measurements at the available, monitored locations.

The innovative EWP system runs five real-time processes simultaneously, performing

(1) Interpretation of the AMS signals in comparison with the APPS model;

(2) Validation of both the model and the sensor readings in their relationship to each other;

(3) Identification of plausible source changes as reasons for differences other than model error or sensor malfunction as unexpected changes at the BC (boundary conditions);

(4) Evaluation of the hazard conditions at critical locations; and

(5) Extrapolation of the trend with time and flagging crossing points with maximum threshold values for issuing an early warning.

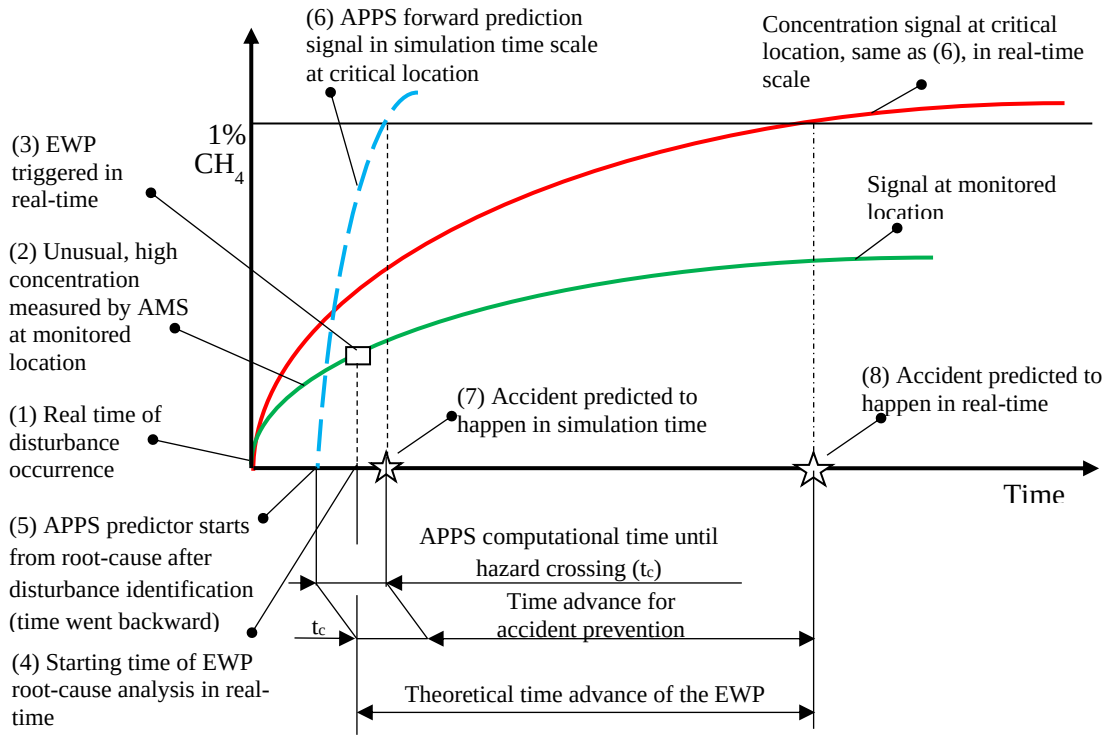


Figure 3-1. Schematic of the EWP "forecast in space and time" concept for methane concentration early warning at the workplace (critical location), based on a trigger from the AMS signal at monitored location (in real-time) and APPS model prediction (in simulation-time scale). Sequence of events are numbered from (1) to (8), (Danko et al, 2016).

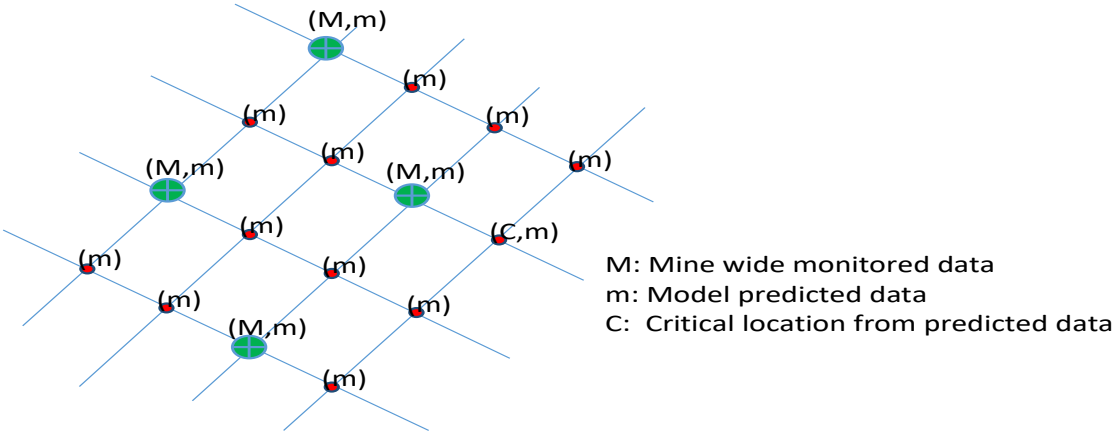


Figure 3-2. Monitored (M), modeled (m), and critical (C) locations at a mine. Note that a critical location may not be monitored at the mine but will always be predicted with the EWP system (Danko et al, 2016).

### 3.1.1 Elements of the Early Warning System (EWS)

The EWS is developed for use by operating mines which already have (a) monitoring system of atmospheric conditions real-time; (b) a mine information system that transfers real-time data from the monitoring system to the EWS and from the ventilation operation parameters as well as ground control sensors; and (c) a mine ventilation model running in either VnetPC (VnetPC, 2007), Ventsim (Ventsim, 2016), or MULTIFLUX (Danko, 2008, Danko and Bahrami, 2008). All modern mines have advanced, monitoring and mine information systems and adopted at least one or sometimes more ventilation models of their choice.

The EWS is developed to be embedded into the infrastructure of a modern mine with a mine ventilation and control system.

The main components necessary for an EWS to function are a number of atmospheric sensors such as air parameter sensors for velocity, airflow rate, relative humidity, pressure and temperature, and gas concentration sensors in the order of at least a few dozen for a mine with a few hundred airways. Atmospheric sensors in strategic locations must be monitored real-time. Mine production data (MPD) and operating parameters in the mine should as well be recorded continuously.

The EWS requires real-time data to be passed from the mine monitoring system for evaluation and forward prediction. The innovative approach of the EWS is that it links together the mine ventilation model, the data stream from the real-time sensors, and an expert system with a forecasting evaluation program that provides a warning message, flagging imminent or near-future safety hazards.

## 3.2 Methodology for model development

### 3.2.1 Link the native VAM of a mine to the APPS

Different mines use different native ventilation air models (VAMs) such as Ventsim and VnetPC. The first step in the model development is to the link these calibrated native VAMs to the APPS used in MULTIFLUX. An input data transfer macro program is developed to read the input data files of the native ventilation model (such as VnetPC, Ventsim) and to translate the model configuration of the surrogate APPS model in the EWP. Best conversion is provided in Ventsim as it is the most convenient with a user friendly graphical user interface (GUI). Conversion from Ventsim to the surrogate APPS source-code model is automatic. Ventsim can import a VnetPC or MULTIFLUX VAM automatically therefore, it can connect to the APPS source-code model directly.

The APPS is used first as a past time simulator in corrector mode for identification of the changing boundary condition (BC) of the ventilation model against real-time mine measurement data. The APPS model is run by a macro and uses data files for input, a very different application style from using the native VAM of the mines directly.

The native VAM of a mine is assumed to be calibrated, providing correct data for relevant air parameters for the mine. Model configuration for partner mine examples were converted and modeled in MULTIFLUX. Figure 3-3 shows the activity chart for converting the native VAM and running the converted model in MULTIFLUX. Appendix 1 illustrates the detailed comparisons qualifying the APPS as a validated, surrogate model to replace the native VAM in operating the EWP.

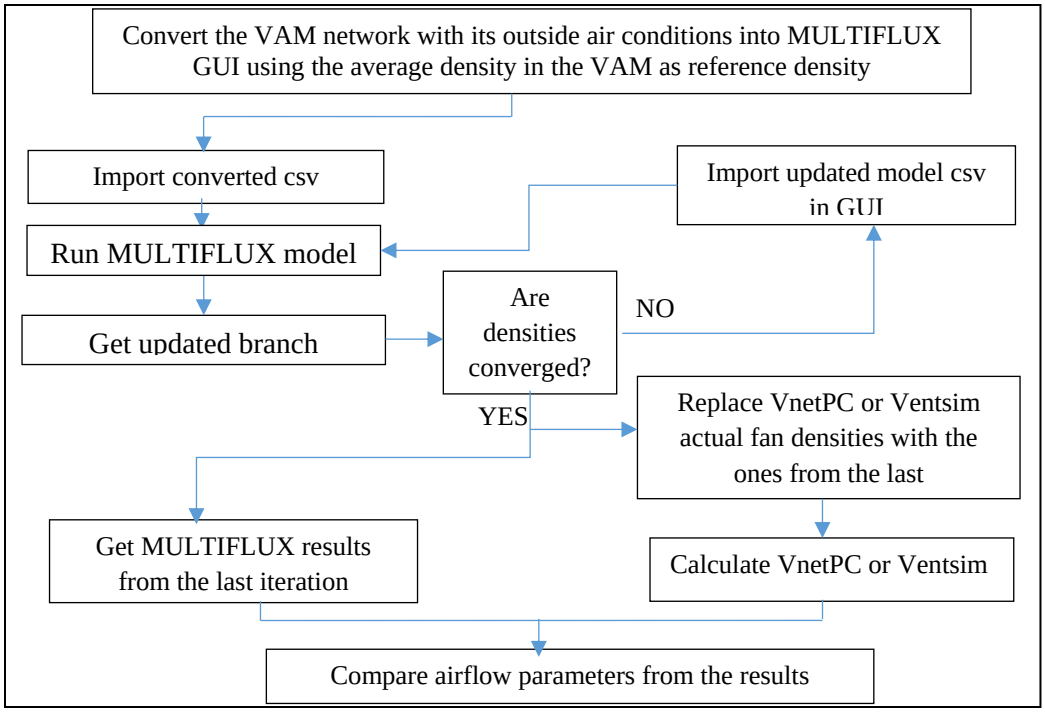


Figure 3-3. Activity chart for running MULTIFLUX (Danko et al, 2016).

#### 3.2.1.1 Model comparison and validation of the APPS model

The software macro is tested for five examples from the partner mines for acceptable match between the APPS model and the native VAM model in air parameter predictions. The comparisons qualifying the APPS as a validated, surrogate model to replace the native VAM in operating the EWP is detailed in Appendix 1. The simulated results from MULTIFLUX are near perfect match with the native VAMs model results for airflow parameters comparison. This provided the basis for commencing with the next approach in the study.

### 3.2.2 Recognition of safety hazard

As indicated in the forgoing, current monitoring sensors have a serious limitation to safety hazard recognition. The necessary activities for recognizing safety hazard developed in this

research work are: (1) data collection; (2) sensor data processing; (3) root-cause analysis; (4) forward prediction; and (5) flagging for criticality.

#### 3.2.2.1 Data collection

Synthetic AMS output data at the real sensor layout locations at a mine is generated by the APPS model with a synthetic change in the BC with an added error to emulate measurement error or sensor malfunction. The model is then calibrated with synthetic data from the ventilation model due to lack of real mine data. The expected data from the sensors is a sequence of data points consisting of successive measurements collected at regular time intervals.

#### 3.2.2.2 Sensor data processing and evaluation

Different signals from monitoring sensors are collected by the mine central data acquisition system and different mine air parameters, concentrations, and disturbances may have different signals. The flow chart for signal analysis problem identification is depicted in Figure 3-4. The mine air parameters all have fluctuating signals with time due to disturbances from ambient conditions as well as from mining operations.

The signal is first analyzed for hazardous trends by a trend analyzer with dynamic identifiers determined before a root cause is commenced. This is then followed by a forward prediction once a specific problem is identified.

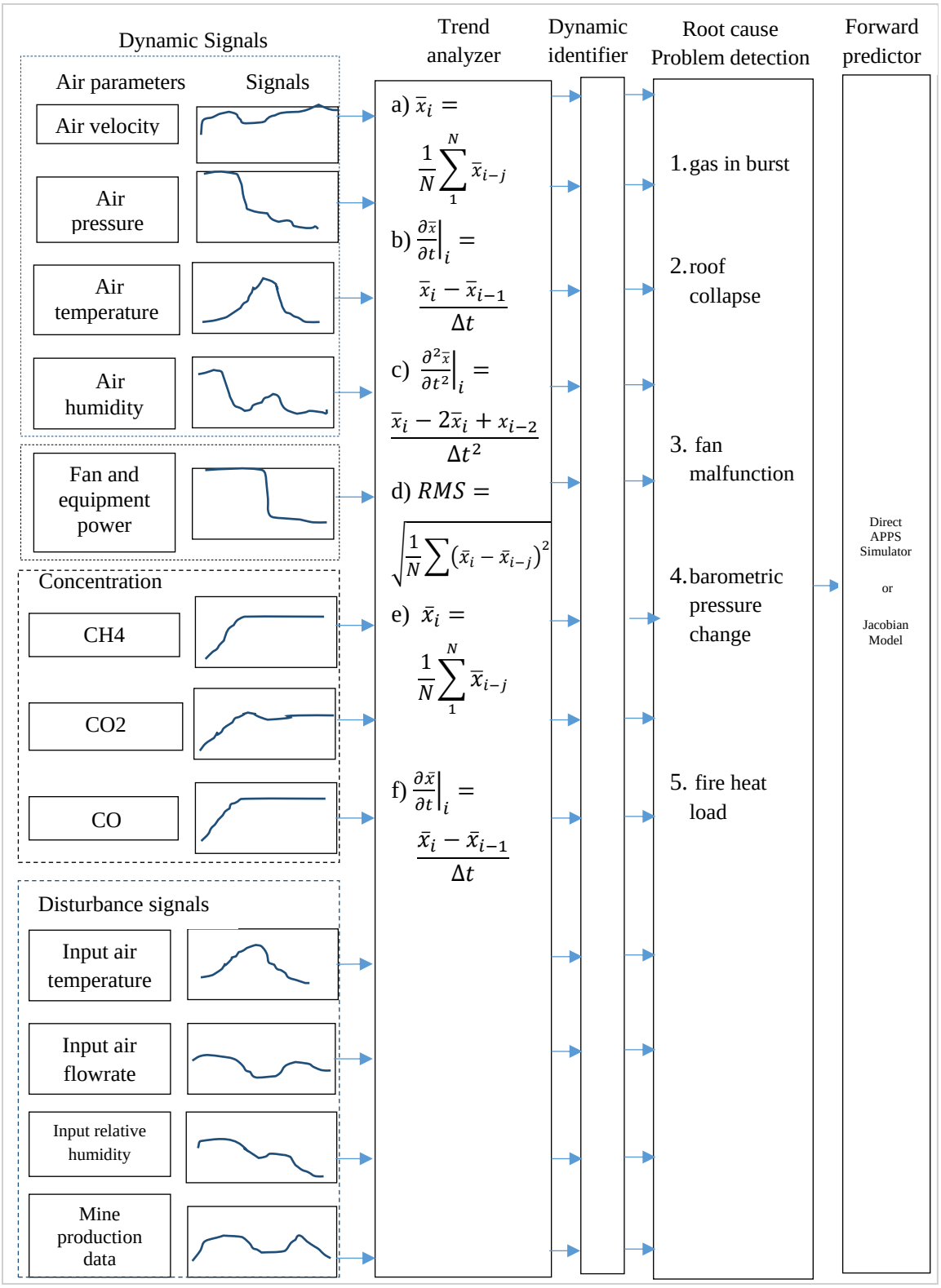


Figure 3-4. Flow chart for signal analysis problem identification (Danko et al, 2016).

#### 3.2.2.2.1 Signal-based trend analysis

Each signal for the various air parameters, fan powers, concentrations and the production disturbances is analyzed and processed into properties by a trend analyzer. Examples of a trend analyzer are as follows:

a) Sliding average value of sensor signal
b) First derivative of sliding average
c) Second derivative of sliding average
d) Root Mean Square (RMS) spread over sliding average (significance check)
e) Sliding average value of disturbance
f) First derivative sliding average value of disturbance

First, signal signatures are searched for and identified by mathematical properties, i.e., signal and system properties.

**a. Signal properties**

Most important are the average value, the RMS value, and the upper and lower limits as shown in Figure 3-5a. In addition, the first and the second derivatives are also very informative as depicted in Figure 3-5b and 3-5c, respectively.

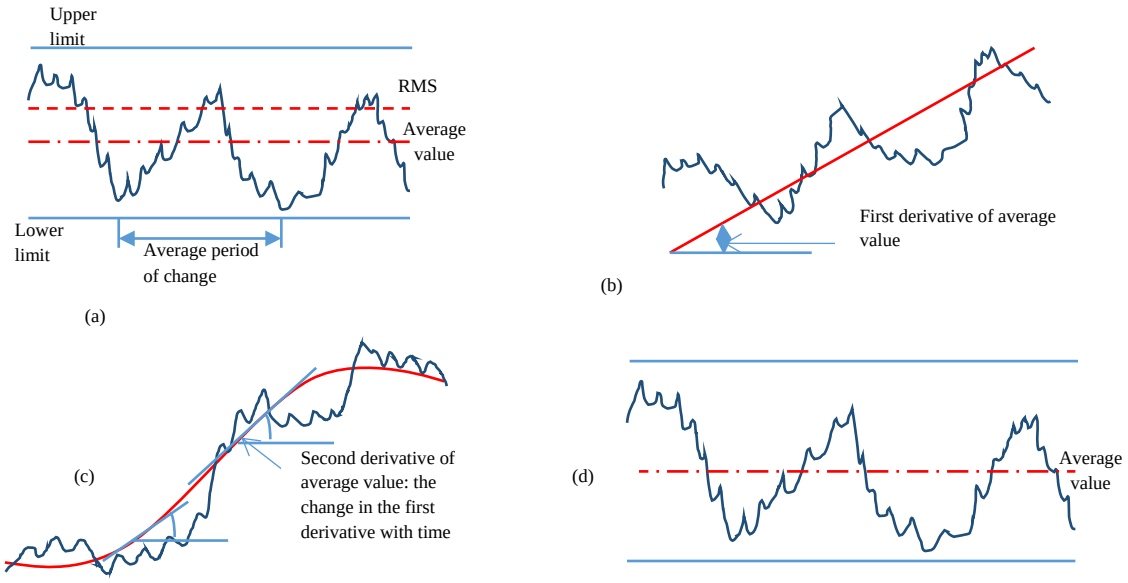


Figure 3-5. (a) Primary signal (b) first derivative (c) second derivative and (d) trend of system constants (Danko et al, 2016).

**b. System properties**

Each measurement signal of an air parameter is an outcome of a mass transport system. There are system characteristics imprinted in the signal trend. The system characteristics should not change if the system is not disturbed. System characteristics and their trends are identified. An n-order system can be characterized by an n-order differential model.

$$A_n \frac{d^n X}{dt^n} + A_{n-1} \frac{d^{n-1} X}{dt^{n-1}} + \cdots + A_o X = B \qquad (3\text{-}1)$$

where; $A_n$, $A_{n-1}$, and $A_o$ are system properties; X is sensor data; $t$ is time, and B is the constant.

After normalization, an n-order system is described by n constants. The EWS identifies the system constants as system properties behind the signal itself. Next, the trends of each system constant is analyzed the same way the signals are analyzed. For example, $A_n$ may

look like Figure 3-5d. Examples of system properties identification are presented in Appendix 2.

Second, the EWP self-calibrates and defines the allowable a) signal changes and b) system constant change characteristics to the operation of the mine. These parameters are mine specific and even location-specific to a mine.

Third, the EWS flags any threshold crossing of the signals at any location. Any crossing triggers a warning signal. Any warning from ground control and power system monitoring also triggers a warning signal as a kind of threshold crossing.

Fourth, the EWS looks for changes in the system constants. These parameters are assumed to be in-site calibrated with limits and trends, all site and mine specific. If the changes are outside the average trends, a warning signal is issued.

#### 3.2.2.3 Root-cause analysis

The next step after analyzing the signals for hazardous trend is to commence a root cause analysis. A root-cause analysis is conducted on the signals if the changes are significant. Five cases are identified for specific attention.

a. Gas in-burst is detected from sudden, unusual gas concentration increase from the measurement of one or more sensors. This event is analyzed with the forward predictor APPS model using a changed boundary condition at the sensed location. The expected time for direct simulation is 15 seconds showing all concentrations at critical locations. If the mine has gas source that adds sources of gas to the upcoming air with elevated concentration, the accumulated effect may cause threshold crossing in the future time, delayed by travel time.

b. Air flow change is identified and accompanied by pressure change which indicates air flow blockage in an upstream drift section as illustrated in Figure 3-6.

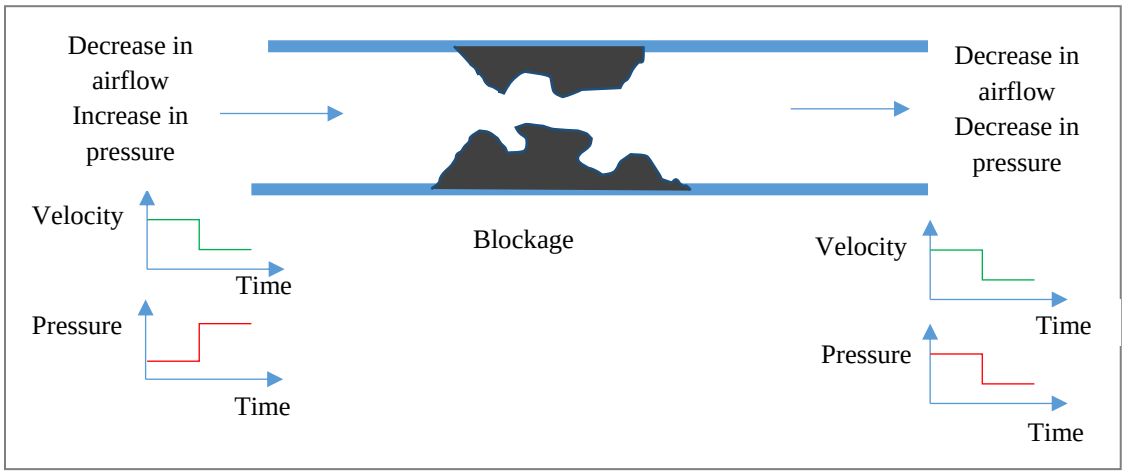


Figure 3-6. Schematic of an airflow blockage and its effect on pressure and airflow (Danko et al, 2016).

The signal evaluation algorithm first looks for ground control and roof stability sensory signals from the roof stability monitoring (RSM). Second, mine-wide changes are analyzed in pressure and velocities before and after this detected event. If the changes are consistent with the signature in Figure 3-6, the likelihood of air flow blockage is identified. The APPS forward predictor algorithm is launched calculating concentrations at critical locations due to this change in the entire mine's flow and gas concentration distributions. The root-cause signals of the sensed concentrations at given locations are used as deviated boundary conditions in the APPS predictor. The expected time for direct simulation is 15 seconds. If the simulation results indicate threshold crossing in any critical location, a warning message is sent.

c. Barometric pressure variation is continuously detected that has an effect on the gas inflow to the mine from the porous gas bearing strata, sealed-off but leaky mine zones or the gob. The critical signals from the sensors are characterized by the amplitude and frequency of the pressure change. It is a particularly difficult signal to characterize for criticality. The ordinary range of change is +/_ 1000Pa, which is in the order of the magnitude of mine fans. An example demonstrating critical methane inflow due to sudden pressure change is in this range. A sudden decrease after an elongated time period with high barometric pressure is considered to be the most critical. However, it impossible to foresee the time period of continuous pressure deviation from a given value at any time instant. A truly continuous simulation is designed to predict this effect as a potentially critical source term from a continuously variable cause of gas inflow.

d. Fan malfunction is detected from the electrical signal of the power system. The mine production data (MPD) signal is checked, and the EWP signal is immediately generated for the management to check if the fan stoppage is not intentional. If it is an unscheduled event, the effect is analyzed by a direct run with the APPS model. The computational time is 15seconds.

e. Fire load is detected by the increased level of multiple gas components as well as of increased temperature. The signature of sensor signals is either step change-type in the average value or in the first derivative. The root cause of these signals is unmistakable, flagging criticality and sending a EWP warning for fire hazard. No forward prediction simulation is necessary in this case.

#### 3.2.2.4 Forward prediction

The signal evaluation process first looks for gas concentration increase from the sensors. Second, mine-wide changes are analyzed in air parameters (ie. airflow, velocity, pressure and relative humidity). If the changes are consistent with the signature of any of the five cases, it is identified as the root cause of the change.

Once the root cause has been identified, this event is modeled and analyzed with the forward predictor APPS model using a changed boundary condition at the sensed location. The root-cause signals of the sensed concentrations at given locations are used as deviated boundary conditions in the APPS model. The concentrations at critical locations due to this change in the entire mine's flow and gas concentration distributions are calculated and forward predicted the next time period.

Two methods are available for forward prediction: (1) fast direct simulation and (2) an innovative, differential forward prediction algorithm based on the use of the Jacobian matrices between differential BC parameters and differential responses for air flows, concentrations of critical mine gas components and heat. Direct simulation deals with the solution of the entire mine model whereas the Jacobian model run is a matrix-vector calculation. The forward prediction time with the Jacobian model is minimal, requiring only matrix-vector multiplications. However, the direct simulation method is used in this study due to the high computational efficiency of the MULTIFLUX solver engine (for example, the CPU solution time of a 27,000-branch mine flow network model is 1.6 second in a laptop computer with a single Intel i7 core).

The system is tested using emulated, synthetic AMS data. Debugging and testing the EWP system with synthetic data are necessary due to the lack of actual mine monitoring data as well as advantageous for performing the test cases under controlled conditions.

The synthetic data are emulated using the native mine ventilation model, which is matched with the APPS model in the EWP. Therefore, no systematic error is suspected in this study simplifying the need for the performance validation in study.

#### 3.2.2.5 Error consideration in model development

In developing the model, measurement uncertainty of a given location as a result of mining operations and ventilation changes from equipment traffic as well as the measurement errors of the measuring devices are taken into consideration for signal processing.

**a. Testing and evaluation of the EWP system with random and perturbed data**

There are different typical error limits for various air parameters that must be taken into consideration for signal processing. Some typical error limits are ±3% for velocity, ±0.3°C for temperature, ±3% for relative humidity, and ±2% for barometric pressure. Agreement and measurement uncertainty in an operating mine is evaluated by comparing measured data from an operating mine and the predicted results from MULTIFLUX and Ventsim. The measured data are imported from a previous NIOSH-funded research project (Danko et al, 2014). Figures 3-7 and 3-8 illustrate the comparison between in-situ measurement results for air velocity and barometric pressure distributions with MULTIFLUX model results for a partner metal mine in Nevada. The confidence bound for velocity and pressure measurement is ± 2.2 m/s and ± 650 Pa are used based on measurement uncertainty of a given location in a metal mine as a result of mining operations and ventilation changes

from traffic. The velocity unit has an accuracy of ± 3% and that of the pressure unit is ± 2.0%. It can be seen that the model results are not matching the measurement results due to some factors such as unknown source terms, ventilation changes from mining operations which are not entered in the model. However, all these factors are incorporated in the early warning system in order not to sound unwarranted alarms. For un-wanted spikes, moving average low pass filter is used to smoothen out the fluctuations. On-site model adjustment relative to measurement data at sensor locations are recommended as part of the EWS initialization. In addition, tolerable bounds with upper and lower limits from various mining activities are to be defined in the EWP.

Sensor failure can be treated and isolated from the correlation of its measurement signal to the signals from neighboring sensors. If the difference between a particular sensor's signal and the neighboring sensors signals is significant, then the sensor would be isolated as defective. Afterward, there would be a followed up to check the sensor to confirm the failure.

Real weather data for Elko, Nevada is used in Ventsim to demonstrate the effects of atmospheric temperature variations in the mine. The objective is to correlate the outside and the inside conditions for the early warning system. The weather data used as an input are depicted in Figure 3-9. A monitoring sensor location close to the active face is set in branch 253 (40 ft perimeter and 3938.1 ft length) of the selected mine for this study is shown in Figure 3-10. The model results for this branch are depicted in Figure A3-11 with a measurement error of ±3$^{o}$C from a typical measurement unit. Since the temperature variations affect the mine ventilation air in a similar manner as the outside condition

changes but with a smaller amplitude and some level of delay, variations in the outside conditions are taken into account in the EWP system to ensure accurate predictions.

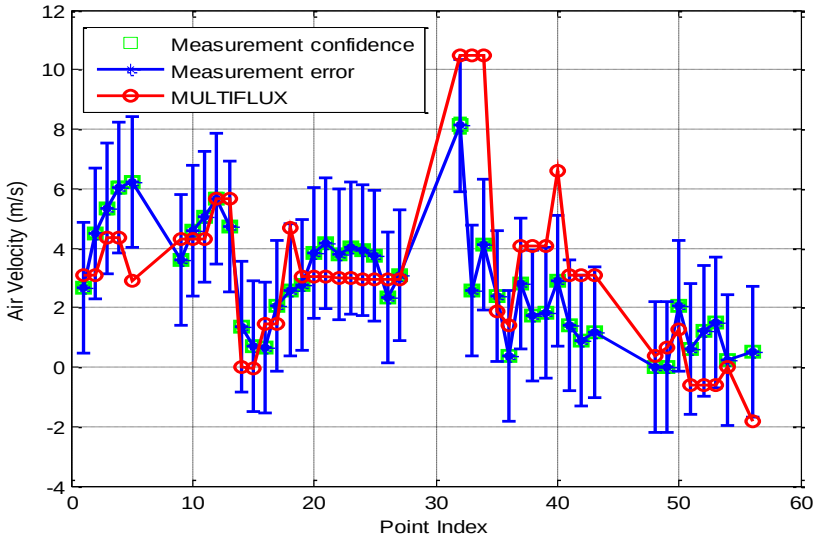


Figure 3-7. Comparison between measured velocities and the results from the MULTIFLUX model with confidence bound (Danko, 2014a)

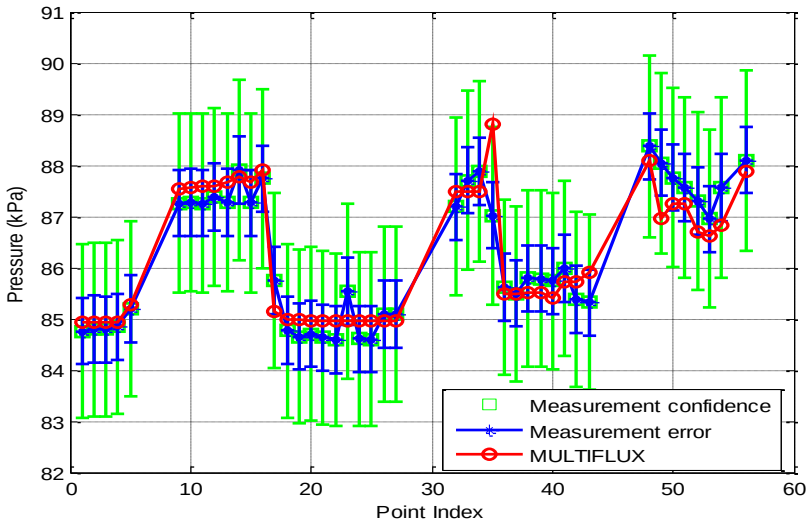


Figure 3-8. Comparison between measured barometric pressure and the results from the MULTIFLUX model with confidence bound (Danko, 2014a).

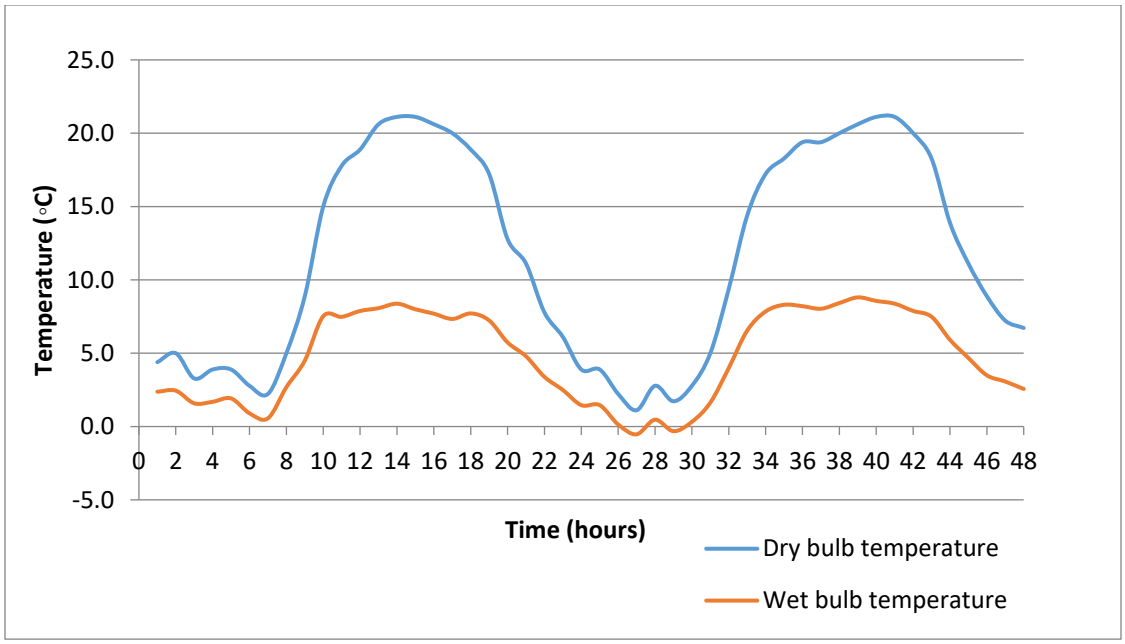


Figure 3-9. Weather data, Elko, NV. April 9-10, 2014 http://www.wunderground.com/history (Danko et al, 2016).

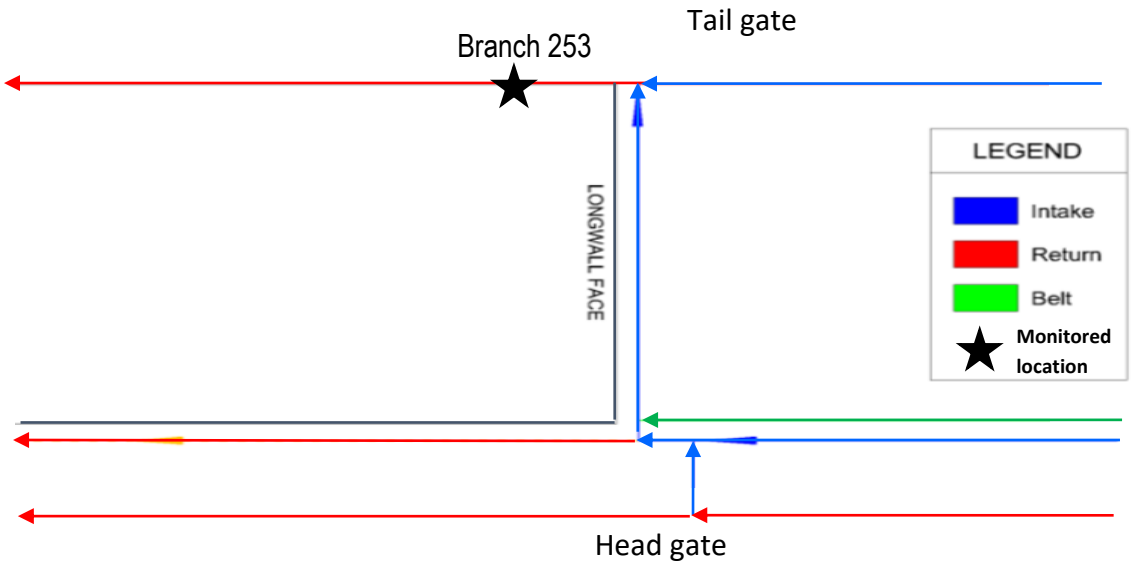


Figure 3-10. Branch 253 monitored location for mine temperature (Danko et al, 2016).

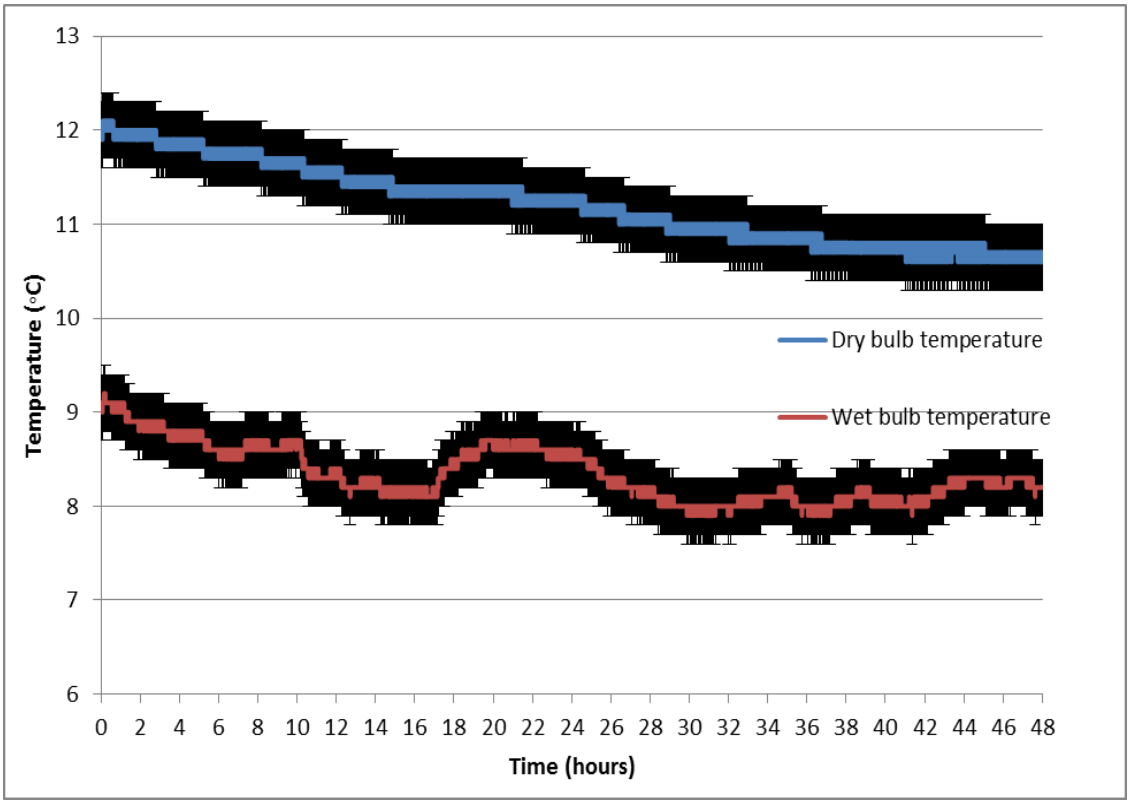


Figure 3-11. Model results for wet bulb and dry bulb temperatures for branch 253 with error (Danko et al, 2016).

### 3.2.2.6 Flagging for criticality conditions at critical location

Data from the sensors are collected at regular time intervals in real application. In this study, emulated, synthetic data are used in lieu of real sensor data from VAM simulations of planned accident scenario. The EWP system is tested with synthetic data due to the lack of actual mine monitoring data as well as advantageous for performing the test cases under controlled conditions. The synthetic data are emulated using the native mine ventilation model, which is matched with the APPS model in the EWP. Therefore, no systematic error is suspected in this study simplifying the need for the performance validation.

The test comprises of using the “blind” emulated sensor data; analyzing the trends of the signals for the root-cause of the changes; and forward predict from that point the possible outcome of the perceived scenario. If threshold crossing for criticality is found from the APPS predictor model (which is a fast running, separate simulator from VAM), the test is considered successful for hazard prediction. The critical elements for success are (a) the accuracy of recognizing the root cause of an unexpected signal change, crossing the tolerance limit of normal regime; and (b) the timely forward prediction, much faster than real-time of future outcome of the disturbance riding toward an accident in real-time.

# 4.0 Chapter 4- Hazardous Contaminant Source Accumulation Simulation, Results and Discussions

Hazardous conditions which affect the safety and health of underground mine workers are simulated and the results are analyzed. The EWP system is tested in its ability to forecast hazardous scenarios during their evolution but before the thresholds for accidents have been crossed. Threshold crossing is caused by methane travel delay time with gas accumulation hazard or methane concentration response delay as a result of atmospheric barometric pressure drop. Methane concentration is simulated and forward predicted based on various hazardous scenarios in order to determine the delay time available for the issuance of an early warning. As part of the dynamic signal interpretation and analysis, an example for DPM contaminant concentration variation travel in the ventilating air from a moving machine is provided. The time averaged DPM concentration travel is determined.

## 4.1 MULTIFLUX (MF) code

The model for my research is configured in MULTIFLUX which is basically a network solution solver. MULTIFLUX has been adapted to mine ventilation, heat, moisture, and gas flow modeling in underground mine airways and has been employed in solving several mine ventilation problems with published results.

The rockmass and the air space are two distinctive model domains dealt with in heat, moisture or vapor, and air transport calculations. A different modeling solution is required for each domain. An integrated-parameter Computational Fluid Dynamic (CFD) solver is used for the airway or drift, which has the heat, moisture, and air flow and the rockmass is solved by a Numerical Transport Code Functionalization (NTCF) model (Danko, 2006).

### 4.1.1 Integrated-parameter Computational Fluid Dynamic (CFD) model elements for the airway

This model elements are developed based on the energy balance equation governed by Fourier' second law, contaminant balance equation governed by Ficks's second law, and the Navier-Stokes momentum balance equations. Figure 4-1 illustrates the domain coordinates for airway.

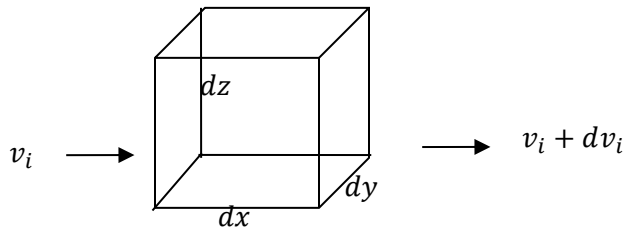


Figure 4-1. Domain coordinates.

Equation 4-1 depicts the energy balance equation in the CFD model which is governed by Fourier's second law used in a simplified form (Danko, 2013).

$$\rho c_p \frac{\partial T}{\partial t} + \rho c_p v_i \frac{\partial T}{\partial x} = \rho c_p a \frac{\partial^2 T}{\partial x^2} + \rho c_p a \frac{\partial^2 T}{\partial y^2} + \rho c_p a \frac{\partial^2 T}{\partial z^2} + \dot{q}_h \qquad (4\text{-}1)$$

with $k = \rho c_p a$

where, $k$ is thermal conductivity, $T$ is the temperature, $\rho$ is the density of moist air; $c_p$ is the specific heat of moist air; $a$ is the molecular or eddy thermal diffusivity for laminar or turbulent flow; $q_h$ is the latent heat source or sink for condensation or evaporation and $v_i$ is air velocity in flow channel $i$ in a discretized flow network model.

This equation is discretized and solved numerically and simultaneously along all parallel flow channels for the temperature field T in MULTIFLUX.

Equation 4-2 shows the species contaminant model equation in the air space that maybe described by Fick's second law (Danko, 2013).

$$\rho \frac{\partial c}{\partial t} + \rho v_i \frac{\partial c}{\partial x} = \rho D \frac{\partial^2 c}{\partial x^2} + \rho D \frac{\partial^2 c}{\partial y^2} + \rho D \frac{\partial^2 c}{\partial z^2} + \dot{q}_c \qquad (4\text{-}2)$$

where $\rho$ is density of the air and gas mixture in the air space, $x$, $y$ and $z$ are Cartesian coordinates, $t$ is time, $c$, $D$ and $q$ are respectively concentration, diffusion coefficient and mass flux source of a given gas species and $v_i$ is air velocity in flow channel $i$ in a discretized flow network model.

Equations 4-3a, 4-3b, and 4-3c depict the momentum equations for the three dimensional flow of the bulk air-moisture mixture in the ventilation network which is governed by the Navier–Stokes equation in its simplified form for flow channels along given grid lines (Danko, 2013).

$$\rho(\frac{\partial v_x}{\partial t} + v\nabla v_x) = \rho g_x - \partial \frac{Pb}{\partial x} + F_x \qquad (4\text{-}3a)$$

$$\rho(\frac{\partial v_y}{\partial t} + v\nabla v_y) = \rho g_y - \frac{\partial Pb}{\partial y} + F_y \qquad (4\text{-}3b)$$

$$\rho(\frac{\partial v_z}{\partial t} + v\nabla v_z) = \rho g_z - \frac{\partial Pb}{\partial z} + F_z \qquad (4\text{-}3c)$$

where $v_x$, $v_y$ and $v_z$ are velocity components of vector $v$, $g_x$, $g_y$ and $g_z$ are gravitational forces which include buoyancy in $x$, $y$ and $z$ directions, $Pb$ is total mixture pressure and $F_x$, $F_y$ and $F_z$ are viscous and kinetic dissipation terms. Note the $\frac{\partial v_x}{\partial t}$, $\frac{\partial v_y}{\partial t}$ and $\frac{\partial v_z}{\partial t}$ terms in equations (4-3a), (4-3b), and (4-3c), accounting for the inertia forces for accelerating or stopping the air flow that may be significant in long airways in terms of response time in the change of velocity due to starting or stopping a fan or adjusting an air regulator.

### 4.1.2 NTCF model element for the rockmass

The rockmass domain requires a Porous-Media Hydrothermal Code (PMHC). Any code capable of modeling coupled thermal hydrologic processes such as NUFT and TOUGH2 can be used as the PMHC. The Numerical Transport Code Functionalization (NTCF) solver is a surrogate model for rockmass response in heat, moisture, and contaminant. The NTCF pre and post-processes the computational results of the PMHC to model the time-dependent heat and moisture flow in the rockmass around a drift (Danko et al, 2008).

### 4.1.3 Coupled solution between the NTCF and CFD model-elements

In order to achieve a common solution of the rock-air interface, the two distinct domains have to be coupled. This is made possible by an innovative system solution method used in MULTIFLUX (Danko, 2008). The NTCF (modeling the strata heat response) and the integrated-element CFD (modeling the in-drift processes) are coupled on the rock-air interface by MULTIFLUX until the heat and moisture fluxes are balanced at the common surface temperature and partial vapor pressure at each surface node and time instant. Inner iteration loops are used to balance the in-rock and in-drift transport processes on the rock-air interface. The air flow balance iteration is executed first between the NTCF and airway CFD models for each time division. The heat flow balance iteration between the NTCF and airway CFD models for each time division is performed. Also, the moisture flow balance iteration between the NTCF and airway CFD models for each time division is performed. An additional outer iteration is also executed, which is the air flow field re-calculation with balanced thermal and moisture transport. The nested iterations continue until full convergence is achieved.

### 4.1.2 Heat, moisture, air, and contaminant constitutive equations for a branch (airway channel)

An airway with flow from the entry point, *i*, to the exit point, *j*, is governed by the flowing transport equations for the air space shown below. *i* and *j* are called nodes (Danko, 2008). The schematics are illustrated in Figure 4-2a, 4-2b, 4-2c, and 4-2d for heat, moisture, air-vapor mixture and contaminant, respectively,

a. Heat

$$qh = \frac{\Delta T}{Rh} \tag{4-4}$$

b. Moisture

$$qm = \frac{\Delta \omega}{Rm} \tag{4-5}$$

c. Air-vapor mixture

$$qa = \frac{\Delta Pb}{Ra} \tag{4-6}$$

d. Contaminant

$$qc = \frac{\Delta C}{Rc} \tag{4-7}$$

where *qh* is heat flux, *qm* is moisture flux, *qa* is the air-vapor mixture mass flux, and *qc* is contaminant flux. *Rh*, *Rm*, *Ra*, *Rc* are resistances. $\Delta T$, $\Delta \omega$, $\Delta Pb$, and $\Delta C$ are the temperature difference, vapor mass fraction difference, pressure difference, and concentration difference, respectively. Potential differences drive the transport fluxes: heat flux by$\Delta T$, moisture flux by $\Delta \omega$, air-vapor mixture mass flux by $\Delta Pb$, and, contaminant flux by $\Delta C$. Connecting resistances between network nodes form networks. Figure 4-3 demonstrates the network models for airflow, heat, moisture, and contaminant species that are coupled

in MULTIFLUX. The network nodes represent finite volumes or finite surface areas in the model domain. The conservations of the flow of heat, moisture, and air are represented by the connection of the branches at its nodes. The constitutive equations are represented by the branches of the network.

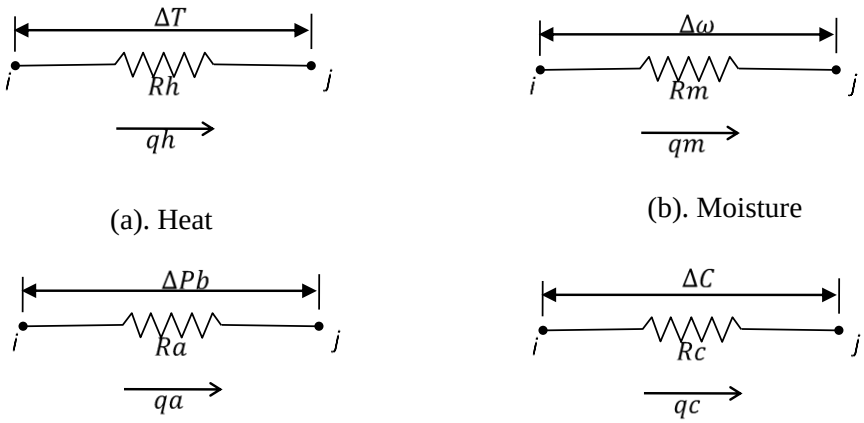


(a). Heat

(b). Moisture

(c). Air-vapor

(d). Contaminant

Figure 4-2. Schematics for heat, moisture, air-vapor, and contaminant governing equations (Danko, 2008)

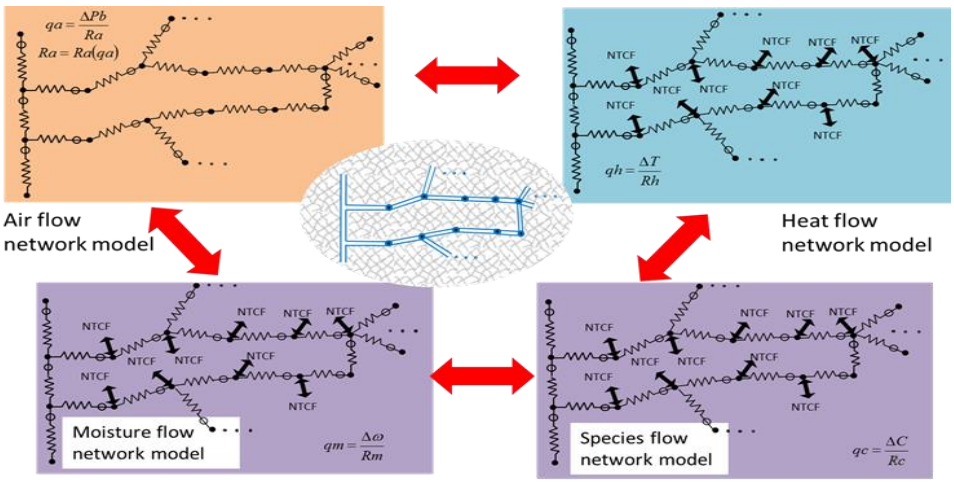


Figure 4-3. Coupled transient transport processes in MULTIFLUX (Danko, 2008)

### 4.1.3 Comparison of network solution solver model to CFD model

CFD is a numerical modeling technique that solves the system of mass, energy, and momentum conservation differential equations to determine a detailed representation of the airflow, temperature, and contaminant conservation at each of these nodes. In order to achieve this hundreds or thousands of nodes needs to be discretized for a zone. And as such it limits its capability to model an entire mine which has a larger network.

Nonetheless, fluid flow behavior in underground mine working areas has been modeled with CFD. Examples are modeling of ventilation and methane behavior of that a dead end roadway in a underground coal mine ( Torano et al, 2009) and modeling of methane flow through permeable strata around a longwall face in underground coal mine (Ren and Edwards, 2000).

## 4.2 Time-dependent methane contaminant concentration simulation for hazardous scenarios

This section is taken from the final report for an Alpha foundation funded project (Danko et al, 2016) for which I worked as a research assistant for two and half years and was instrumental in the report write up.

Five scenarios that could lead to methane concentration increase are modeled and checked in forward-predicting mode for testing the EWS, including:

(1) Methane in-burst from encountering a pocket at the face

(2) Airway blockage as a result of partial collapse of a hazardous roof section in a mine

(3) Atmospheric barometric pressure variations causing methane inflow from the gob

(4) Booster fans malfunction; fan starts or stops can cause barometric pressure variation that may trigger pressure unbalances and methane inflow from sealed areas, seams, or gob

(5) Fire heat load

Table 4-1 summarizes the five modeled scenarios in two coal mine examples depicted in Figures 4-6 and 4-10, respectively. Eighteen selected observed locations are marked in the model. These locations are represented in the model using markers called “dynamic monitors” in Ventsim. The observed locations include assumed monitoring sensor locations and critical location (not necessarily monitored) determined by knowing the dangerous spots in the mine.

The modeling process is performed in two parts. First, the VAM model is used and data are generated from it emulating sensors’ output. Second, the emulated sensor signals from some observed locations from the VAM results are used as assumed monitored data input to trigger the EWS system at 0.5% methane. Note that the sensor signals are also used for the APPS predictor continuously. Once the 0.5% methane concentration threshold limit value is crossed at any sensor, the EWP is triggered, which starts with a root-cause analysis and an APPS forward prediction at locations that may not be necessarily monitored. If the forward-predicted values lead to a threshold crossing of 1% methane for stopping work in a coal mine (CFR 30 Part 75.323, 1996), a warning alarm is triggered. The delay time, which is the time required for the methane concentration to cross the threshold limit value of 1% for a particular critical location is determined from the time the sensor trips the EWP forward prediction at 0.5% methane as a reference time. The delay time minus the computational time of the APPS predictor is available as advance time for warning. This approach is used in all five EWS capacity demonstration examples. The APPS prediction

simulation takes approximately 2 minutes from the time a sensor crosses the 0.5% methane threshold to the time of finishing the forward prediction at the (1% methane) threshold limit value crossing at a critical location, which might not be necessarily monitored. The simulation time of approximately 2 minutes has to be deducted from the delay time to determine the actual time gain for management to take action.

The time-dependent methane concentration results for each of the five scenarios are presented in three parts: (a) the native VAM model simulation results; (b) the emulated sensor signals used as monitored data input to trigger the EWS system; and (c) the APPS model forward prediction signals starting from an early threshold crossing of monitored signals to check and issue EWS alarm if needed.

Table 4-1. Modeled hazardous scenarios used in demonstrational examples (Danko et al, 2016).

| | | |
|---|---|---|
| Scenario 1A (Base case for scenarios 2 and 3) | Methane in-burst (2 sources) | Mine example 1 |
| Scenario 1B | Methane in-burst (3 sources) | Mine example 1 |
| Scenario 1C(Base case for scenarios 4 and 5) | Methane in-burst (3 sources) | Mine example 2 |
| Scenario 2 | Airway blockage | Mine example 1 |
| Scenario 3 | Atmospheric barometric pressure variations | Mine example 1 |
| Scenario 4 | Fans malfunction | Mine example 2 |
| Scenario 5 | Fire heat load | Mine example 2 |

### 4.1.1 Methane in-burst from encountering a pocket at the face

Gas in-burst is considered when inflow of methane gas from the strata enters the mine airway due to e.g., face collapse, roof collapse, leakage from a gas pocket due to cracks in the strata, or water inflow that may be accompanied by methane. The gas inflow is caused by opening of a pathway to ventilating air. Methane in-burst is a hazardous event and is more likely to occur in coal mines, illustrated in Figure 4-4.

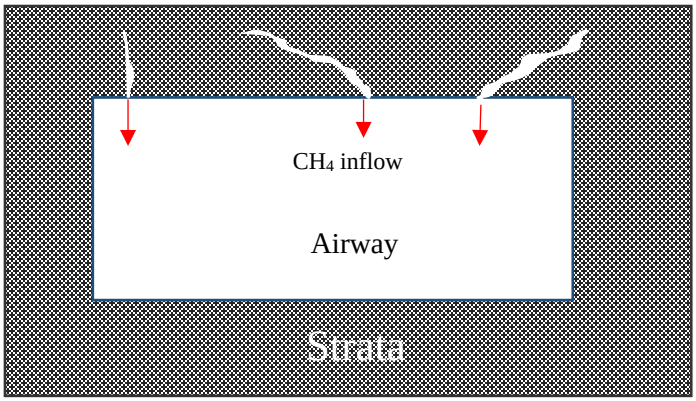


Figure 4-4. Gas inflow from strata (Danko et al, 2016).

Two examples are demonstrated in a longwall coal mine assuming two different methane source arrangements. This coal mine has 766 branches and 3 surface fans. The ventilation around the panel is facilitated using a three entry headgate, a single entry tailgate, a three entry bleeder, and a fringe ventilation path, which utilizes a small amount of intake air provided to the outside edges of the gob to ventilate any accumulation of gases. Three potential methane gas sources S1, S2, and S3 are assumed in the mine at three different locations, shown in Figure 4-5 with S1 in one of the longwall intake airways (branch 758), S2 at the working face (branch 761), and S3 in the longwall return airway (branch 760). S1, S2, and S3 only serve as methane gas input locations. Figure 4-6 illustrates the layout of the mine model with 18 observed locations of interest. All or only some of the marked-up locations may be used as monitored locations from which, the signals are used in real-time to trigger the EWP for forward predictions. The roles of the monitored signals, always in real-time, are (a) to trigger the EWP and start, if needed, a forward prediction by the fast APPS predictor; and (b) to serve for supporting the APPS corrector. Some or all of the same “observed” locations (or any other locations included in the mine ventilation network) are used in the hazard analysis by the APPS predicator in the accelerated,

simulation time. The APPS predictor uses the same model as the APPS corrector, but the two processes run in parallel and on two very different time scales. If the two time scales are the same, no advance warning is possible. This is the reason for using high-performance simulation technique such as provided by MULTIFLUX. The area of investigation for methane in-burst in the two mines examples is the working face.

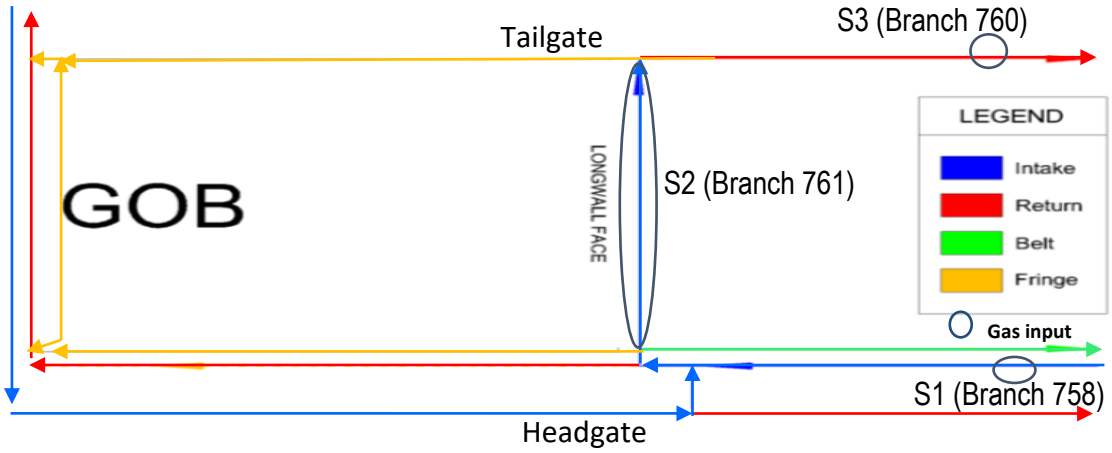


Figure 4-5. Schematic of modeled section showing areas of gas inflow with source locations for coal mine example 1 (Jong et al, 2013).

#### 4.1.1.1 Two methane sources (Scenario 1A, coal mine example 1)

Gas in-burst is modeled first by injecting only two methane sources at S2 (line load, across the entire longwall face, 55 liters/second/100m of $CH_4$) and S3 (point source, 50% $CH_4$ at 0.1$m^3$/s). The simulation results for selected locations with significant changes only are plotted. The time-dependent VAM results for methane concentration are demonstrated in Figure 4-7a. The emulated sensor signals used as monitored data input to trigger the EWS system is shown in Figure 4-7b. Figure 4-7c depicts the APPS model forward prediction results for observed locations 15 and 17 based on the 0.5% methane crossing at assumed

sensor 15. The results for airflow, velocity, and absolute pressure do not show any changes at the observed locations. A threshold limit value of 1% methane for stopping work is used in this analysis. Using 0.5% methane for a safety assumption to start a forward prediction and using branch 742 (monitoring sensor 15), which is a sensor location just at the end of the active face as a reference, the delay time in methane front arrival can be estimated. Branch 742 reaches 0.5% in 21 minutes and branch 760 reaches 0.8% in 33 minutes and remains constant as illustrated in Figure 4-7c. Therefore, the delay time before branch 760 (forward predicted signal at observed location 17 downstream of branch 742 on the return airway), reaches a maximum concentration is 12 minutes (33 minutes minus 21 minutes) in real-time. The computational overhead in forward-prediction simulation time is 2 minutes, negligible in this case. Therefore, 10 minutes is available for advance notice (12 minutes minus 2 minutes forward prediction time). Nevertheless, it is observed that the methane concentration remains below the threshold value of 1% for EWS alarm and no warning is necessary.

#### 4.1.1.2 Three methane sources (Scenario 1B, coal mine example 1)

Gas in-burst is modeled by injecting three methane sources, adding an extra gas source, S1 (80% $CH_4$ at 0.2 $m^3/s$) at the upstream of the working face in addition to S2 and S3 with the same concentrations and flow rates as in Scenario 1A. The same sensor locations are used. The simulation results for selected locations with significant changes only are plotted. The time-dependent VAM results for methane concentration are demonstrated in Figure 4-8a. The emulated sensor signals used as monitored data input to trigger the EWS system is shown in Figure 4-8b. Figure 4-8c depicts the APPS model forward prediction results for

observed locations 15 and 17 based on the 0.5% methane crossing at assumed sensor 15. There is a slight increase in methane concentrations in branch 760, which is a return airway downstream of the methane sources. The concentration crosses the threshold limit compared to that of the previous scenario 1A, where only two methane sources are used. This indicates that there is a possibility of threshold crossing from unknown methane source accumulation as the air flows downstream. A threshold limit value of 1% methane for stopping work is used in this analysis. The air parameters (airflow, velocity, and absolute pressure) are unaffected by the increase in methane sources from the results. Using 0.5% methane for a safety assumption to start a forward prediction and using branch 742 (monitoring sensor 15), which is a sensor location just at the end of the active face as a reference, the delay time in methane front arrival can be estimated. Branch 742 reaches 0.5% in 21 minutes and branch 760 reaches 1% in 52 minutes as illustrated in Figure 4-8c. Therefore, the delay time before branch 760 (forward predicted signal at observed location 17 downstream of branch 742 on the return airway, not necessarily monitored), crosses the threshold is 31 minutes (52 minutes minus 21 minutes) which triggers an EWS alarm. Since threshold crossing occurs, the gain time for management to take action is 29 minutes (31 minutes minus 2 minutes forward prediction time).

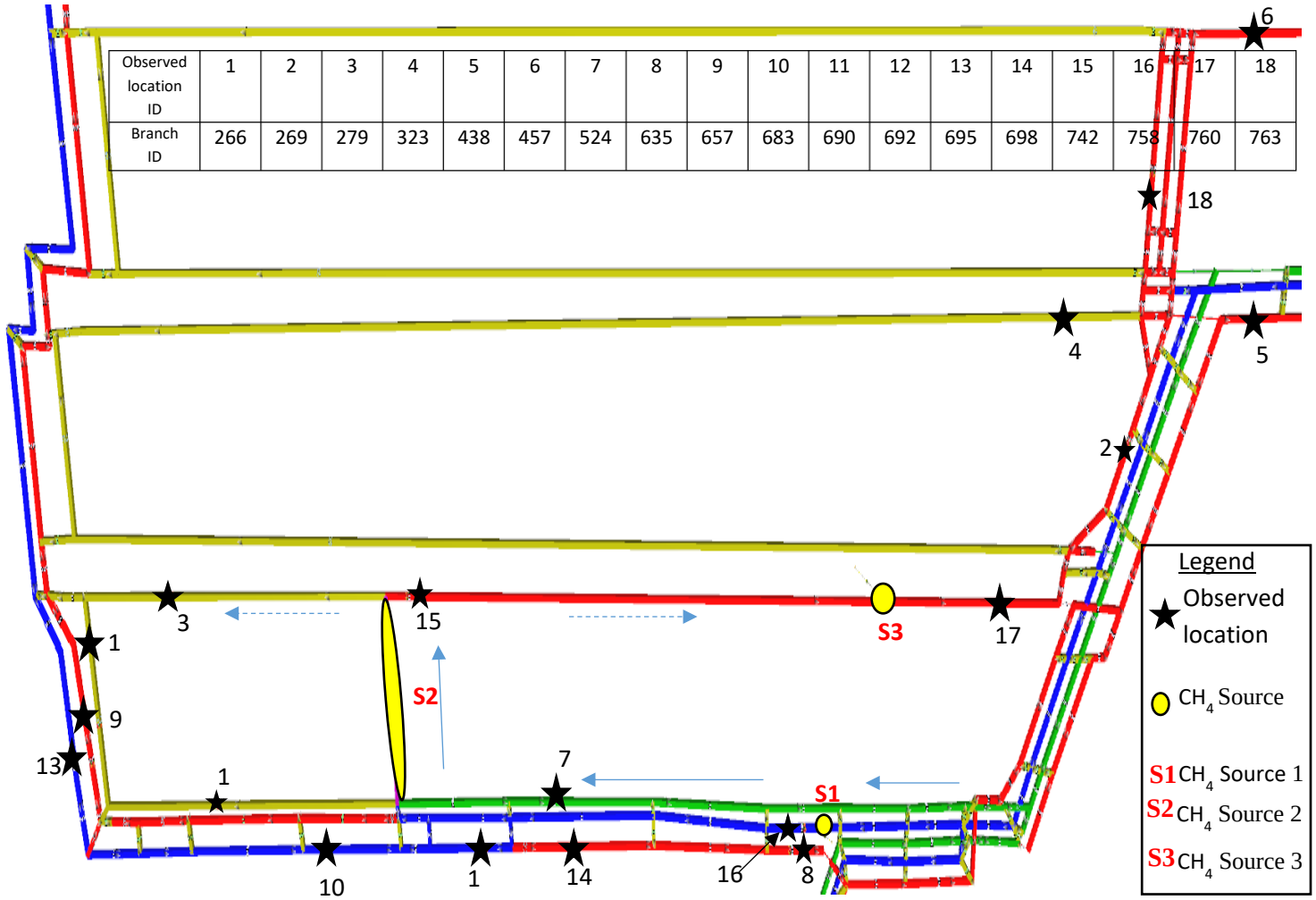


Figure 4-6. Layout of coal mine example 1 with methane sources and assumed monitored sensor locations in Ventsim (Danko et al, 2016).

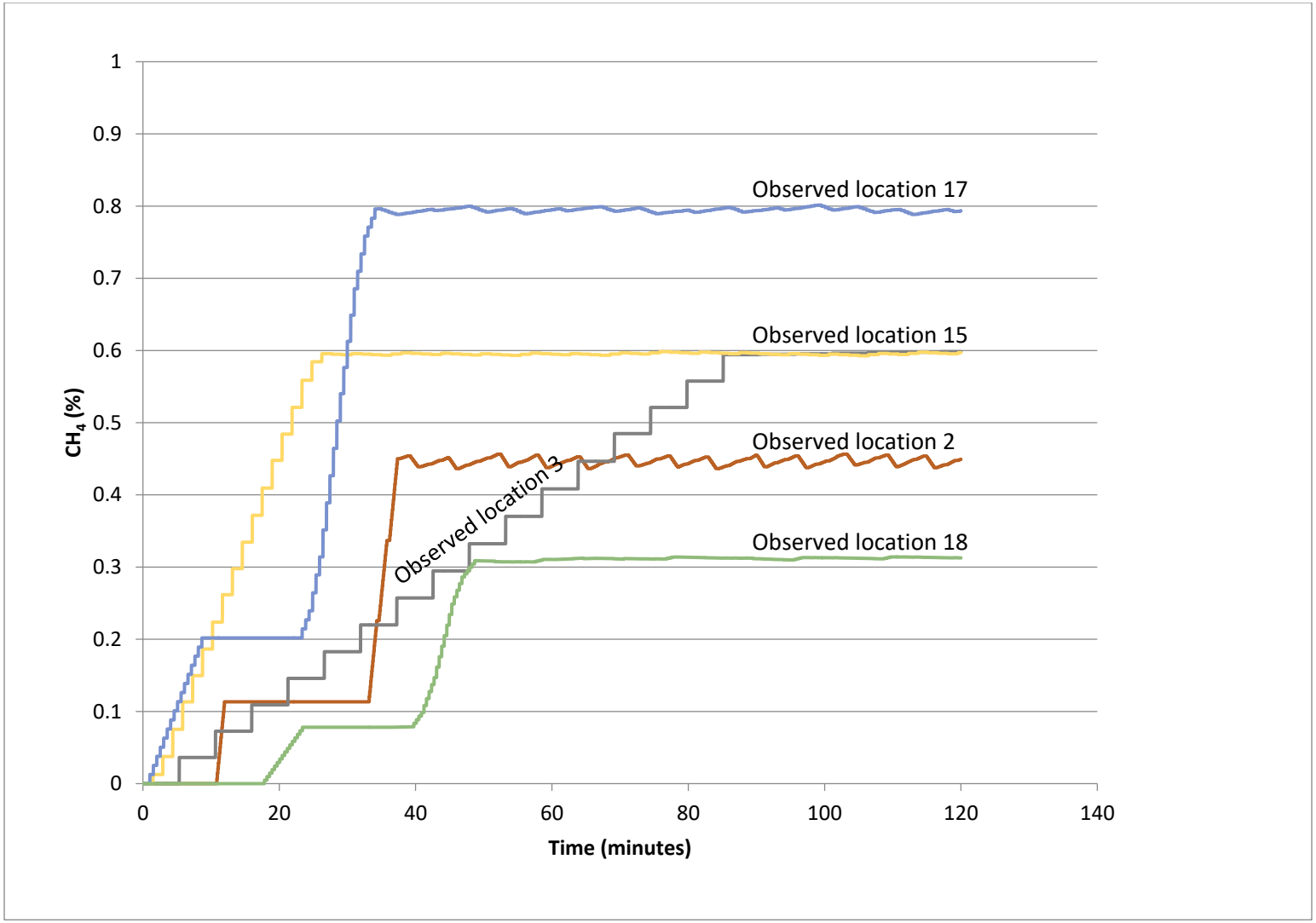


Figure 4-7a. Results of methane concentration at selected observed locations from native VAM simulation in Scenario 1A. Selected locations with significant changes only are plotted (Danko et al, 2016).

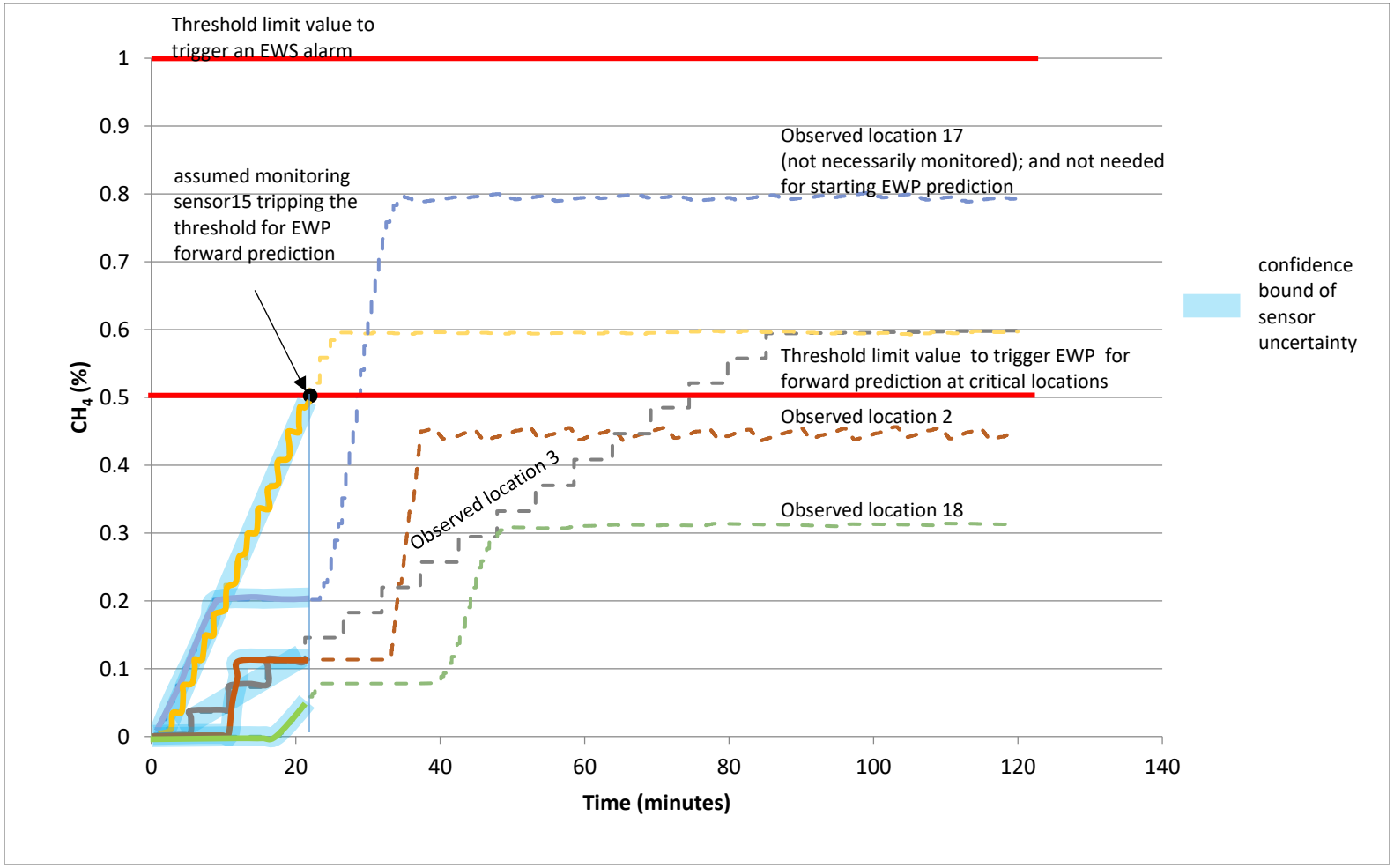


Figure 4-7b. Emulated sensor signals used as assumed monitored data input to trigger the APPS forward predictor in the EWS system in Scenario 1A (shown in thick lines with confidence bounds). Assumed sensor 15 (and 17 if installed) trip(s) threshold for EWP forward prediction. The curves show real-time changes in $CH_4$ concentration. Selected locations with significant changes only are plotted. Note that the sensor signals are also used for the APPS predictor continuously (shown in dashed lines) (Danko et al, 2016).

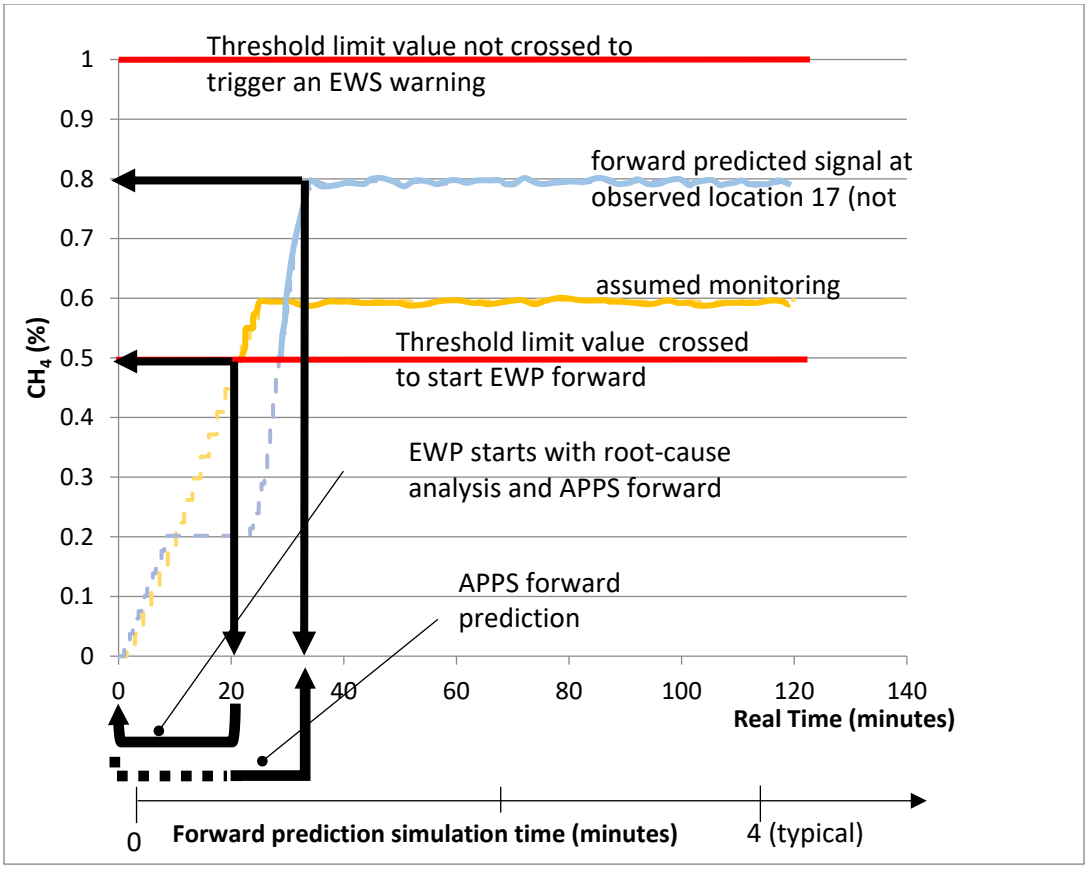


Figure 4-7c. APPS model forward prediction at selected observed locations in real-time and in fast simulation time scales for Scenario 1A. Only two selected locations are shown (Danko et al, 2016).

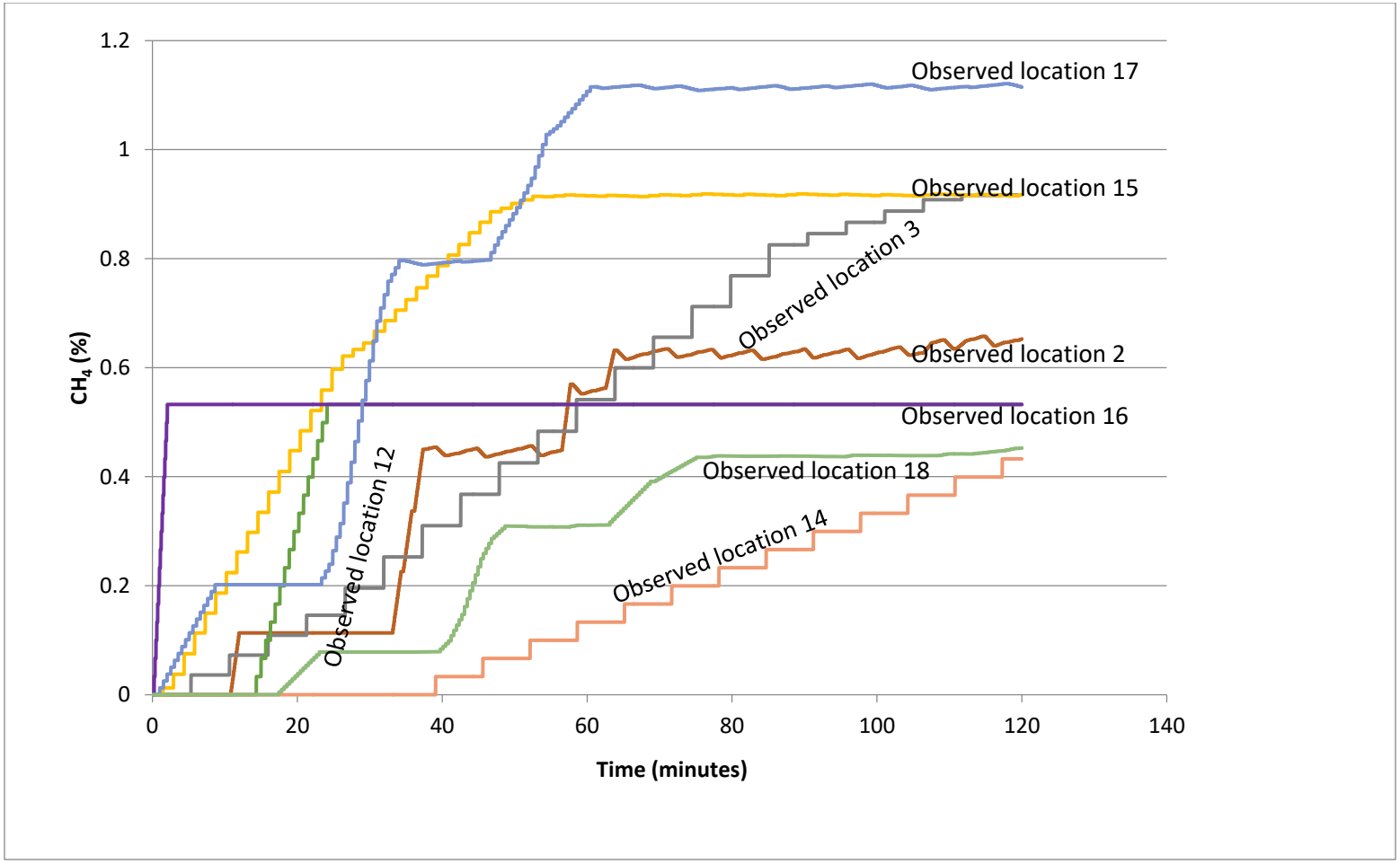


Figure 4-8a. Results of methane concentration at selected observed locations from native VAM simulation in Scenario 1B. Selected locations with significant changes only are plotted (Danko et al, 2016).

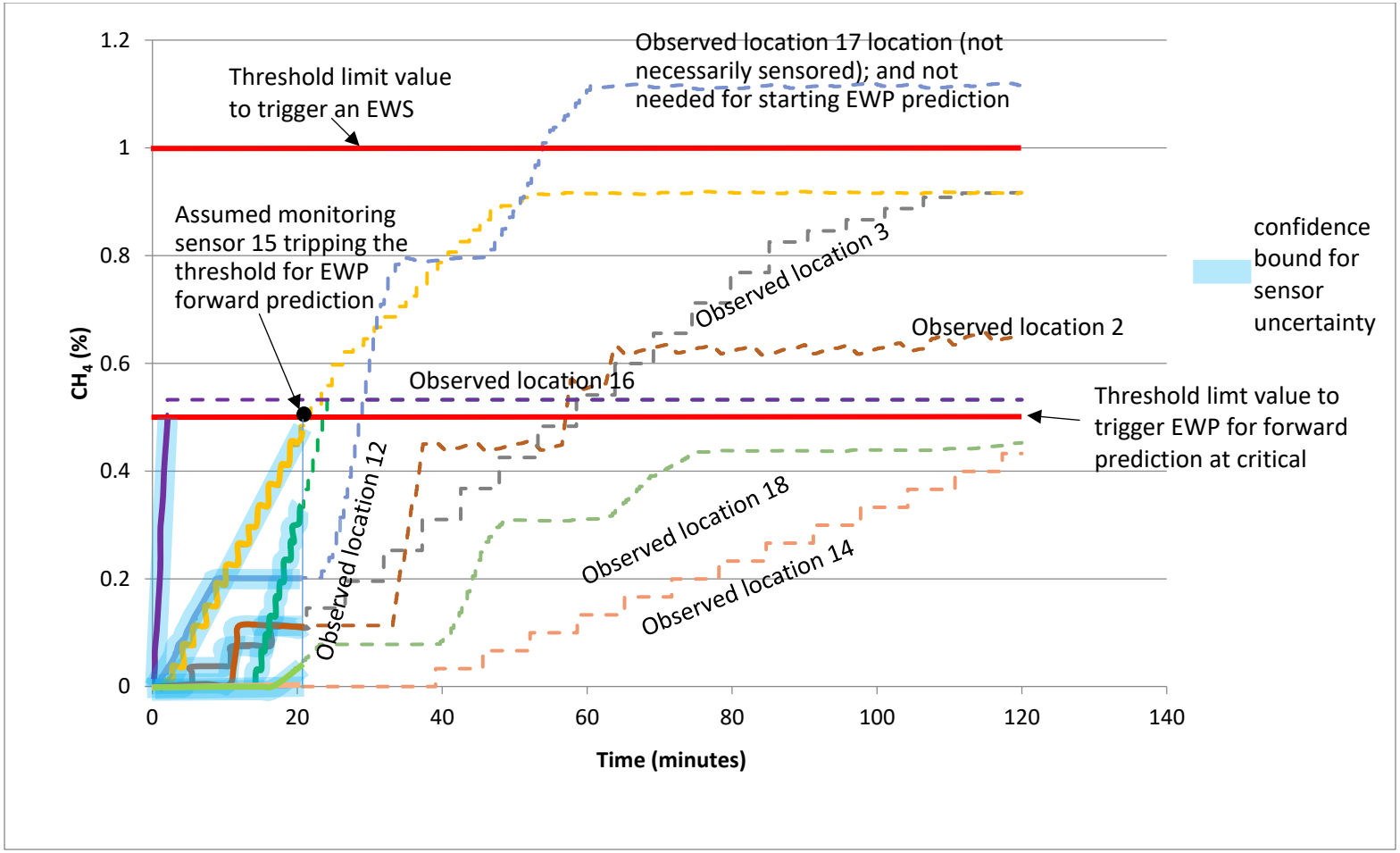


Figure 4-8b. Emulated sensor signals used as assumed monitored data input to trigger the EWS system in Scenario 1B (shown in thick lines with confidence bounds). Assumed sensors 15, 12, 16 (and 17 if installed) trip threshold for EWP forward prediction (sensor 16 is too close to threshold to trip). The curves show real-time changes in $CH_4$ concentration. Selected locations (with significant changes only) are plotted. Note that the sensor signals are also used for the APPS corrector continuously (shown in dashed lines) (Danko et al, 2016).

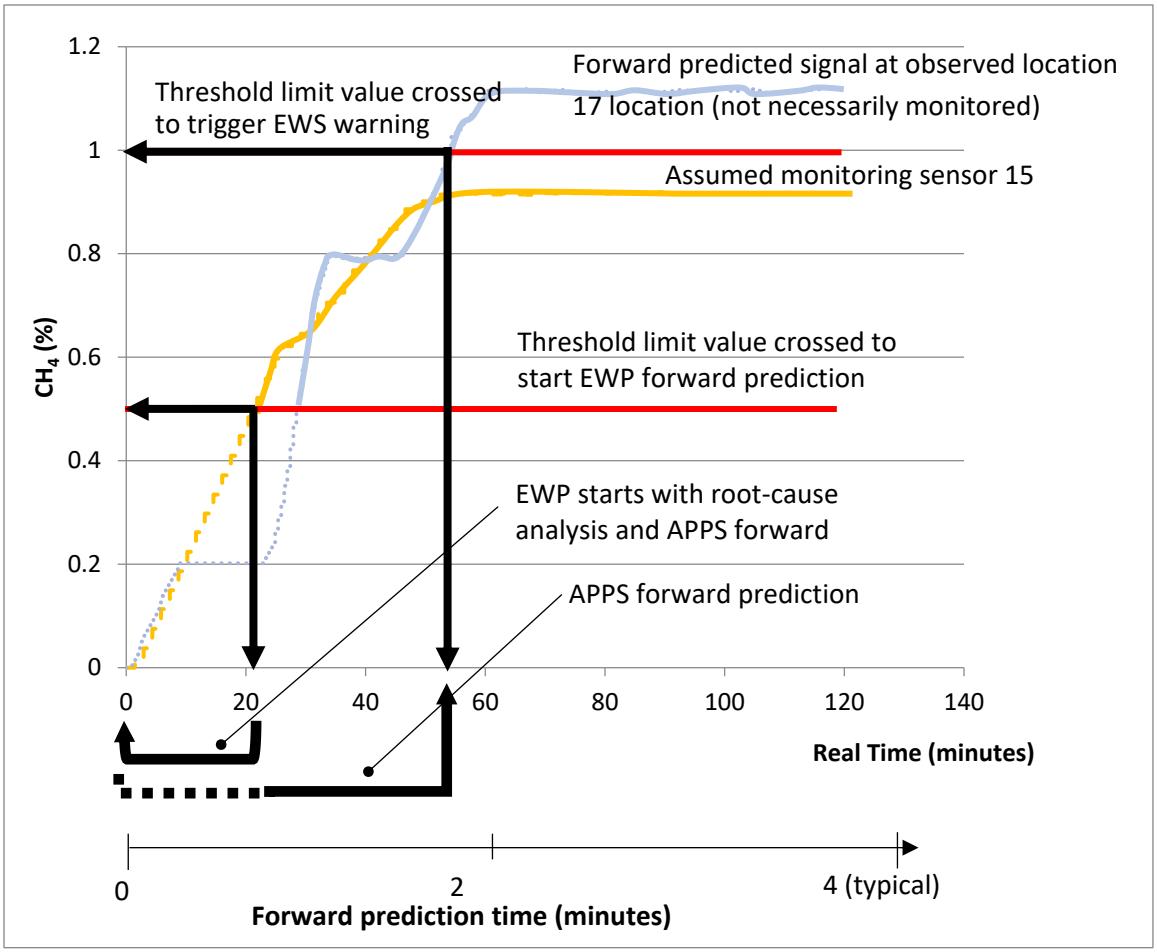


Figure 4-8c. APPS model forward prediction at selected observed locations in real-time and in fast simulation time scales for Scenario 1B. Only two selected locations are shown (Danko et al, 2016).

#### 4.1.1.3 Three methane sources (Scenario 1C, coal mine example 2)

Coal mine 2 is used to model three methane sources. This coal mine example is converted from a native VnetPC model with 253 branches and 2 fans. The panel in this coal mine is ventilated by delivering fresh air through three entries, two from the headgate and one from the tailgate. The contaminated air is exhausted through back bleeder return airways. Three methane gas sources S1, S2, and S3 are injected into the mine at three different locations shown in Figure 4-9 with S1 in one of the longwall intake airways (branch 249), S2 at the

working face (branch 100), and S3 in the longwall return airway (branch 251). Figure 4-10 illustrates the layout of the mine model with 18 observed locations of interest.

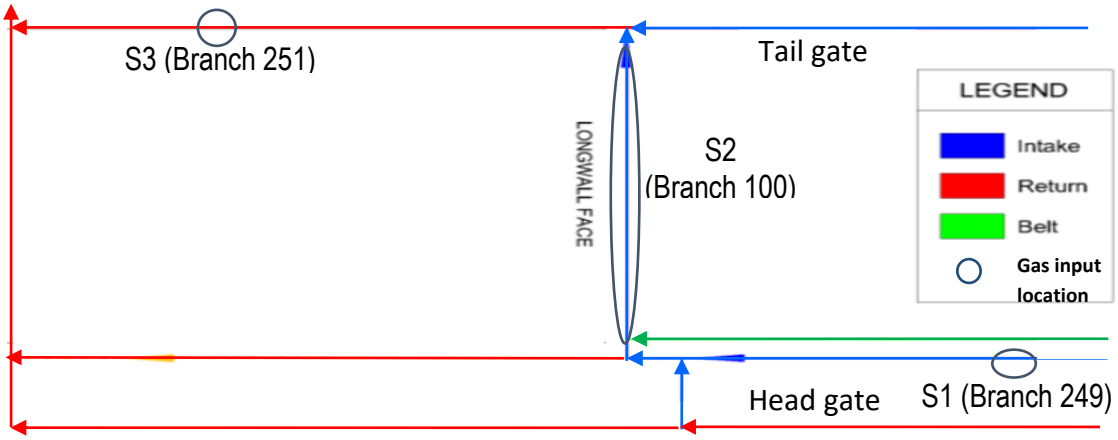


Figure 4-9. Schematic of modeled section showing areas of perturbation with source locations for coal mine example 2 (Danko et al, 2016).

Scenario 1C is studied in mine example 2 as a base scenario to demonstrate fan malfunction and fire heat load. Gas in-burst into the mine airway is modeled by injecting three methane sources at S1 (80% $CH_4$ at 0.2 $m^3/s$), S2 (line load, 55 liters/second/100m of $CH_4$) and S3 (point source, 50% $CH_4$ at 0.1$m^3/s$). The simulation results for selected locations with significant changes only are plotted. The time-dependent VAM results for methane concentration are demonstrated in Figure 4-11a. The emulated sensor signals used as monitored data input to trigger the EWS system is shown in Figure 4-11b. Figure 4-11c depicts the APPS model forward prediction results for observed locations 13 and 18 based on the 0.5% methane crossing at assumed sensor 13. The results for airflow, velocity, and absolute pressure are not shown since there are no changes at the 18 observed locations. A threshold limit value of 1% methane for stopping work is used in this analysis and from the results. It is observed that the methane concentration is below the threshold limit for all

the 18 assumed monitored locations. Using 0.5% methane for a safety assumption to start a forward prediction and using branch 219 (monitoring sensor 13), which is a sensor location just at the end of the active face as a reference, the delay time in methane front arrival can be estimated. Branch 219 reaches 0.5% in 7 minutes and branch 251 reaches 0.8% in 17 minutes and remains constant as illustrated in Figure 4-11c. Therefore, the delay time before branch 251 (forward predicted signal at observed location 18 downstream of branch 219 on the return airway, not necessarily monitored), reaches a maximum concentration in 10 minutes (17 minutes minus 7 minutes). Hence, 8 minutes are available for advance notice (10 minutes minus 2 minutes forward prediction time). However, it is observed that the methane concentration remains below the threshold value for the observed location 18 and no warning is necessary.

The typical signal trends for methane in-burst are depicted in Figures 4-7a, 4-8a, and 4-11a. In order to identify gas in-burst as a root cause, the signal trends must be analyzed. There is only the methane concentration signal from the results useful for detection. The future effect of scenario 1 that can lead to a hazard is the increase in methane as a result of gas accumulation. Therefore, the gas accumulation model is a necessary and useful APPS forward predictor to evaluate the effect of methane in-burst at the face and the allowable delay time for concentration threshold crossing.

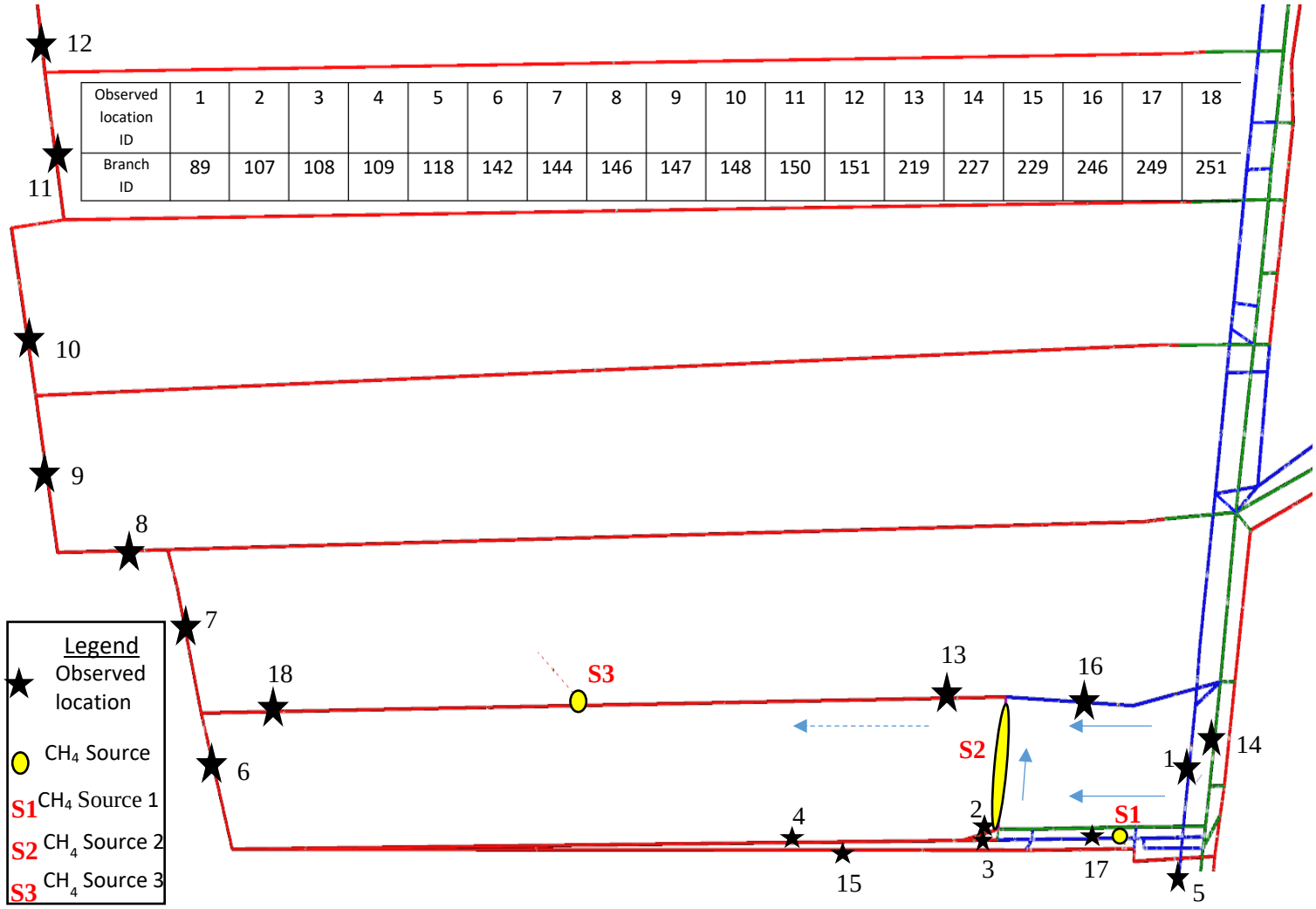


Figure 4-10. Layout of coal mine example 2 with methane sources and assumed monitored sensor locations in Ventsim (Danko et al, 2016).

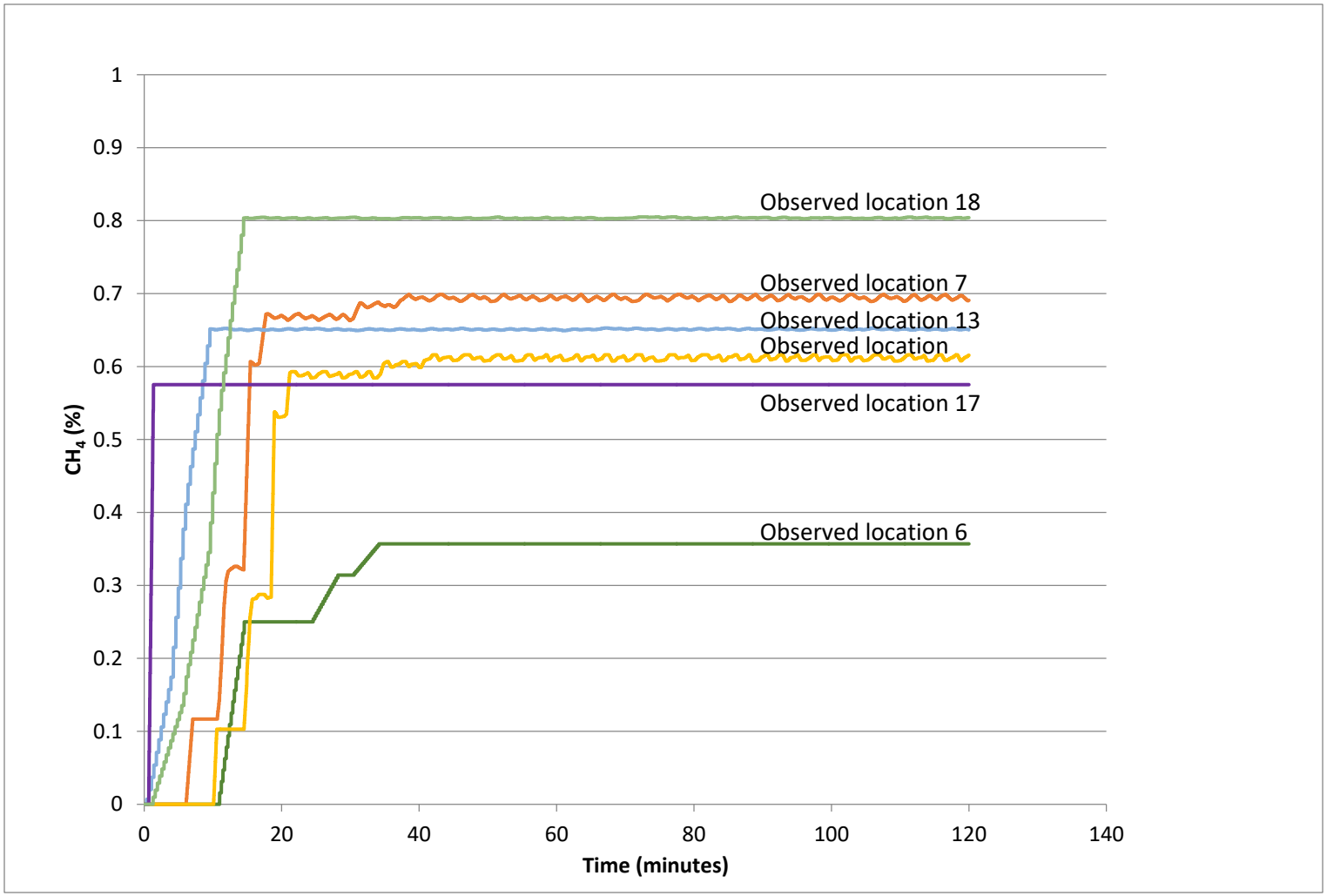


Figure 4-11a. Results of methane concentration at selected observed locations from native VAM simulation in Scenario 1C. Selected locations with significant changes only are plotted (Danko et al, 2016).

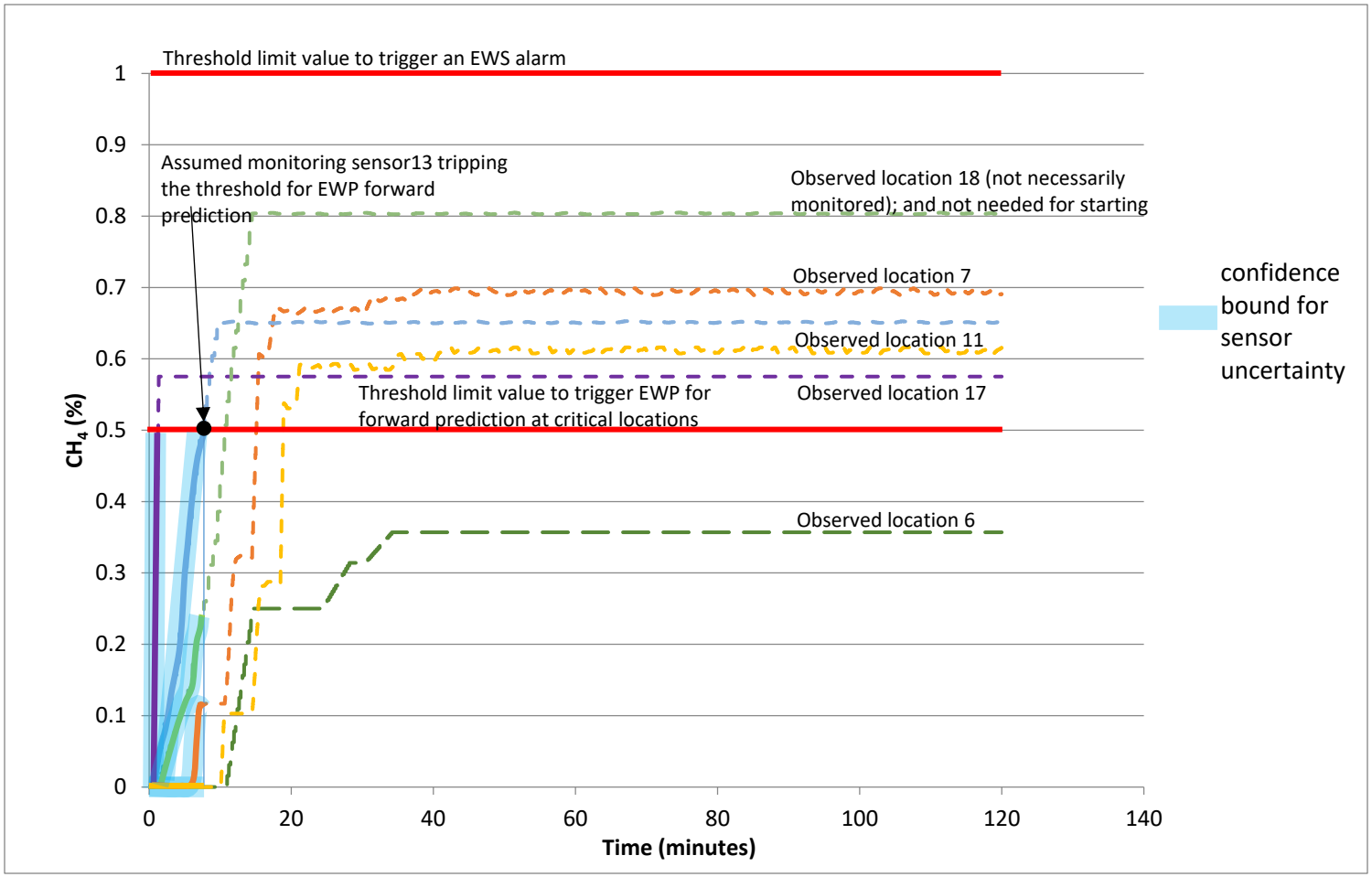


Figure 4-11b. Emulated sensor signal used as assumed monitored data input to trigger the EWS system in Scenario 1C (shown in thick lines with confidence bounds). Assumed sensors 13, 17 (and 18 if installed) trip(s) threshold for EWP forward prediction. The curves show real-time changes in $CH_4$ concentration. Selected locations with significant changes only are plotted. Note that the sensor signals are also used for the APPS predictor continuously (shown in dashed lines) (Danko et al, 2016).

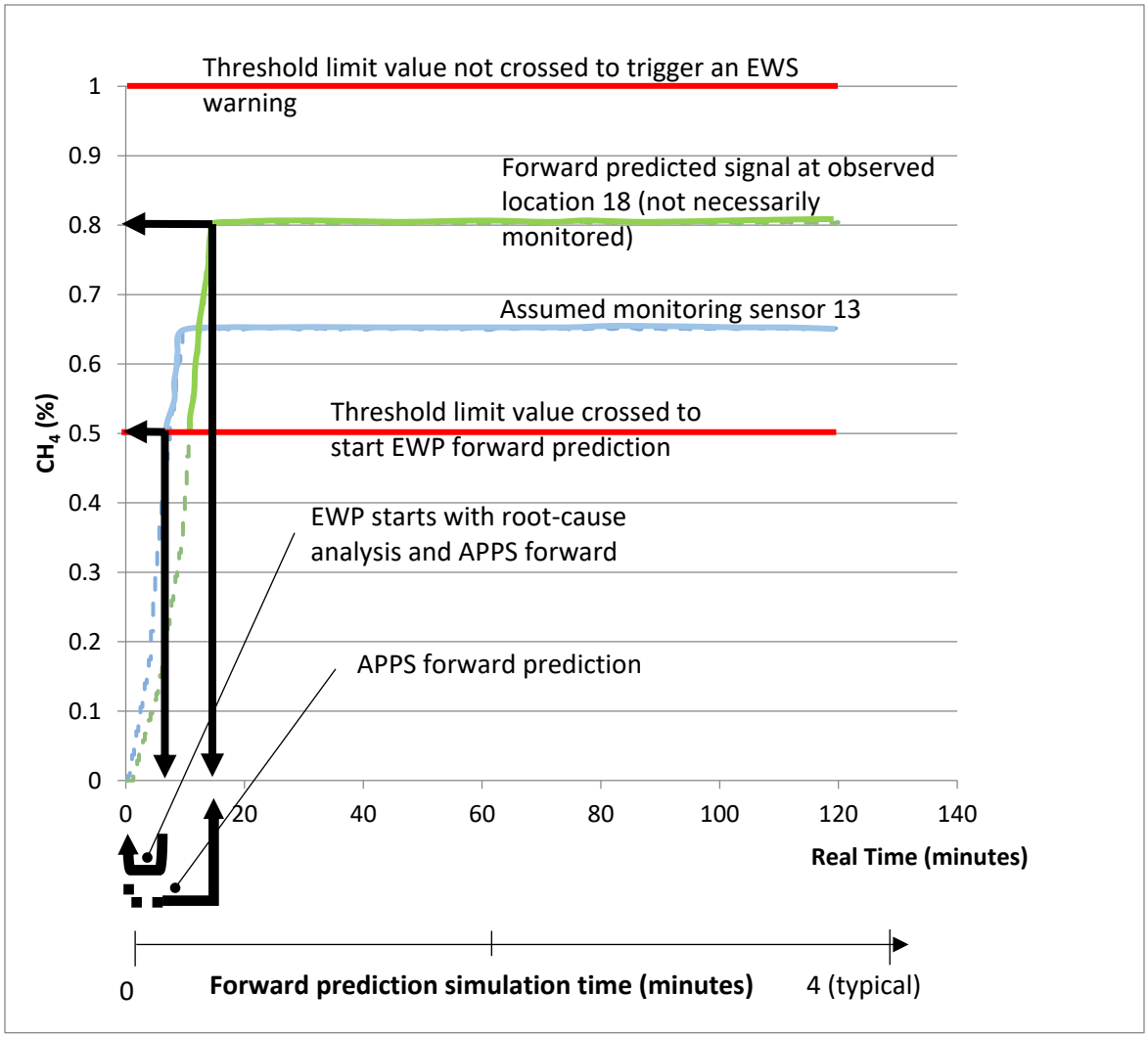


Figure 4-11c. APPS model forward prediction at selected observed locations in real-time and in fast simulation time scales for Scenario 1C. Only two selected locations are shown (Danko et al, 2016).

### 4.1.2 Airway blockage as a result of partial collapse of a hazardous roof section in the mine (Scenario 2, mine example 1)

Airway blockage may occur from a roof collapse, equipment and other malfunctions. The roof collapse is caused by ground failure. This is a dangerous but very rare type of event that could occur in mines. Airway blockage causes a decrease in airflow that results in methane concentration increase. There are two ways in which this scenario can be detected.

Firstly, the primary detection is used which comprises of ground control and roof stability sensory signals; and secondly, detection of the change in airflow, as well as in barometric pressure, and temperature. These signals must be analyzed together to collaborate in the recognition of airway blockage. Airway blockage is modeled as Scenario 2 in mine example 1. Figure 4-6 shows the layout of the mine model with 18 observed locations of interest, which is used to access the time dependent behavior of the performance elements. The signature of the primary detection parameters is a step change which directly gives the root cause and therefore there is no need for modeling. However, the secondary changes are simulated to determine the forms of signatures expected in such a scenario.

This scenario is modeled by blocking one of the intake airways (branch 758) upstream of S2 and S3 sources, after 10 minutes into a 2-hour simulation**.**

Two methane gas sources S2 and S3 are modeled. In order to mimic an airway blockage, the resistance in branch 758, which is about 3500 ft away from the longwall face is increased from 0.00170 $Ns^2/m^8$ to 8000 $Ns^2/m^8$. The area of perturbation for airway blockage is shown Figure 4-12. Blockage reduced the airflow in this branch from $30m^3/s$ to $0.1m^3/s$ depicting a total blockage with little amount of leakage.

The simulation results for selected locations with significant changes only are plotted. The time-dependent VAM results for methane concentration are demonstrated in Figure 4-13a. The emulated sensor signals used as monitored data input to trigger the EWS system is shown in Figure 4-13b. Figure 4-13c depicts the APPS model forward prediction results for observed locations 15 and 17 based on the 0.5% methane crossing at assumed sensor 15. The results for airflow, velocity, and absolute pressure are demonstrated in Figures 5-14, 5-15, and 5-16, respectively. There is an increase in airflow in some branches as well

as decrease in other branches. The results indicate that methane concentration increases with reduction in airflow that leads to threshold crossing in one branch (branch 760). A threshold limit value of 1% methane for stopping work is used in this analysis. Therefore, using 0.5% methane as a safety concentration value to start a forward prediction and using branch 742 (monitoring sensor 15), which is a sensor location just at the end of the active face as a reference and using a safety factor of 0.5% methane, the delay time can be estimated. Branch 742 reaches 0.5% in 23 minutes and branch 760 (forward predicted signal at observed location 17 downstream of branch 742 on the return airway, not necessarily monitored), reaches 1% in 46 minutes as illustrated in Figure 4-13c. Therefore, the delay time before branch 760 crosses the threshold is 23 minutes (46 minutes minus 23 minutes), which triggers an EWS alarm. Since there is a threshold crossing, the gain time for management to take action is 21 minutes (23 minutes minus 2 minutes forward prediction time).

Figure 4-13a through 4-16 depict typical trends due to an airway blockage for air parameters and concentrations. These signals are step changes. Therefore, these signal trends have to be searched for in order to determine airway blockage as a root cause. The future effect of scenario 2 is methane increase due to reduced airflow required for proper dilution. A gas accumulation model, in the form of a fast-running APPS is an adequate EWP method for this example.

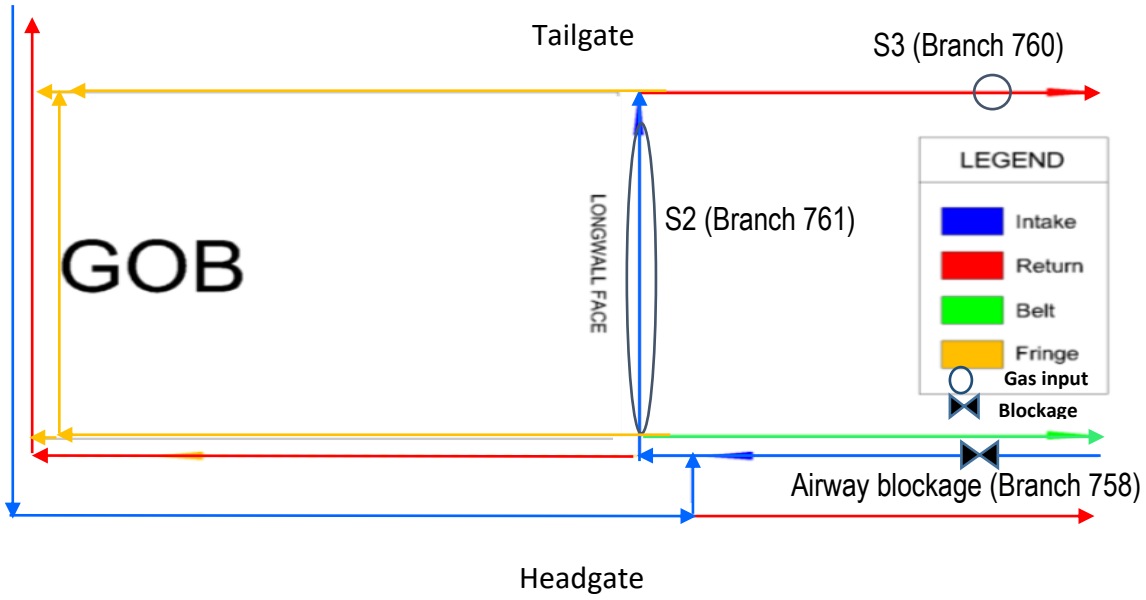


Figure 4-12. Schematic of area of perturbation for airway blockage for coal mine example 1 (Danko et al, 2016).

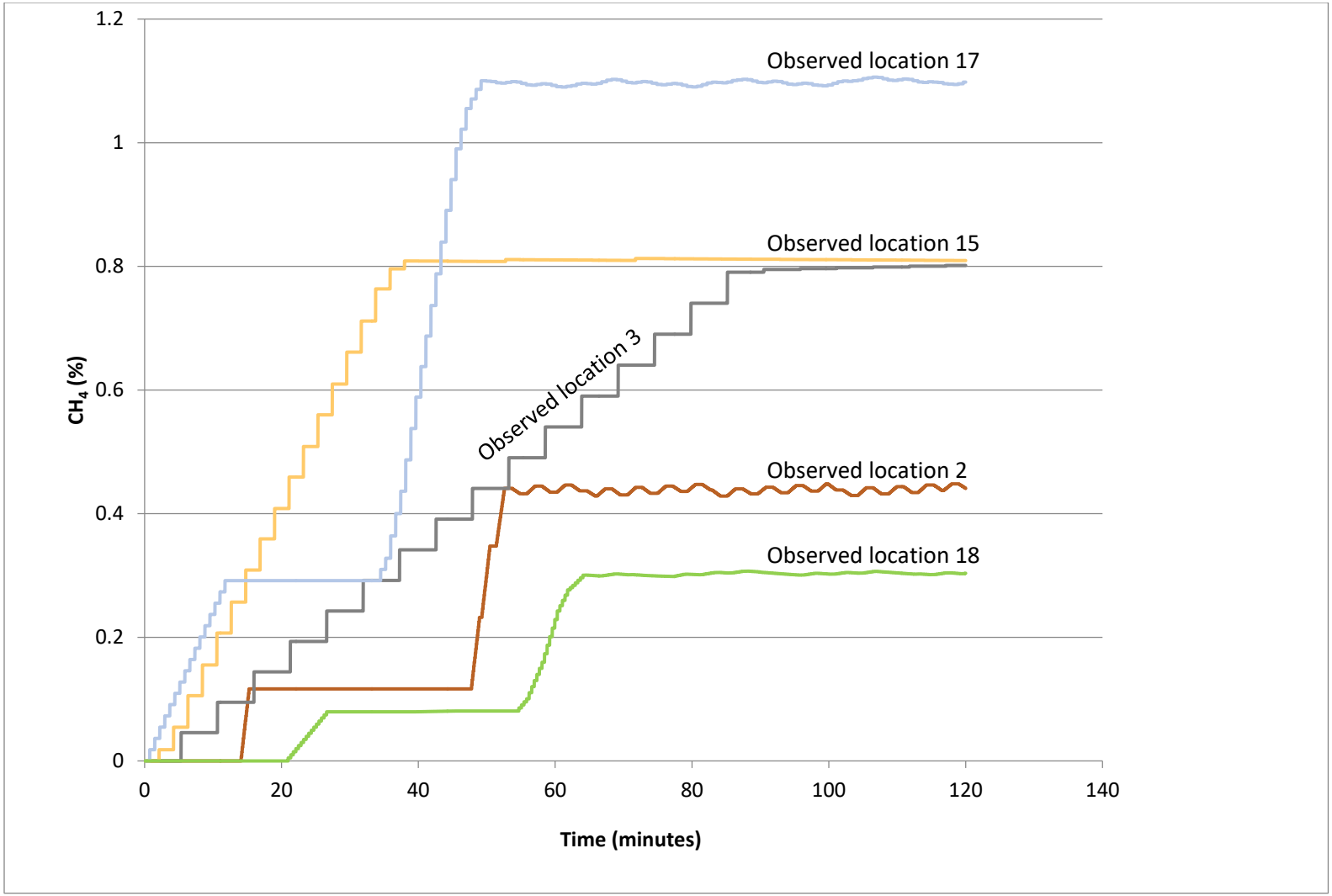


Figure 4-13a. Results of methane concentration at selected observed locations from native VAM simulation in Scenario 2. Selected locations with significant changes only are plotted (Danko et al, 2016).

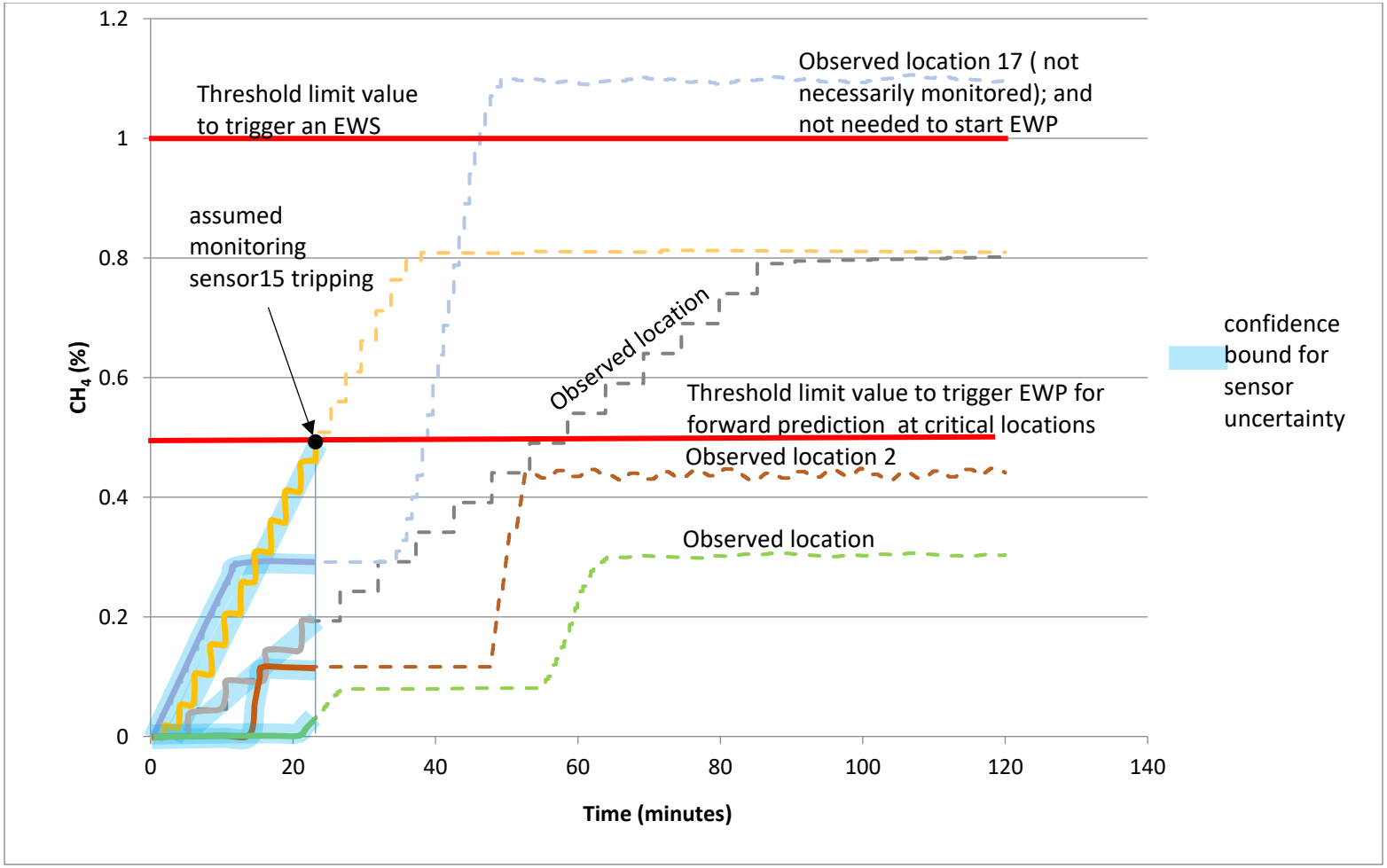


Figure 4-13b. Emulated sensor signal used as assumed monitored data input to trigger the EWS system in Scenario 2 (shown in thick lines with confidence bounds). Assumed sensors 15 (and 17 if installed) trip threshold for EWP forward prediction. The curves show real-time changes in $CH_4$ concentration. Selected locations with significant changes only are plotted. Note that the sensor signals are also used for the APPS predictor continuously (shown in dashed lines) (Danko et al, 2016).

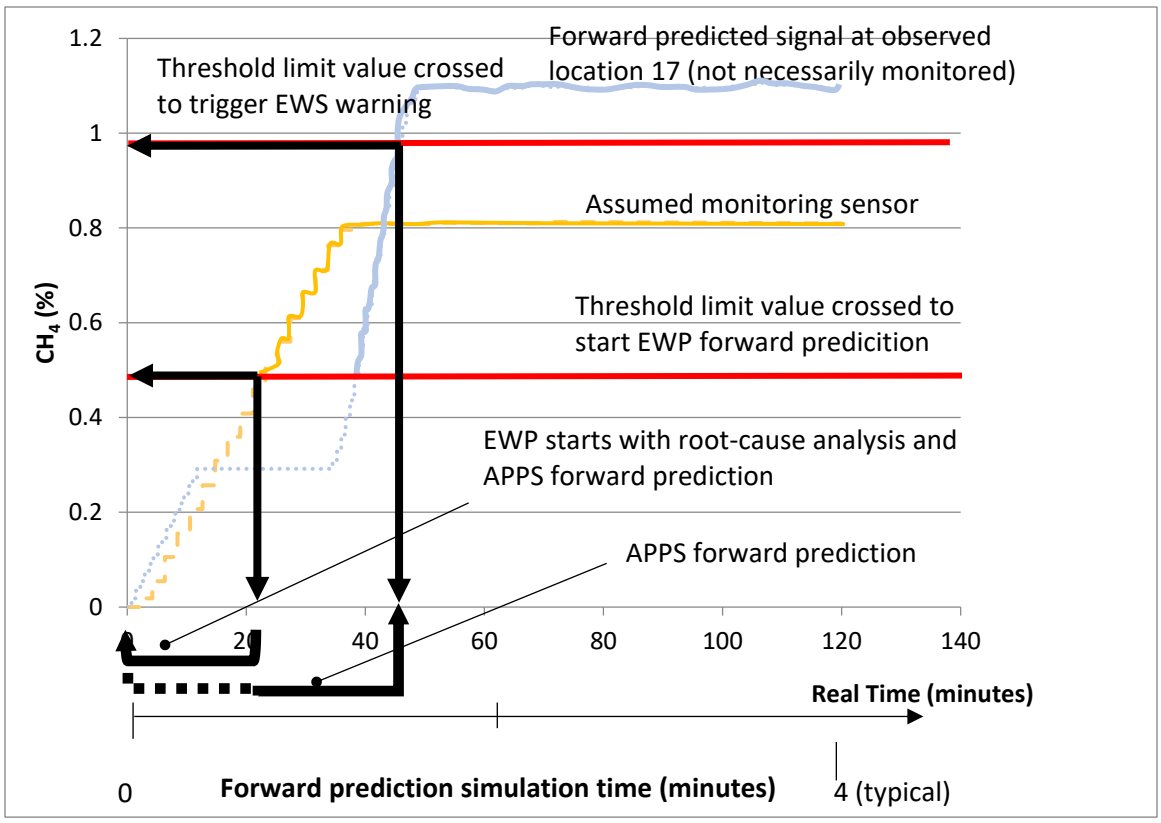


Figure 4-13c. APPS model forward prediction at selected observed locations in real-time and in fast simulation time scales for Scenario 2. Only two selected locations are shown (Danko et al, 2016).

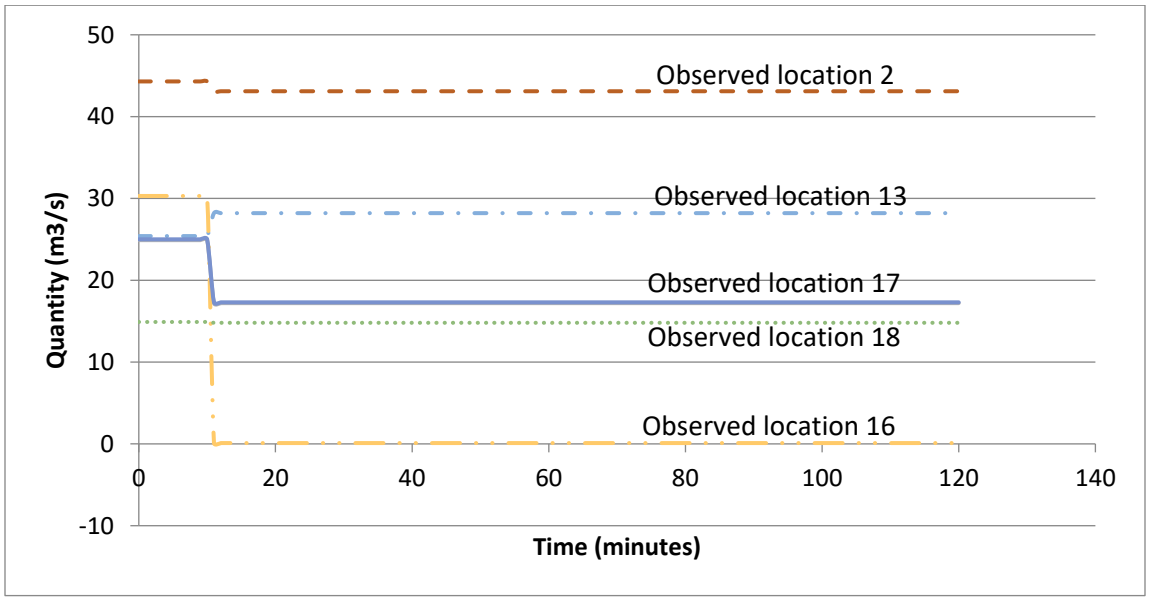


Figure 4-14. Results of airflow at assumed monitored locations due to airway blockage in coal mine example 1 (Danko et al, 2016).

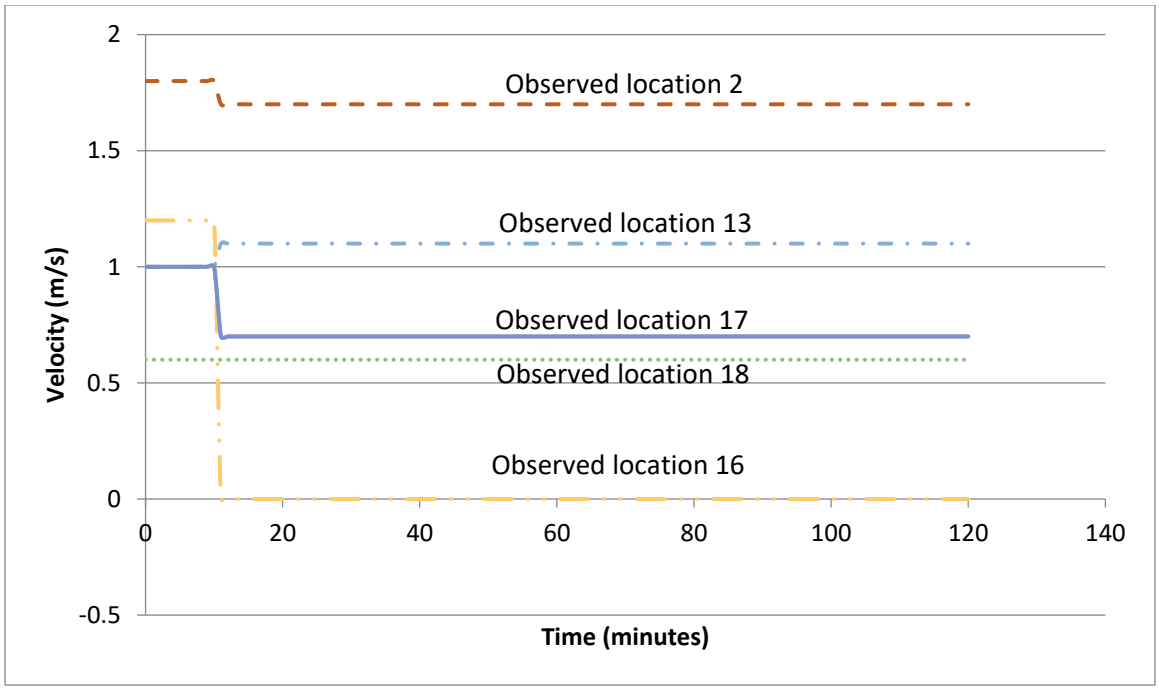


Figure 4-15. Results of velocity at assumed monitored locations due to airway blockage in coal mine example 1 (Danko et al, 2016).

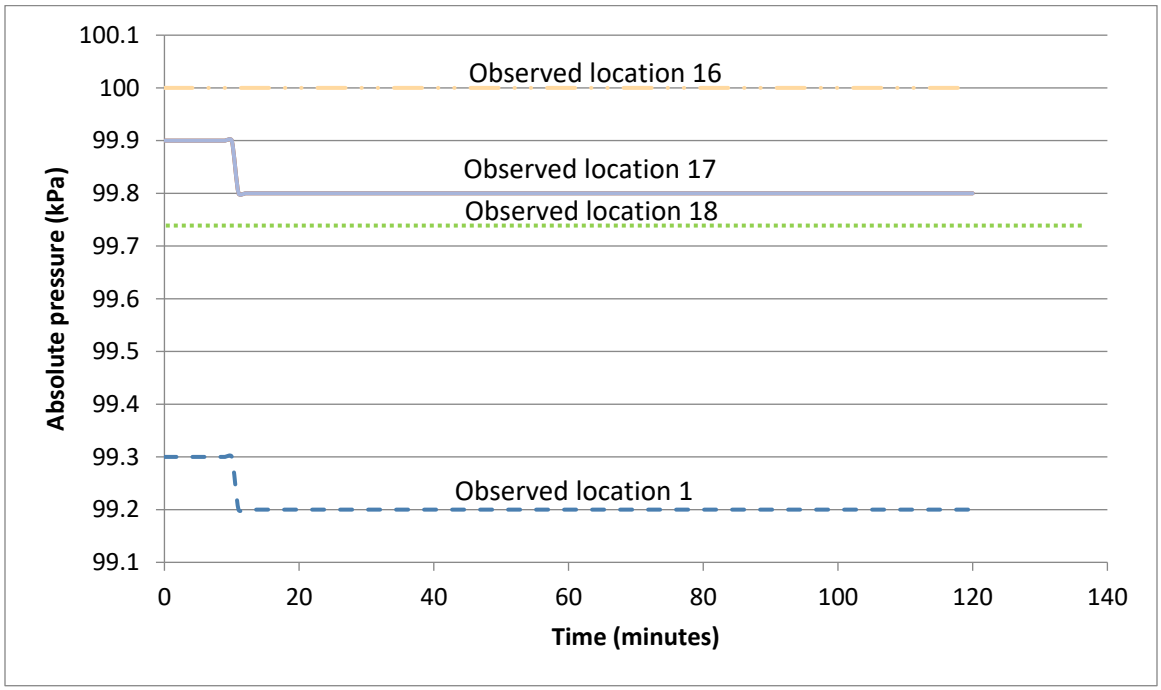


Figure 4-16. Results of absolute pressure at assumed monitored locations due to airway blockage in coal mine example 1 (Danko et al, 2016).

### 4.1.3 Atmospheric barometric pressure variations causing methane inflow from the gob (Scenario 3, mine example 1)

A large volume of porous and fractured methane coal seam under pressure variations, described in Appendix 3, may release a large amount of methane by Darcy flow. Gob, strata, and partially sealed off dead zones are examples of such a volume.

One methane gas source S2 is modeled in mine example 1, illustrated in Figure 4-6. The effect of barometric pressure change upon methane inflow from the gob is modeled assuming a 2000 Pa drop from a previously high value in 20 minutes and keeping it low for an hour. Although no problem may be caused by $CH_4$ release due to slow barometric pressure changes under normal weather conditions, sudden change may induce $CH_4$ from the gob into the airway as demonstrated in Figure 4-17. The data is for 60 minutes, 20 minutes of drop and 40 minutes of no change in pressure. Pressure variation of large amplitude is seen in Figure A3-1 from real weather data, showing pressure drops of the same magnitude in about 10 days intervals, therefore, the sudden-drop scenario may happen during a fast-moving storm or a weather front.

The methane source is modeled using a gob model in MULTIFLUX. The details of the gob model is depicted in Appendix 3. The results from MULTIFLUX shown in Figure 4-17 are entered into Ventsim and modeled to determine its effects on methane concentrations and airflow parameters. The simulation results for selected locations with significant changes only are plotted. The time-dependent VAM results for methane concentration are demonstrated in Figure 4-18a. The emulated sensor signals used as monitored data input to trigger the EWS system is shown in Figure 4-18b. Figure 4-18c depicts the APPS model forward prediction results for observed locations 15 and 17 based on the 0.5% methane

crossing at assumed sensor 15. There are slight changes in airflow and velocity illustrated in Figure 4-19 and 4-20, respectively and significant drop in absolute pressure depicted in Figure 4-21. A threshold limit value of 1% methane for stopping work is used in this analysis. Using branch 742, which is a sensor location just at the end of the active face as a reference and using a safety level of 0.5% methane, the delay time can be estimated. Branch 742 reaches 0.5% in 19 minutes and branch 760 (forward predicted signal at observed location 17 downstream of branch 742 on the return airway, not necessarily monitored), reaches 1% in 42 minutes as illustrated in Figure 4-18c. Therefore, the delay time before branch 760 crosses the threshold is 23 minutes (42 minutes minus19 minutes), which triggers an EWS alarm. Since, there is a threshold crossing, the gain time for management to take action is 21 minutes (23 minutes minus 2 minutes forward prediction time). The type of methane increase is a dynamic delayed signal trend shown in Figure 4-18a, from too complex of a process to be described by a simple model. Therefore, an NTCF predictive model as a dynamic Jacobian gob model detailed in Appendix 3 is used to simulate such a scenario.

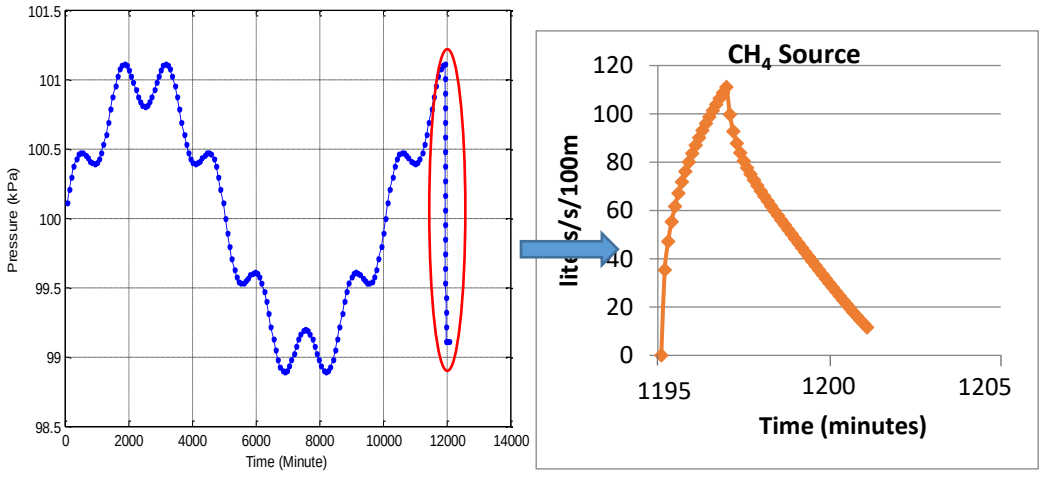


Figure 4-17. Barometric pressure drop inducing $CH_4$ flow (Danko et al, 2016).

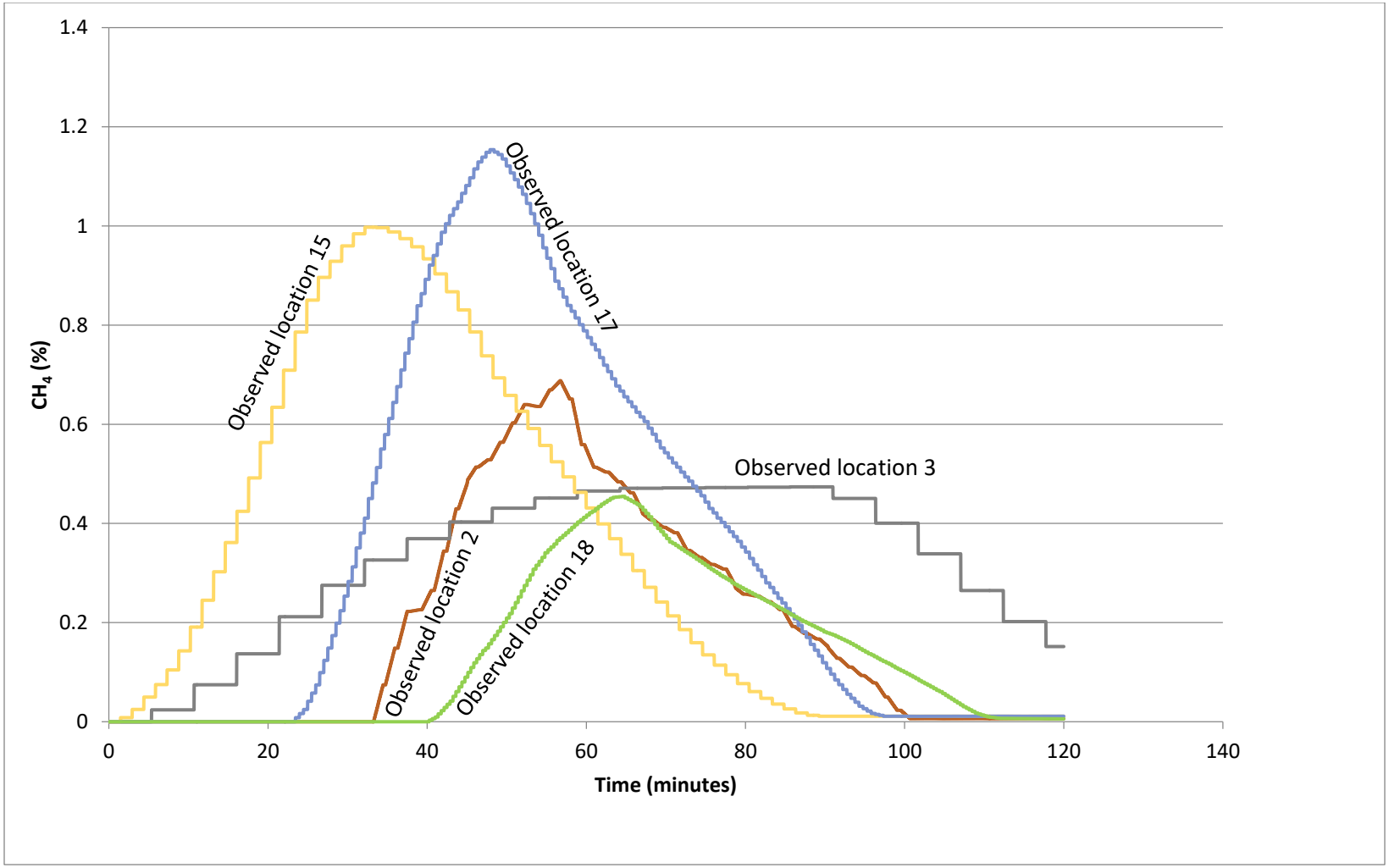


Figure 4-18a. Results of methane concentration at selected observed locations from native VAM simulation in Scenario 3. Selected locations with significant changes only are plotted (Danko et al, 2016).

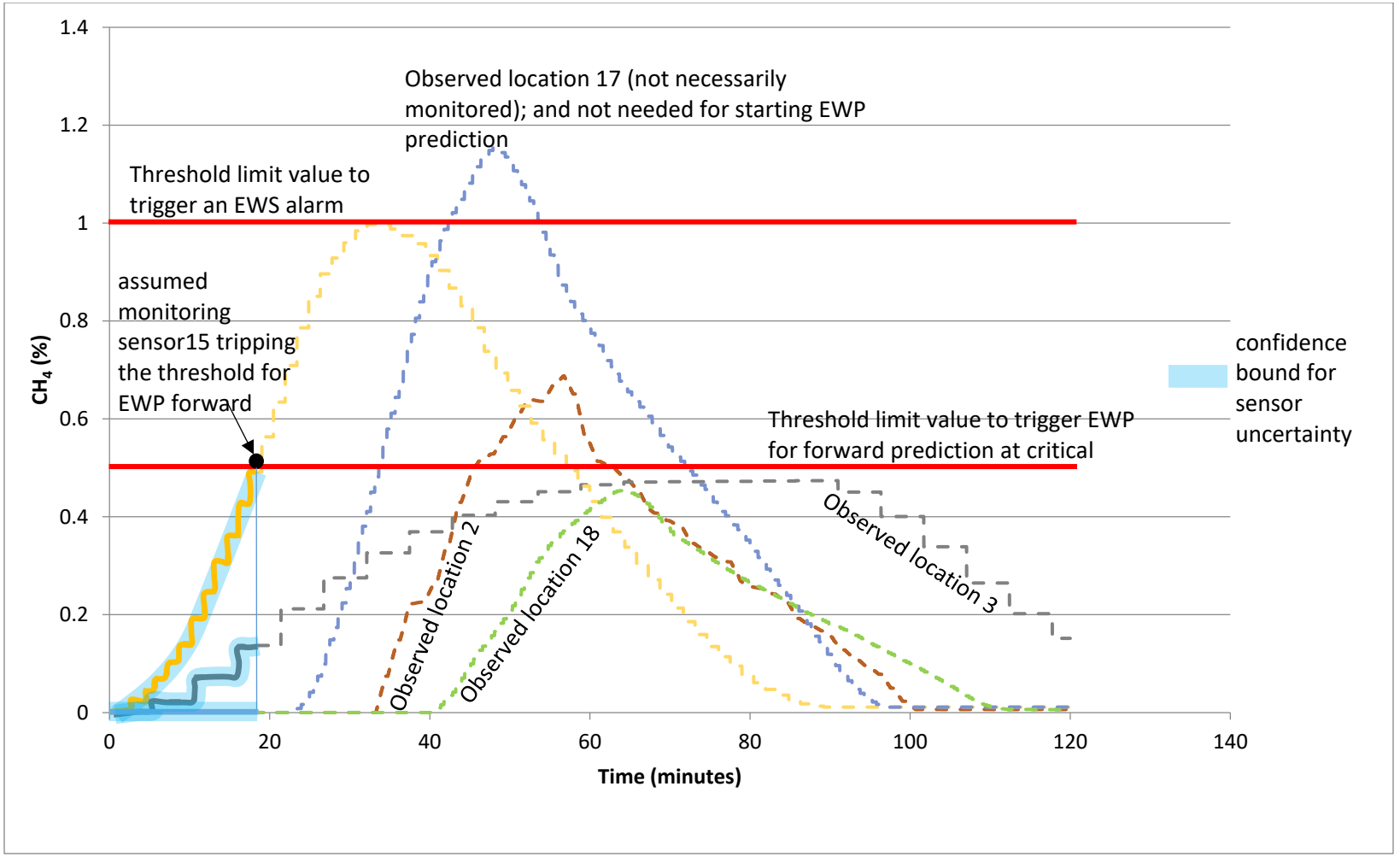


Figure 4-18b. Emulated sensor signal used as assumed monitored data input to trigger the EWS system Scenario 3 (shown in thick lines with confidence bounds). Assumed sensors 15 (and 17 if installed) trip threshold for EWP forward prediction. The curves show real-time changes in $CH_4$ concentration. Selected locations with significant changes only are plotted. Note that the sensor signals are also used for the APPS corrector continuously (shown in dashed lines) (Danko et al, 2016).

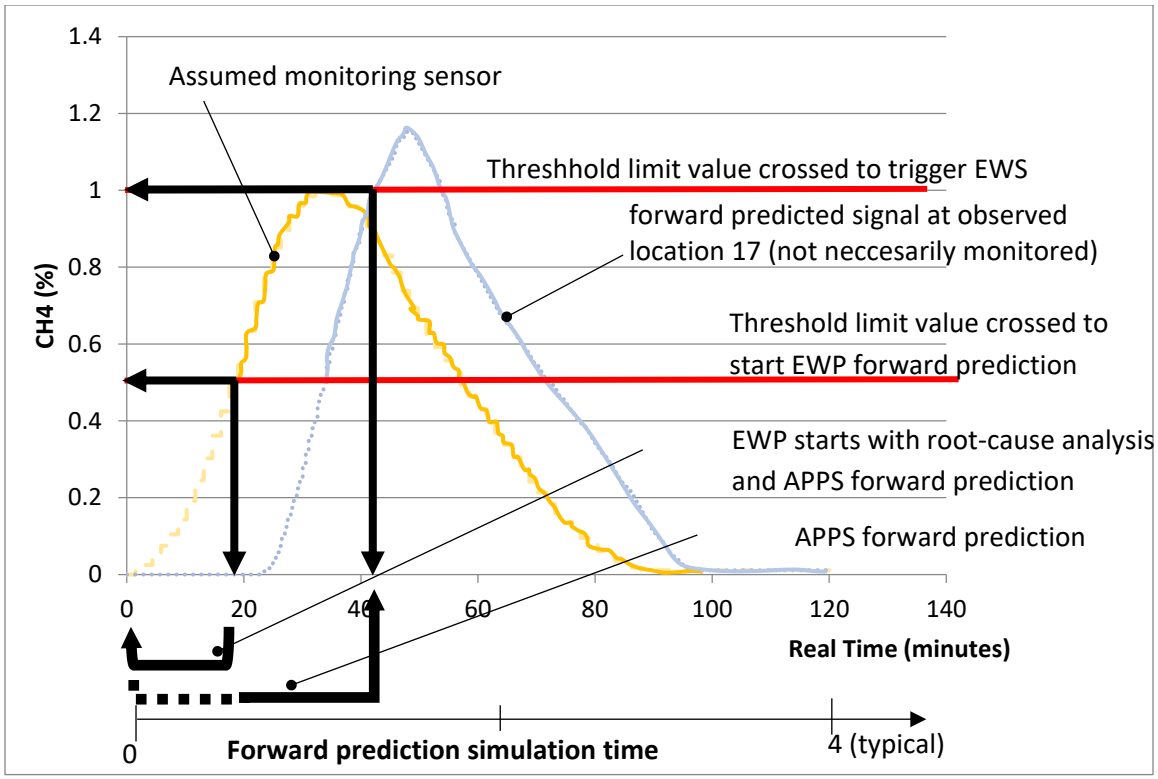


Figure 4-18c. APPS model forward prediction at selected observed locations in real-time and in fast simulation time scales for Scenario 3. Only two selected locations are shown (Danko et al, 2016).

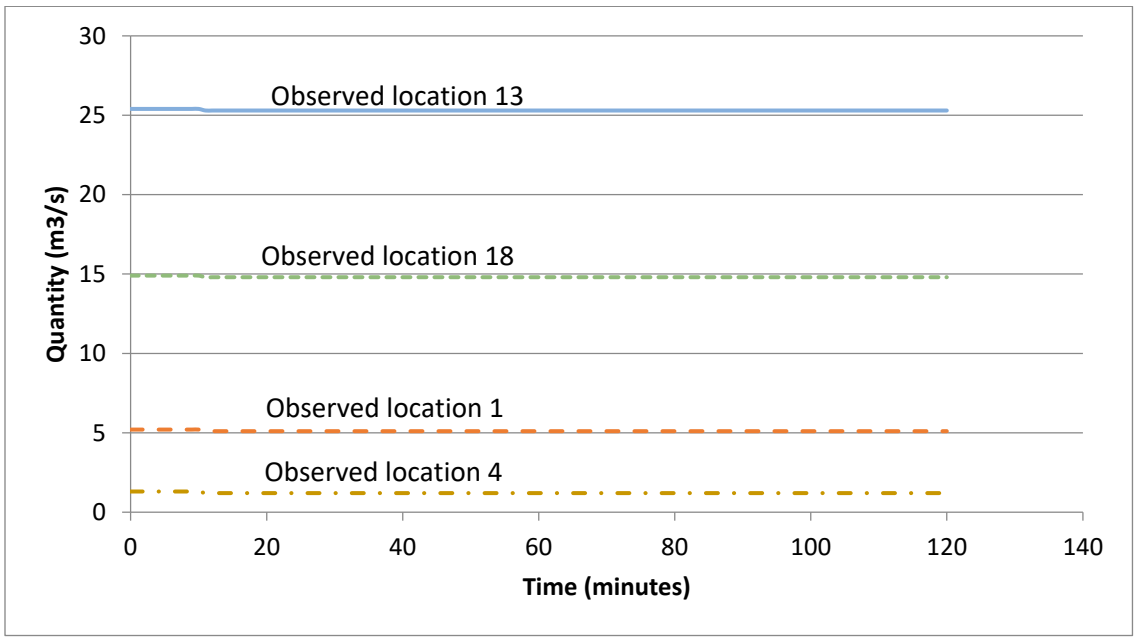


Figure 4-19. Results of airflow at monitored locations due to barometric pressure drop (Danko et al, 2016).

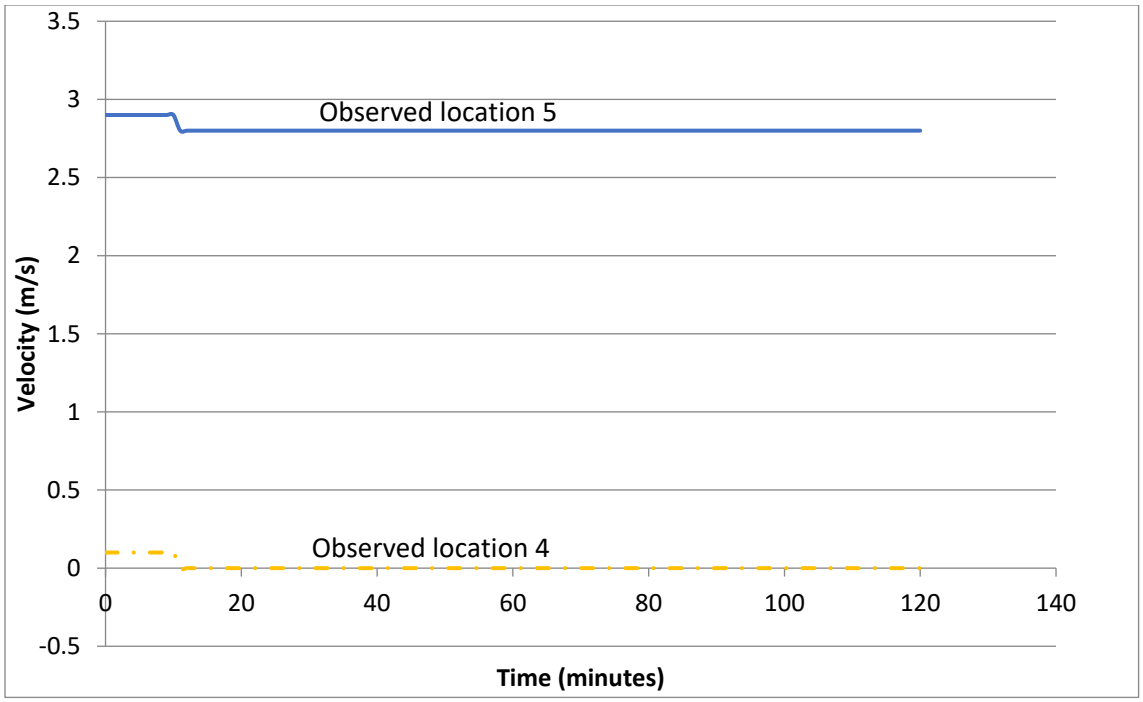


Figure 4-20. Results of velocity at monitored locations due to barometric pressure drop (Danko et al, 2016).

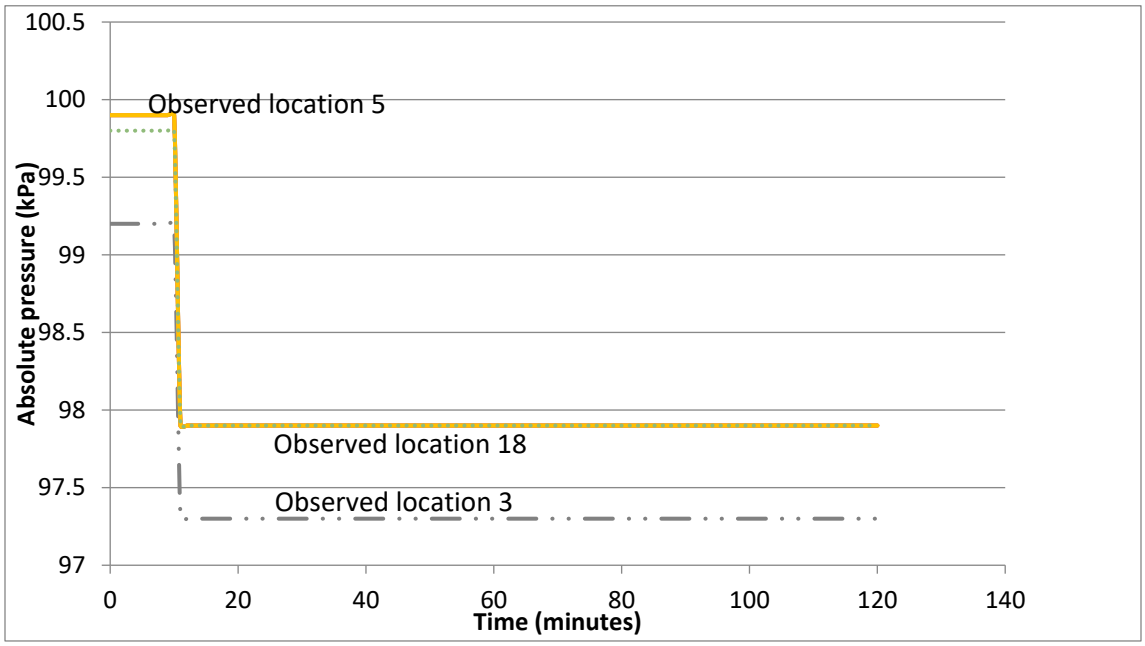


Figure 4-21. Results of absolute pressure at assumed monitored locations due to barometric pressure drop in coal mine example 1 (Danko et al, 2016).

### 4.1.4. Fan malfunctioning (Scenario 4, mine example 2)

Fans are very important equipment in underground mines to provide fresh air to dilute gases in the mine. However, interruptions in fan power supply or fan malfunctioning may result in sudden fan stoppage. Reduction in airflow prevents proper dilution of gases in the working areas. Fan malfunction or the effect of fan stoppage can be indicted by MPD. Fluctuations may be caused by mechanical failure or electrical interruptions. The root cause for this scenario may be detected from the fan power and electrical equipment power usage. Changes of the airflow rate and pressure are other indications. This event is rarely observed regarding surface fans, nonetheless, it may happen frequently to booster fans.

A partial fan malfunction is modelled in mine example 2, Figure 4-10, by reducing one of the fans' static pressure by 30% (fan #4 in branch 230) on the surface connected to the return shaft after 10 minutes into a 2-hour simulation. All three methane sources, S1, S2, and S3 are kept unchanged. Table A4-1 in Appendix 4 demonstrates both the original and reduced fan points. Figure A4-1 illustrates the fan curves for the original (a) and reduced (b) fan points. The areas of perturbation are shown in Figure 4-22 with S1 in the longwall intake airways (branch 249), S2 at the working face (branch 100), and S3 in the longwall return airway (branch 251). The area of investigation for methane in-burst in the two coal mines is working face.

The simulation results for selected locations with significant changes only are plotted. The time-dependent VAM results for methane concentration are demonstrated in Figure 4-23a. The emulated sensor signals used as monitored data input to trigger the EWS system is shown in Figure 4-23b. Figure 4-23c depicts the APPS model forward prediction results for observed locations 13 and 18 based on the 0.5% methane crossing at assumed sensor

13. The airflow, velocity and absolute pressure simulation results are depicted in Figures 4-24, 4-25, and 4-26, respectively. Comparing this scenario to the base scenario 1C for mine example 2, it is seen that the airflow reduced significantly resulting in increased methane concentration and absolute pressure at some locations. Therefore, using branch 219 (monitoring sensor 13), which is a sensor location just at the end of the active face as a reference and using a safety concentration of 0.5% methane, the delay time can be estimated. Branch 219 reaches 0.5% in 9 minutes and branch 251 (forward predicted signal at observed location 18 downstream of branch 219 on the return airway, not necessarily monitored), reaches a maximum of 0.91% in 19 minutes and remains constant as illustrated in Figure 4-23c. Hence, the delay time before branch 219 reaches 0.91% is 10 minutes (19 minutes minus 9 minutes). Therefore, 8 minutes are available for advance notice (10 minutes minus 2 minutes forward prediction time). However, there is no 1% methane threshold crossing at this time.

The results indicate that a delayed mixing process decreased dilution and increased methane concentration. The signature trends for a fan malfunction is a step change as shown in Figure 4-23a through 4-26 which is similar to scenario 2. For forward prediction, a gas accumulation model is required in APPS for this scenario. Fan power comparison for all five scenarios is detailed in Appendix 5.

The fan power of scenario 4 for the fan with reduced rpm (fan ID=230) decreases significantly compared to the Base scenario 1C. Therefore, fan power measurements are conclusive only in the case of the fan malfunction.

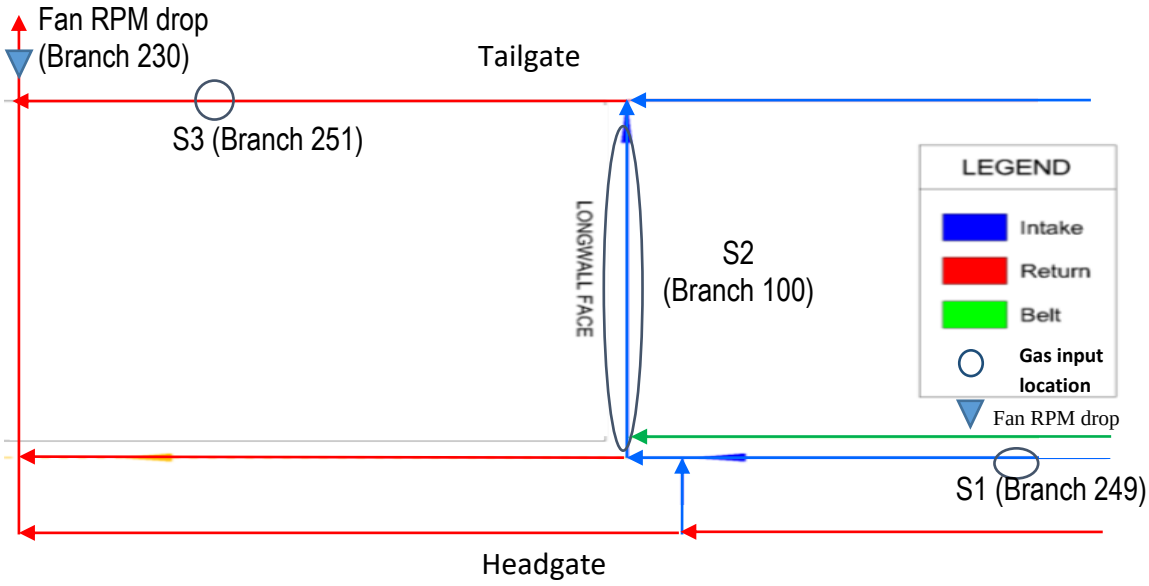


Figure 4-22. Schematic of modeled section showing areas of perturbation with source locations and fan RPM drop location for coal mine example 2 (Danko et al, 2016).

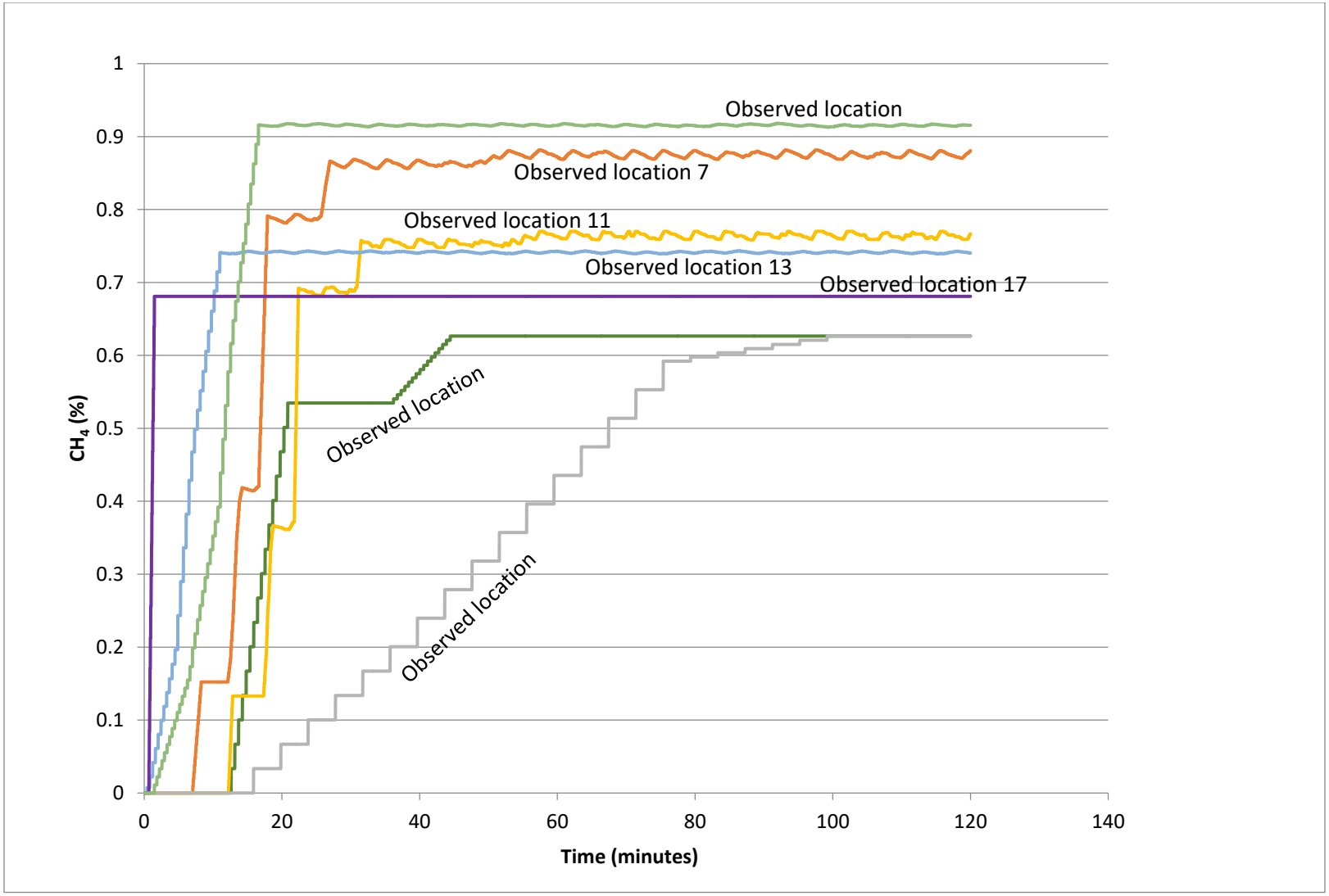


Figure 4-23a. Results of methane concentration at selected observed locations from native VAM simulation in Scenario 4. Selected locations with significant changes only are plotted (Danko et al, 2016).

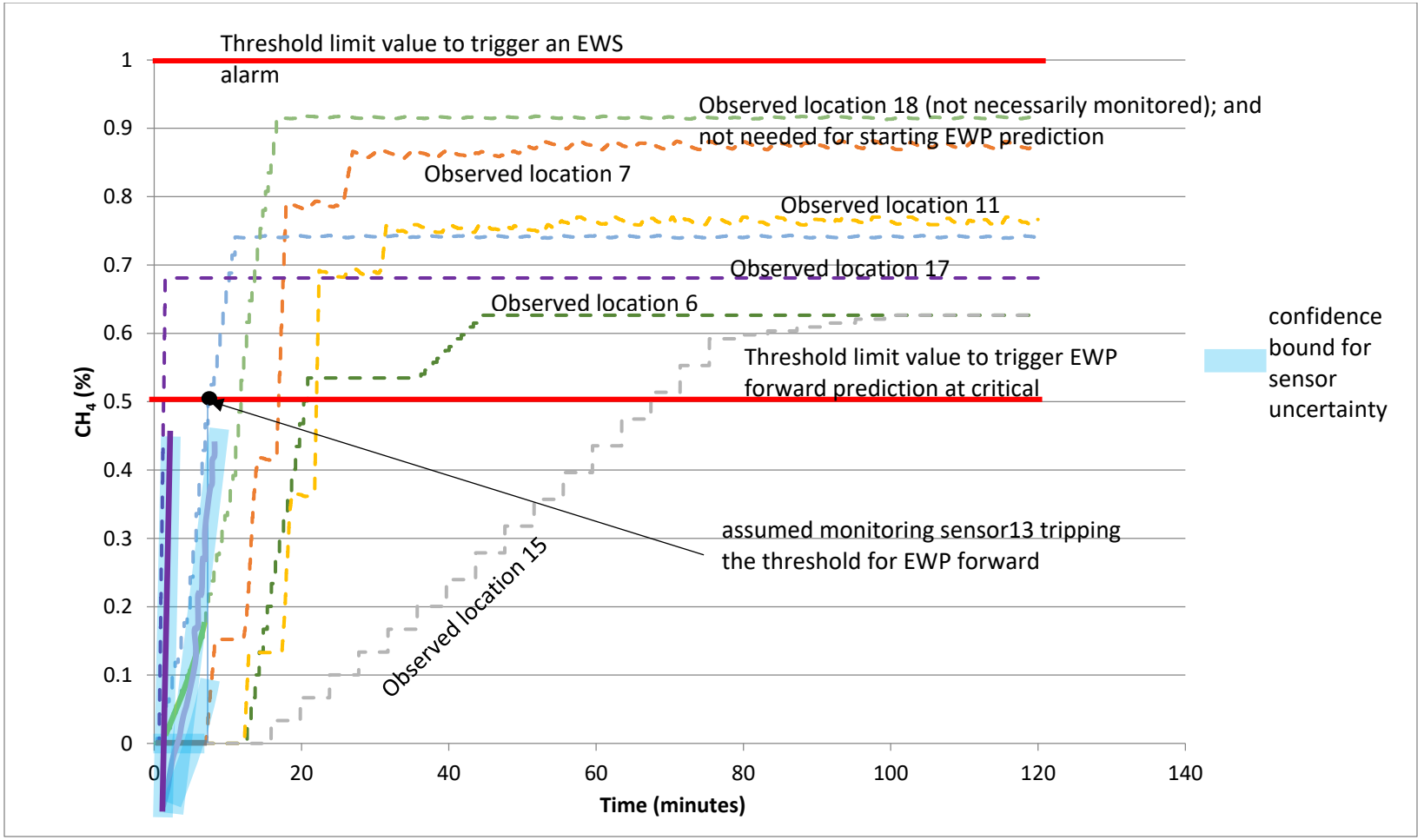


Figure 4-23b. Emulated sensor signal used as assumed monitored data input to trigger the EWS system in Scenario 4 (shown in thick lines with confidence bounds). Assumed sensors 13, 17 (and 18 if installed) trip(s) threshold for EWP forward prediction. The curves show real-time changes in $CH_4$ concentration. Selected locations with significant changes only are plotted. Note that the sensor signals are also used for the APPS predictor continuously (shown in dashed lines) (Danko et al, 2016).

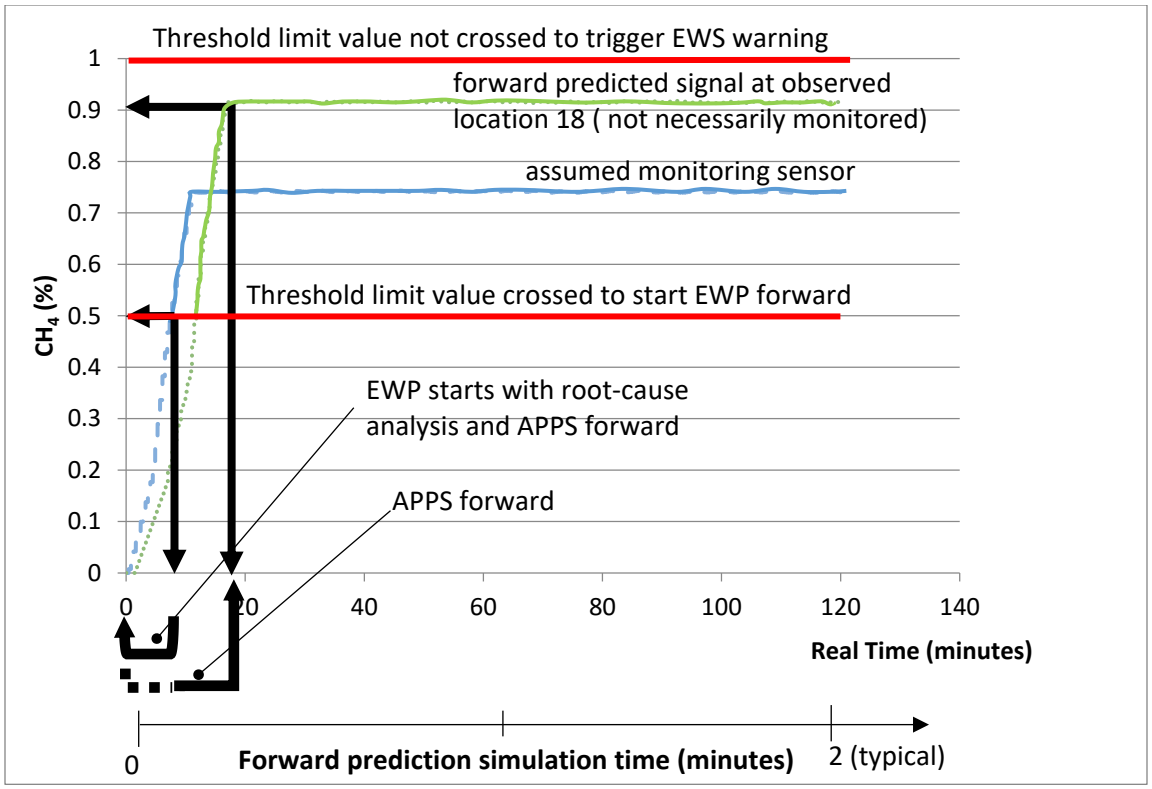


Figure 4-23c. APPS model forward prediction at selected observed locations in real-time and in fast simulation time scales for Scenario 4. Only two selected locations are shown (Danko et al, 2016).

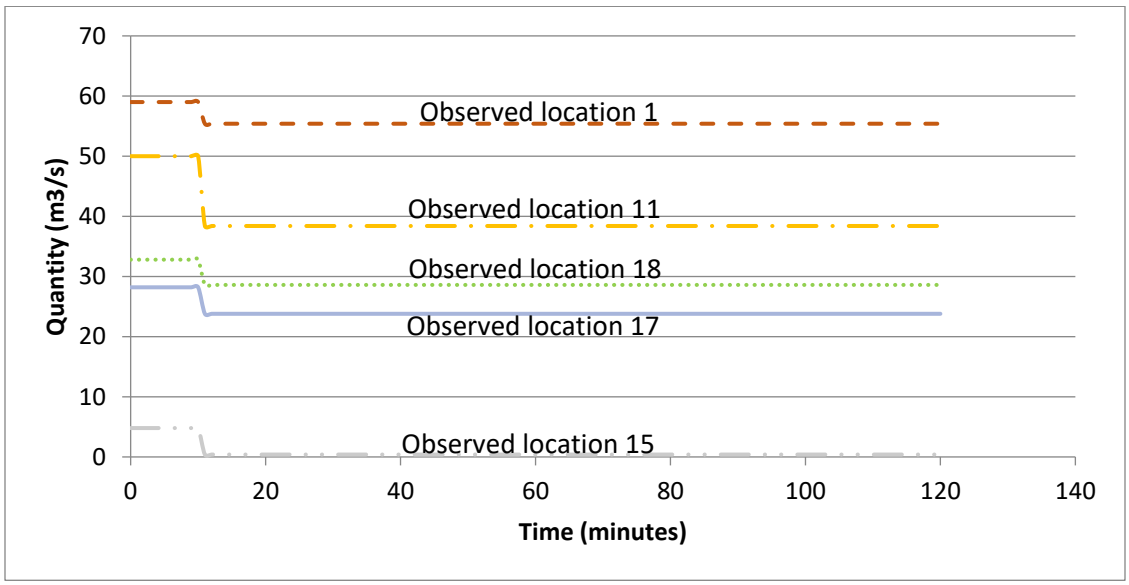


Figure 4-24. Results of airflow at assumed monitored locations due to fan malfunction in coal mine example 2 (Danko et al, 2016).

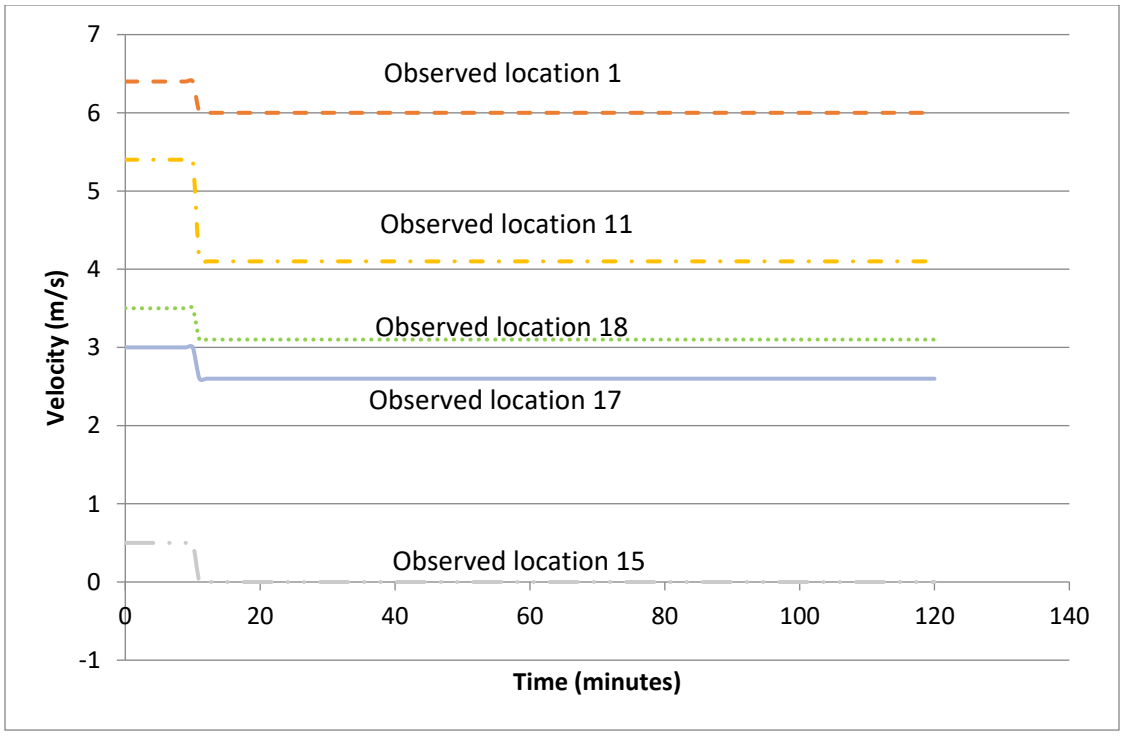


Figure 4-25. Results of velocity at assumed monitored locations due to fan malfunction in coal mine example 2 (Danko et al, 2016).

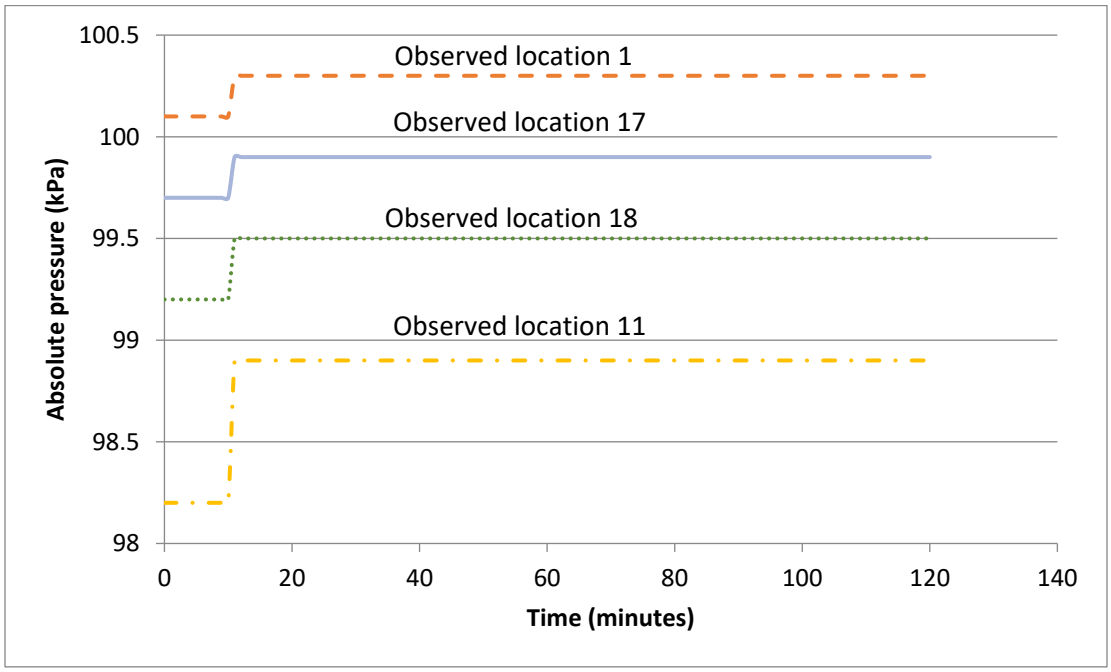


Figure 4-26. Results of absolute pressure at assumed monitored locations due to fan malfunction in coal mine example 2 (Danko et al, 2016).

### 4.1.5 Fire heat load (Scenario 5, mine example 2)

Fire of coal dust, belt, truck, fuel and lube bays are serious hazard scenarios. Truck fires may be due to an overload. Overheating of the longwall cutter heads as a result of overload might lead to fire which could ignite the coal dust. Although, this event is not frequent, it is highly dangerous once it occurs in a mine.

Fire load is modeled using conveyor belt fire with S1, S2 and S3 in mine example 2 illustrated in Figure 4-10. A conveyor belt fire with an assumed burning rate of 1000 kg/hr to 3000 kg/hr is modeled in branch 96 approximately 350 ft away from the longwall face in order to examine its effect on gas concentrations and airflow parameters. The fire is set up to start from 600 seconds through 3600 seconds during the simulation period of 2 hours. The areas of perturbation are shown in Figure 4-27 with S1 in one of the longwall intake airways (branch 249), S2 at the working face (branch 100), and S3 in the longwall return airway (branch 251).

The area of investigation is methane concentration variation due to changes carried by the fire at the working face. The simulation results for selected locations with significant changes only are plotted. The time-dependent VAM results for methane concentration are demonstrated in Figure 4-28a. The emulated sensor signals used as monitored data input to trigger the EWS system is shown in Figure 4-28b. Figure 4-28c depicts the APPS model forward prediction results for observed locations 13 and 18 based on the 0.5% methane crossing at assumed sensor 13. However, there are slight variations in the airflow and velocity results illustrated in Figures 4-29 and 4-30, respectively. The absolute pressure does not change. No significant methane concentration change is seen from the face due to fire at a different location. However, immediate action must be taken as soon as a signal

indicates there is fire in the mine and it is confirmed. There is no need for further forward prediction for the other gas concentrations since the mine is placed in an alarm state in a real mine fire.

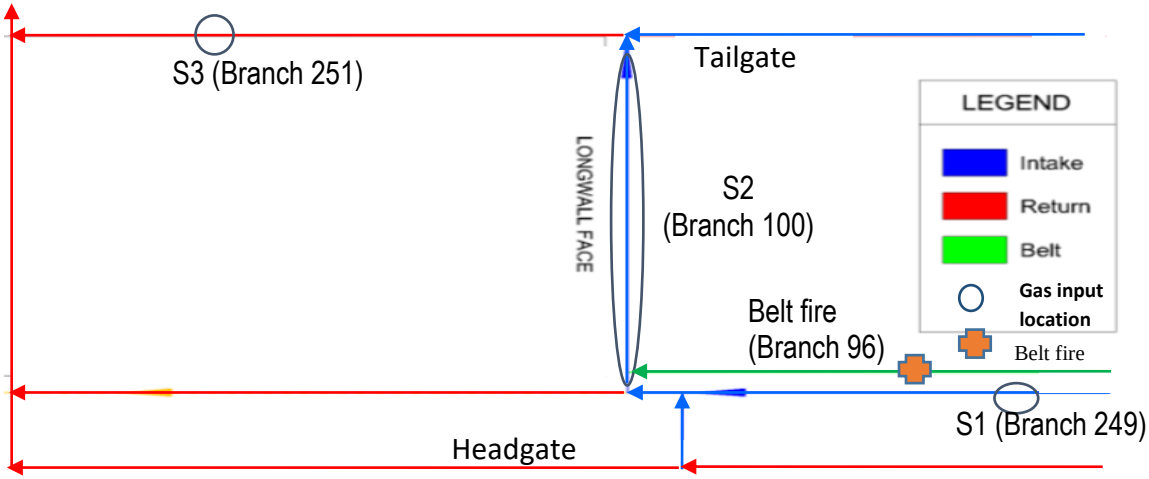


Figure 4-27. Schematic of modeled section illustrating areas of perturbation with source locations and belt fire location for coal mine example 2 (Danko et al, 2016).

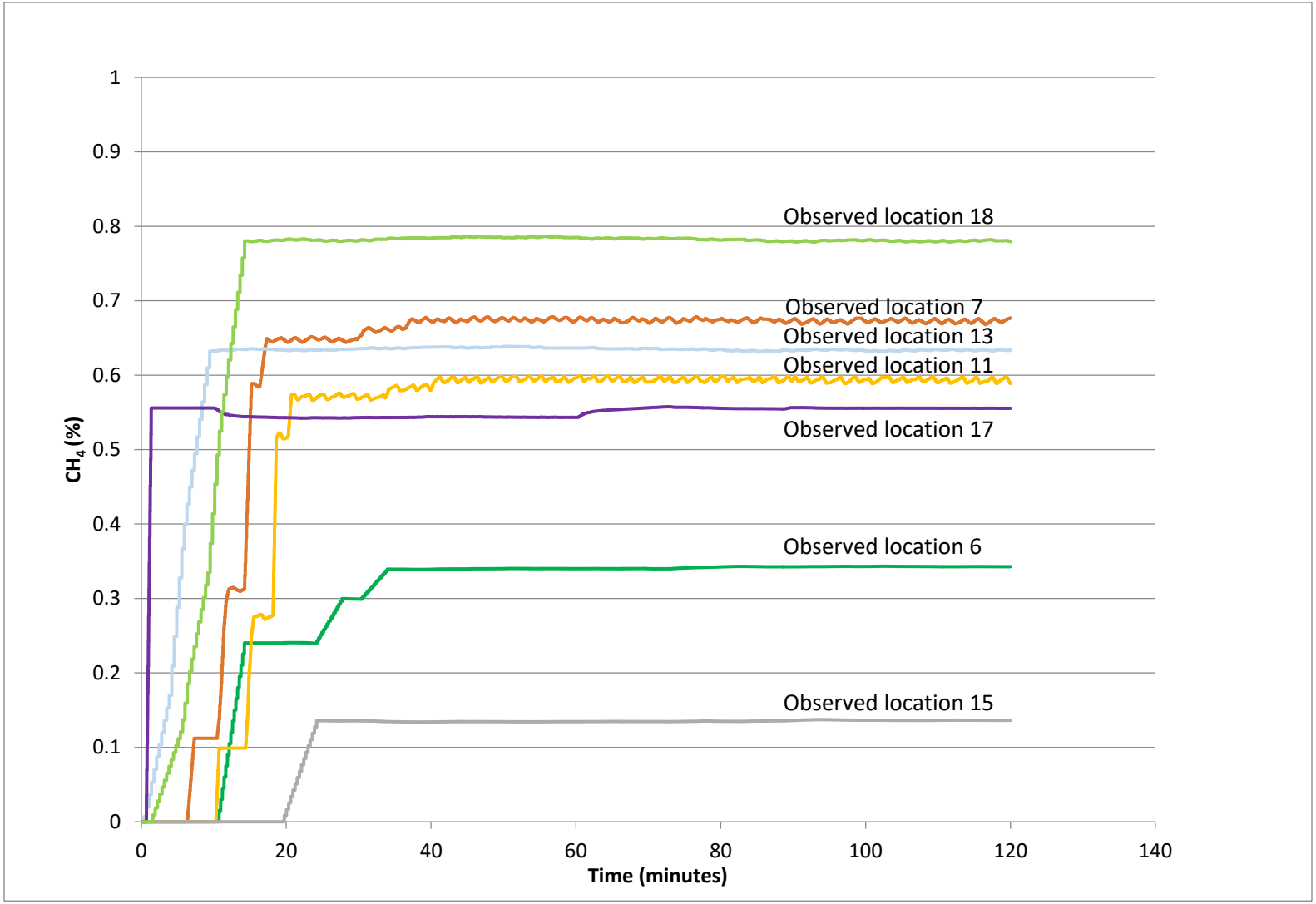


Figure 4-28a. Results of methane concentration at selected observed locations from native VAM simulation in Scenario 5. Selected locations with significant changes only are plotted (Danko et al, 2016).

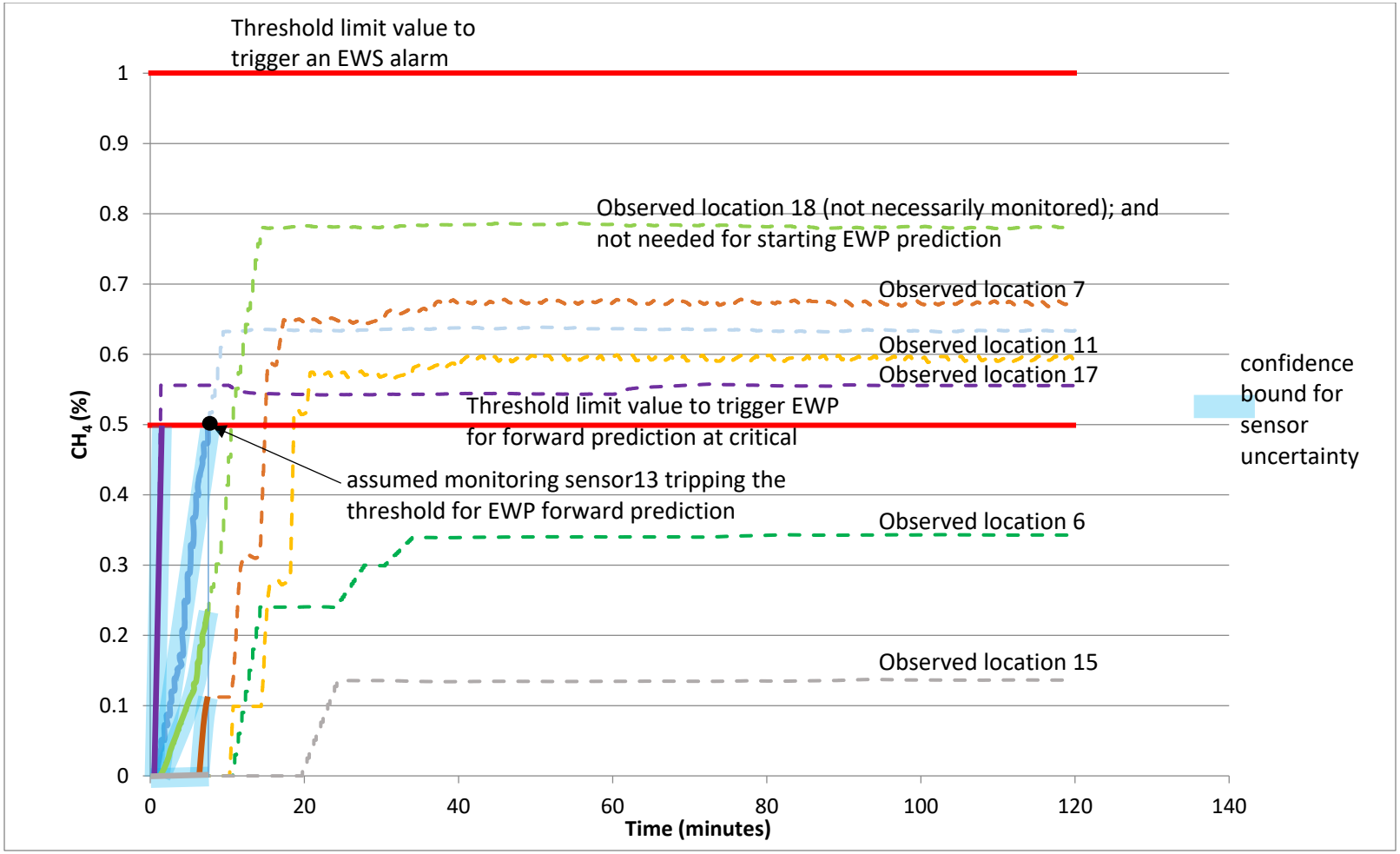


Figure 4-28b. Emulated sensor signal used as assumed monitored data input to trigger the EWS system in Scenario 5 (shown in thick lines with confidence bounds). Assumed sensors 13, 17 (and 18 if installed) trip(s) threshold for EWP forward prediction. The curves show real-time changes in $CH_4$ concentration. Selected locations with significant changes only are plotted. Note that the sensor signals are also used for the APPS predictor continuously (shown in dashed lines) (Danko et al, 2016).

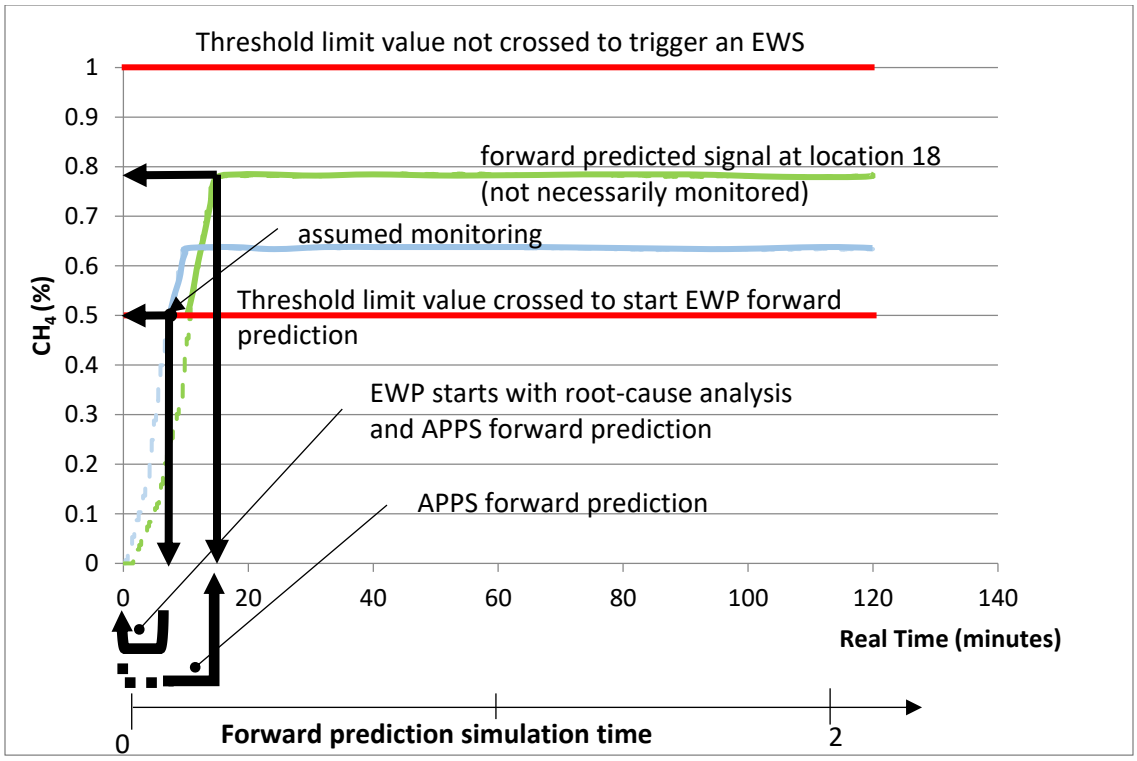


Figure 4-28c. APPS model forward prediction at selected observed locations in real-time and in fast simulation time scales for Scenario 5. Only two selected locations are shown (Danko et al, 2016).

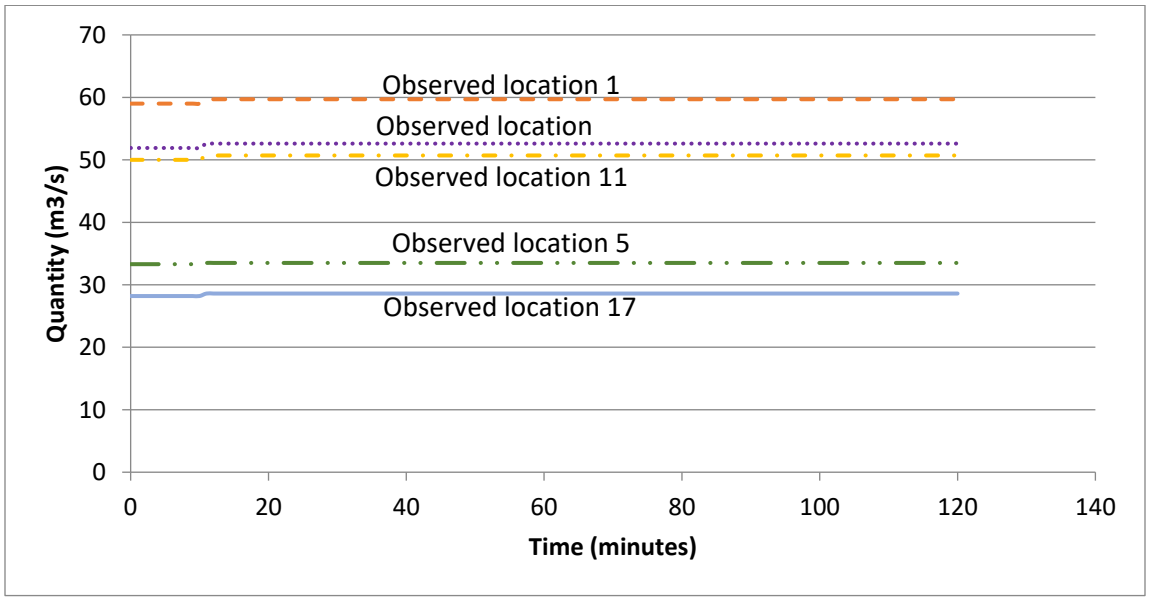


Figure 4-29. Results of airflow at assumed monitored locations due to belt fire in coal mine example 2 (Danko et al, 2016).

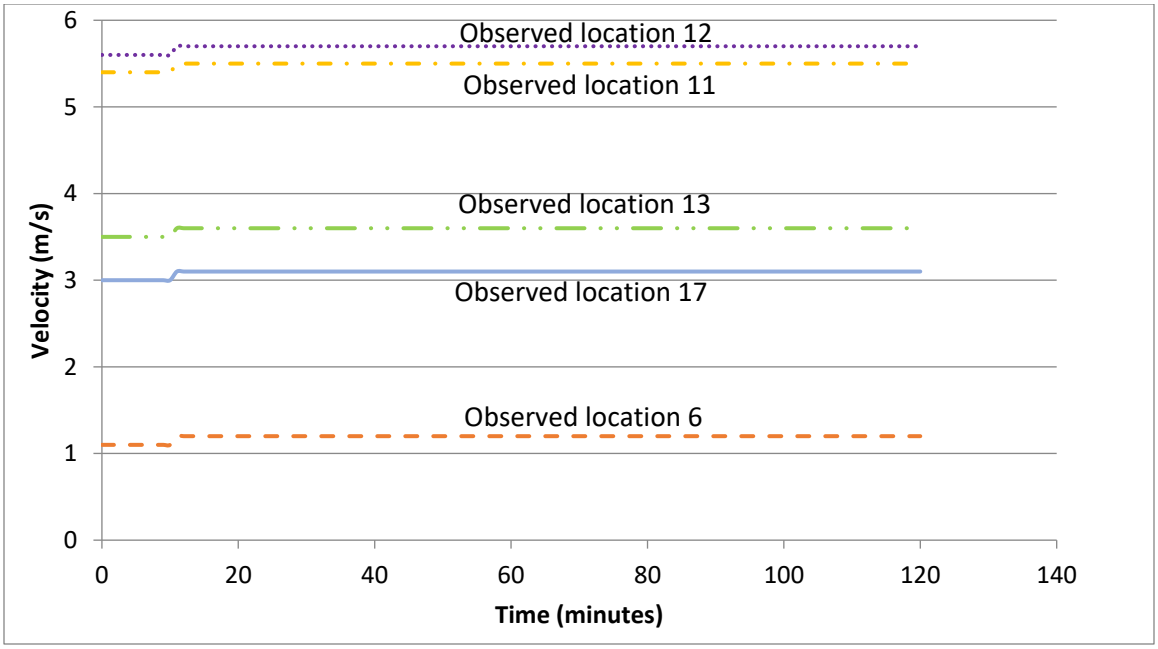


Figure 4-30. Results of velocity at assumed monitored locations due to belt fire in coal mine example 2 (Danko et al, 2016).

The summarized results for maximum concentration from the forward prediction as well as the delay time in methane front arrival for all the scenarios based on the sensors used in the analysis (ie 15 and 17 for mine example 1; and 13 and 18 for mine example 2) are summarized in Table 4-2.

Table 4-2. Summarized results for maximum concentration from the forward prediction as well as the delay time in methane front arrival for all scenarios (Danko et al, 2016).

| Scenario | T1 (mins) | T2 (mins) | Max. $CH_4$ (%) | T3 (mins) | T4= T3-T1 (mins) | T5= T4-T2 (mins) |
|---|---|---|---|---|---|---|
| 1A | 21 | 2 | 0.80 | 33* | 12* | 10* |
| 1B | 21 | 2 | 1.12 | 52 | 31 | 29 |
| 1C | 7 | 2 | 0.80 | 17* | 10* | 8* |
| 2 | 23 | 2 | 1.10 | 46 | 23 | 21 |
| 3 | 19 | 2 | 1.18 | 42 | 23 | 21 |
| 4 | 9 | 2 | 0.91 | 19* | 10* | 8* |
| 5° | 8 | 2 | 0.78 | 17° | 9° | 7° |

* No alarm is triggered since methane concentration is less than 1% and therefore, immediate action is not needed.

° No alarm is triggered in terms of methane concentration increase, however, action must be taken as soon as a signal indicates there is fire in the mine and is confirmed.

T1= Threshold value (0.5%) crossing (Hazard Detection time) to trigger EWP forward Prediction

T2= Forward prediction simulation time

Max. $CH_4$ = Maximum CH4 concentration from forward prediction

T3= Safety Threshold value (1%) crossing time to trigger EWS alarm

T4= Delay time required for CH4 concentration to cross the threshold limit value of 1%

T5= Actual gain time for management to take action

The comparison of fan power for scenarios 1A, 1B, 2, and 3 modeled in example 2 is shown in Appendix A5-1. Also, the comparison of fan power for scenarios 1B, 4, and 5 modeled in example 2 is demonstrated in Appendix A5-2. The comparison results indicate that fan power measurements are conclusive only in the case of the fan malfunction.

### 4.3 Time-dependent diesel particulate matter (DPM) contaminant concentration transport simulation

As part of the dynamic atmospheric signal analysis, time-dependent DPM concentration transport (Asante, 2014) is studied for safety checking. The transport of contaminant species by the moving air is of great importance in underground mine environment.

A new method for modeling transport processes has been introduced that combines the Eulerian, fixed control volume with a moving, Lagrangean flow channel for a solution scheme for advection-diffusion problems (Danko, 2016).

The multi-level, implicit state-flux, space-time (SFST) model scheme is used for simulating DPM concentration for safety hazard checking in a long drift with constant air flow velocity in a mine environment.

The SFST model is used for the prediction and evaluation of the average exposure to DPM concentration. I have shown that it is helpful for checking the safety hazard beforehand, because once the predicted concentrations suggest there could be elevated concentrations in critical locations leading to an over-exposure of mine workers, measures can be put in place to rectify the problem before sending miners into such working areas.

The model is used to study diesel emission variation in a ventilated underground working area with a moving loader machine. I have proved the validity of the SFST model by comparing numerical simulation results with measurement data collected with stationary as well as moving sensors. The results are discussed and conclusions are drawn from the exercise.

### 4.3.1 DPM sampling experiment in an underground mine

In order to determine the DPM concentration in an underground mine, the air has to be sampled and taken to the laboratory for the determination of the average concentration over the sampled time period. The recommended method for DPM sampling is the NIOSH 5040 method which was used for this experiment. The NIOSH 5040 method uses a sampling sensor which consists of a pump, a cyclone with a tygon tube and a cassette. The DPM is sampled by starting the pump which draws the air through a cyclone into the cassette with a standard flow rate set at 1.7 liters/minute. The cassette is then sealed and taken to the laboratory and results are received within two weeks. The recommended sampling time for the NIOSH 5040 method is 8 hours to ensure sufficient sampling time for more reliable results. However, due to the unavailability of the machine for 8 hours in the same experimental area, the sampling time was 2 hours which was adequate to obtain the minimum flow volume of 142 liters (NIOSH 5040 manual, 2003) required for the laboratory analysis to be performed on the samples. Appendix 6 shows the sample volumes for each cassette.

### 4.3.2 Mine DPM test

DPM contaminant concentration distribution in the ventilating air in a mine drift is modeled based on an underground experiment (Asante, 2014). The mine drift has dimensions of length, L=319 m, width, W=4 m, and height, H=5.6 m. Figure 4-31 shows the experimental haulage route for the diesel machine. Two sampling methods were performed: area sampling and machine tailpipe source sampling methods.

Three different locations 3.1 m, 48 m, and 78 m away from the loading point were sampled with each location having two DPM sampling sensors placed on the drift wall for the area sampling method.

Also, a Load-Haul-Dump (LHD) machine had two sampling sensors placed 2.1 m away from the tailpipe to sample the exhaust fumes as a source term which was used as input source to the DPM transport model. The sampling sensor were placed 2.1 m away from the direct tailpipe due to the high exhaust fumes temperature that could damage the sampling sensor.

The experimental drift was separated into two segments relative to the direction of air flow as it enters into the mine drift. A 78 m long segment with the airflow direction moving towards the loading point known as the left side (LS) and a 241 m long segment with the airflow direction moving towards the dumping point known as the right side (RS).

The machine traveled with the two sampling sensors placed on it. The tailpipe fumes was then sampled during the machine movement from the loading point to the dumping point for the 2 hour experimental period. The spread of tailpipe exhaust fumes relative to the airflow directions as well as machine movement in and out of both the LS and RS segments as depicted in Figure 4-32.

A 420 second per cycle was obtained resulting in a total of 17 cycles at the end of the test. The DPM sampled cassettes were taken to the laboratory at the end of the test and results received after two weeks. Table 4-3 shows the DPM concentration results for sampled location. The average DPM concentrations between the two samplers at each location is compared with model results.

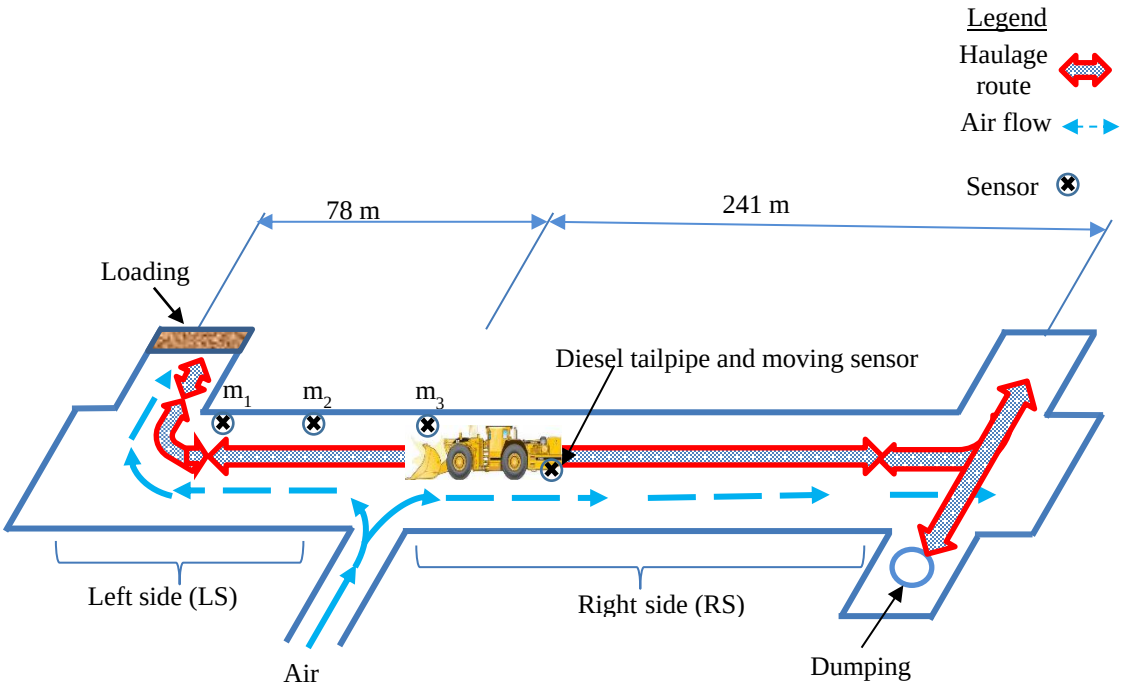


Figure 4-31. Plan view of mine drift (Asante, 2014)

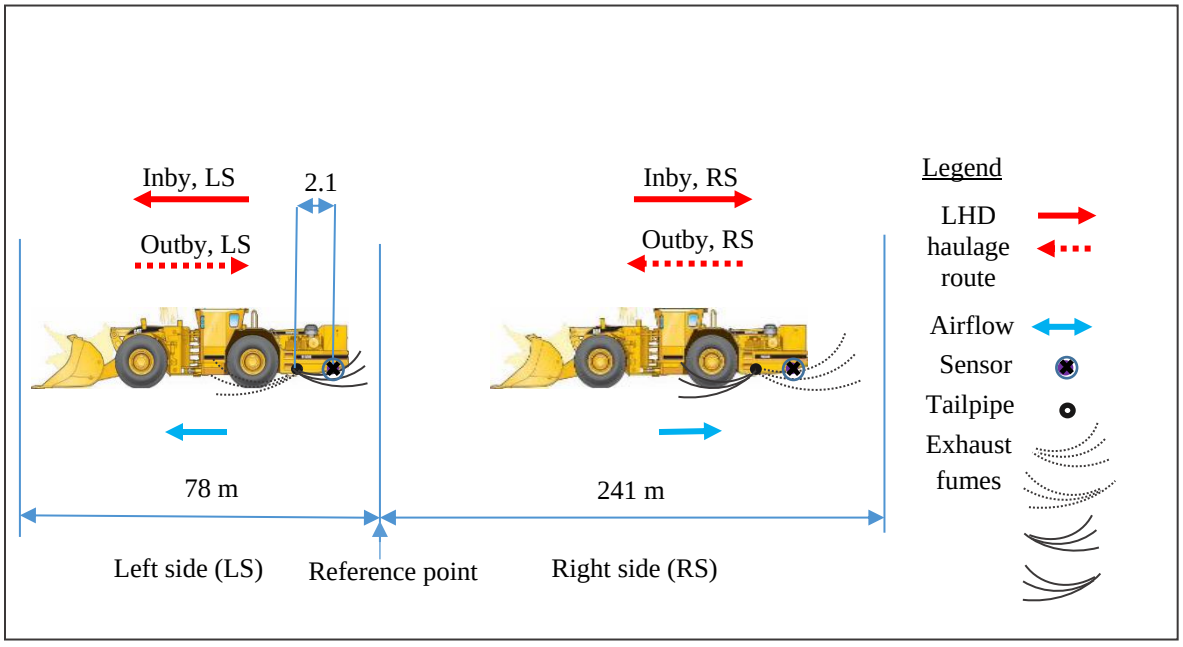


Figure 4-32. Airflow directions and spread of tailpipe exhaust fumes as a result of the LHD machine movement (Asante, 2014)

Table 4-3. DPM measurement results (Asante, 2014)

| Location | DPM Concentration ($\mu g/m^3$) | Average ($\mu g/m^3$) |
|---|---|---|
| Tailpipe sensor #1 | 380 | |
| Tailpipe sensor #2 | 280 | 330 |
| Point 1 sensor # 1 | 120 | |
| Point 1 sensor #2 | 160 | 140 |
| Point 2 sensor #1 | 91 | |
| Point 2 sensor #2 | 85 | 88 |
| Point 3 sensor #1 | 110 | |
| Point 3 sensor #2 | 97 | 103.5 |
| Background (Drift entry point) | | 90 |

### 4.3.3 Variance in DPM sampled results

#### 4.3.3.1. Stationary sensors mounted on the drift wall

There are some differences between the DPM concentration results of the samples received from the DATACHEM analytical laboratory (Appendix 6) for the samples collected close to each other at the approximately same location at the drift wall. The variances between the two individual sampled results for each location relative to the averaged values are about +/- 15%, +/- 3% and +/-6% for points 1, 2 and 3, respectively. These are very acceptable absolute variances for the stationary samplers on the wall, considering that the air flow and concentration profiles are known to be disturbed by turbulent eddies due to the roughness of the wall of a drill-and-blast drift (McPherson, 1993). The concentration profiles around the sampler units may have easily been different to the extent of the measurement observations due to the local air velocity and DPM concentration variations. Even numerical simulation results from the time-and-space model show ruggedness of the concentration variations depending on the average dispersion coefficient assumed in the

simulation, shown in Figures 4-36, 4-39 and 4-42 for the stationary sampling DPM sensors. The ruggedness of the DPM results from the simulation model caused by the finite pixel size and the mismatch of the air and the machine velocities truncating periodically and differently the fixed mixing volume in each pixel will be discussed and explained in more detail later in this chapter. Enough to say for now that the DPM transport by advection and dispersion as well as the resulting concentration distribution may result in a rugged variation with time (and space) due to the time-variable eddies of air. Considering that the ruggedness of the simulated concentration profiles may reach close to +/-10% to +/-40% for a low dispersion coefficient of 0.05 $m^2/s$ depending on the position of the DPM source (seen in Figure 4-36) and the ruggedness all but disappears for a high dispersion coefficient of 2.5 $m^2/s$ (seen in Figure 4-42), the measured variations are considered very minor wit, the local dispersion coefficients around the DPM samplers may be very different (e.g., 0.05 $m^2/s$ for one sensor and 2.5 $m^2/s$ for the other next to it) due to the stochastic nature of the turbulent eddies over the corrugated, rough drift wall. These eddies, in turn, may affect the average values of the sampled DPM concentrations taken at different sensors well over the range of the measured variations as well.

#### 4.3.3.2. Moving sensors mounted on the LHD machine

The variance between the two individual sampled results by the moving sensors relative to the averaged value is about +/-18%. This discrepancy is not surprising as higher variation is expected for the two moving samplers mounted on the machine than for the stationary sensors fastened on the drift wall. This is due to the movement of the samplers as the machine travels back and forth throughout the haulage route with each sampling pump

taking the tailpipe fumes differently. In such a complex underground environment it impossible to sample the same amount of DPM at nearly the same location. This is due to the turbulent nature of the air flow in the drift causing uneven mixing of the air and tailpipe fumes as well as machine movement. Once again, the simulated DPM concentration variations may be studied for an insight of the potential cause of the phenomenon. The simulated tailpipe as well as the sampling sensor concentrations are highly variable for the inby section of the LH drift section at the low dispersion coefficient value of 0.05 $m^2/s$. The relative value of the sensor variance becomes very high in the LH drift section as shown in Figure 4-33, giving approximately +/-20% relative variance to the averaged concentration during the inby travel of the sensor in the air velocity direction (albeit at different rate); and +/-50% relative variance during the outby travel of the sensor opposite to the air velocity direction. The cause of the variation in the simulation is again the periodically varying mixing air volume (and length) due to two different velocities (that of the air and the traveling DPM source) involved in coupled the advection-dispersion transport model. Such a congruency mismatch is unavoidable in reality due to the mixing turbulent eddies in the ventilating air in the drift. Similar DPM variations of significant magnitude are seen at different sections and time periods for other assumed dispersion coefficient cases shown in Figures 4-36, 4-37, 4-40, and 4-41. Conclusively, a +/-18% variance from the measurement by two similar sensors close to each other is well within reason for acceptance.

#### 4.3.3.3. Sensor measurement variances in general

The general difference between repeated reading of like stationary and moving samplers can be attributed to a number of other factors including sampling sensor pump efficiency, turbulent air flow in the measurement drift, laboratory analysis error, and sampling location specifics in the drift. The pumps were pre-calibrated and post-calibrated before and after the sampling and the pump flow rate recorded each time. The sampled air volume which is critical for the DPM laboratory analysis is calculated based on the average flow rate between both calibrations and the sampling time for each pump (Asante, 2014). The two pumps installed at one location may have different efficiencies which could have affected the total volume sampled, affecting the collected DPM amount and the calculated concentration. As discussed before, the angulated walls affected the air flow movement. Therefore, the results of such an experiment under such conditions can be significantly affected.

Nonetheless, the most accurate way to have minimum sampling error would be to measure multiple samples at each location, but due to cost constraints for the project, only two samples were taken at each location. Also, the two weeks' time frame within which the samples are shipped to the laboratory for analysis may contribute to the difference in DPM concentration results.

Again, the center of the drift would be the best location to install the samplers for a more accurate sampling but it would be damaged due to its being in the way of the machine during its movement. As such, a secured location on the wall was selected in order to avoid damage to the samplers. Needless to say, the DPM concentration between the wall and the centerline, or better yet, between the wall and the averaged DPM concentration of the

representative finite pixel volume may not be able to even out by the time-dependent transport processes.

An argument is heard that real-time DPM concentration measurements would have been a better solution for model verification. This is arguable, lacking any tryout experience as no such units were available for the study. Note that the sampling sensors averaged the time-dependent concentrations of approximately 17 full haulage cycles over about 120 continuing measurement periods. If a real-time DPM measurement unit were used with a 1 minute acquisition time, 120 samples would have been necessary to evaluate at each sensor locations to be equivalent. Looking at the sharp changes in DPM concentration profiles of either the stationary or the moving sensors with time, it is doubtful to expect a more stable average than presented from the integrating samplers of the presented method. Due to all these factors coupled with underground conditions under which the experiment was performed, the results are considered to be within acceptable error.

### 4.3.4 DPM moving source term simulation by applying the SFST model

Two separate DPM transport models are used for simulating both LS ad RS drifts sections using an original development in a submitted manuscript form (Danko, 2014b). The connection between the two model sections is the loading machine crossing from one to the other in a cyclic manner (Asante, 2014, Danko, 2014b, Danko, 2016, Danko and Asante, 2017). The loading machine's diesel exhaust source travels with a velocity of $v_{LHD}$=2.18 m/s for the entire experimental with the airflow moving with a travel velocity of $v_{air}$=1.3 m/s. The cycle time diagram for the machine and the airflow directions is shown in Figure 4-33. A background DPM concentration of 90 μg/m$^3$ measured at the

airflow intake to the experimental drift is used as a constant additive source in the numerical model. The moving samplers' concentration is modeled by sampling the spatial concentration from the SFST solution at an offset of 2.1 m away from the tailpipe exhaust point. The geometry of the mine experiment is used to setup the model with a fine special mesh of temporal discretization of 1.3 m and 1 second for both separate numerical models for LS and RS. The DPM source tailpipe concentration of 1000 μg/$m^3$ estimated based on measured fuel use for the haulage, tailpipe emission dada, LHD machine data (Asante, 2014).

Three independent simulations with three different dispersion coefficients, $D$=0.05 $m^2$/s, 0.5 $m^2$/s, and 2.5 $m^2$/s are tested with the objective of assessing the effect of dispersion on the predicted DPM concentration from the model. The mathematical model is detailed in publications (Danko, 2016; Danko and Asante, 2017).

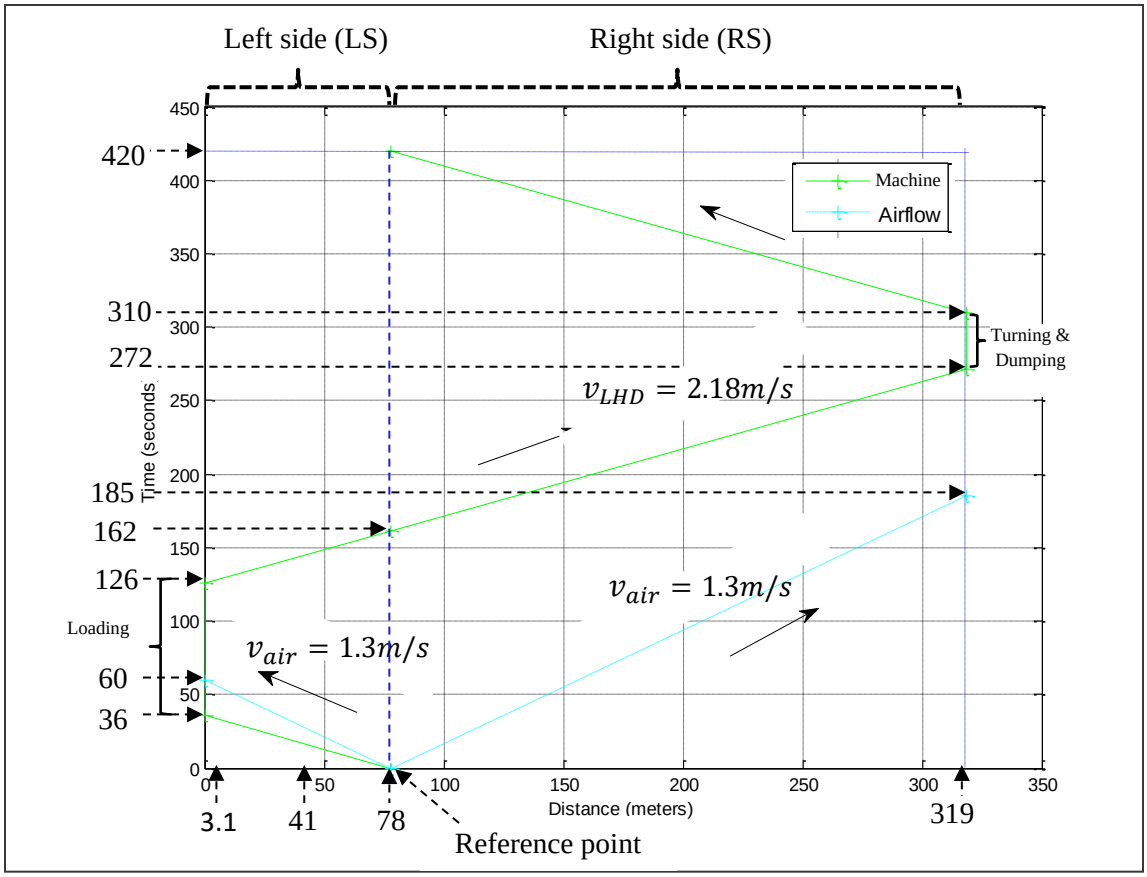


Figure 4-33. Cycle time diagram for the loading machine and the airflow directions (Asante, 2014)

### 4.3.5 Model Results and discussions

Figures 4-34 and 4-35 show the DPM concentration for the LHD tailpipe and the DPM moving samplers (DPM sensors) for the LS and RH segments, respectively with $D$=0.05 $m^2/s$. Similarly, Figures 4-37 and 4-38 depicts that for $D$=0.5 $m^2/s$, with $D$=2.5 $m^2/s$ shown in Figures 4-40 and 4-41. The corresponding concentrations for the stationary sensors are illustrated in Figures 4-36, 4-39, 4-42 with $D$=0.05 $m^2/s$, $D$=0.5 $m^2/s$, and $D$=2.5 $m^2/s$, respectively.

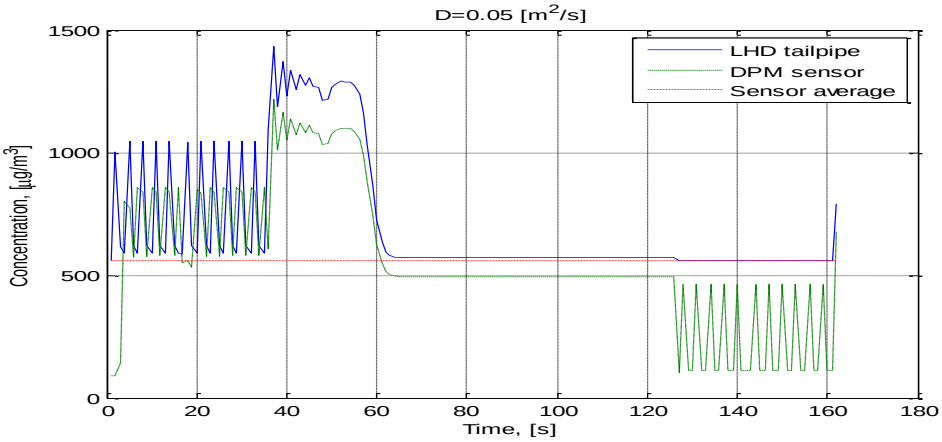


Figure 4-34. Sampled mass concentrations at moving points on the LS drift segment with $D$=0.05 m$^2$/s (Asante, 2014; Danko, 2014b; Danko, 2016; Danko and Asante, 2017)

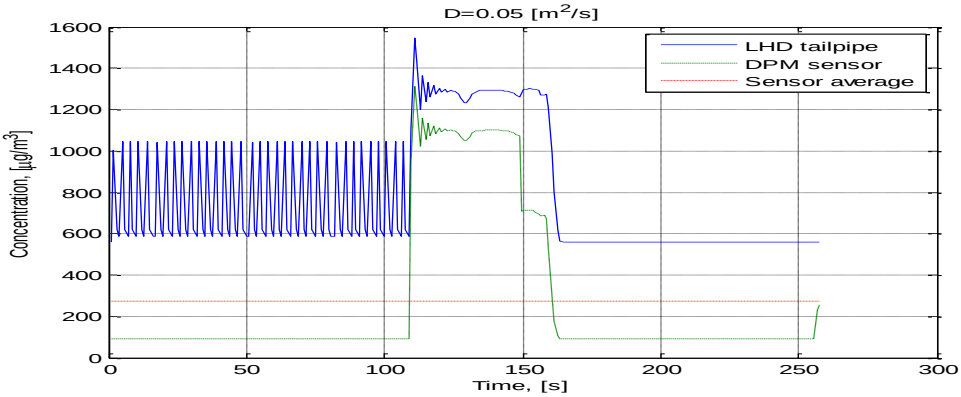


Figure 4-35.Sampled mass concentrations at moving points on the RS drift segment with $D$=0.05m$^2$/s (Asante, 2014; Danko, 2014b; Danko, 2016; Danko and Asante, 2017)

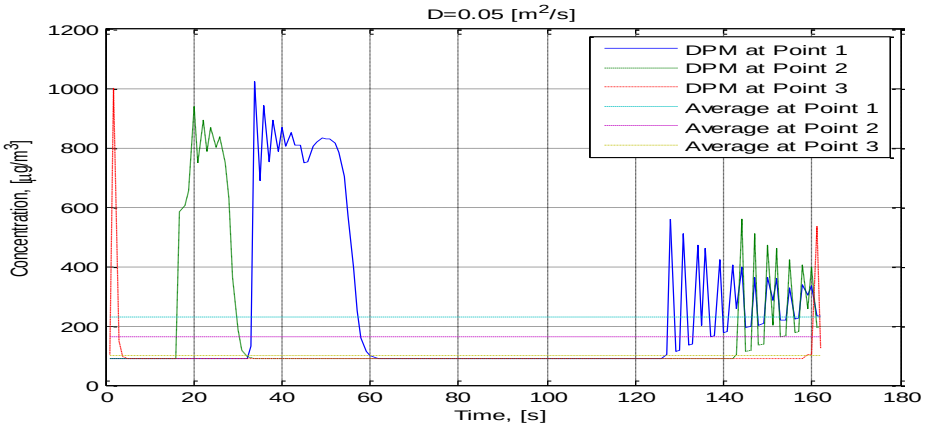


Figure 4-36. Sampled mass concentrations at fixed points on the LS drift segment with $D$=0.05 m$^2$/s (Asante, 2014; Danko, 2014b; Danko, 2016; Danko and Asante, 2017)

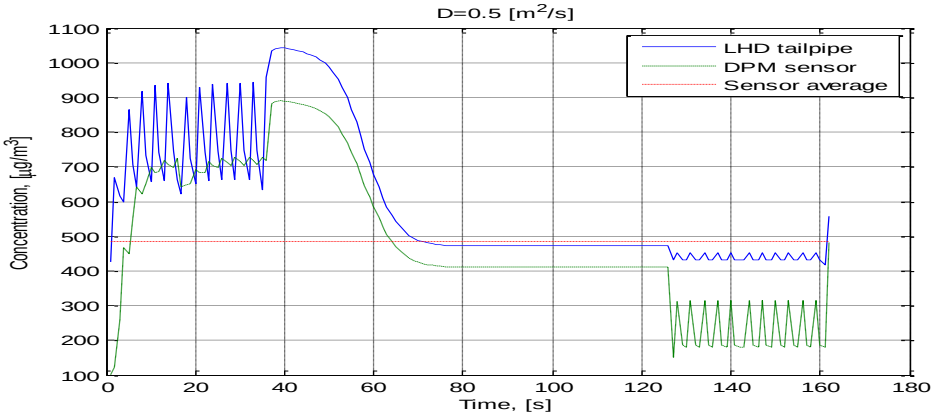


Figure 4-37. Sampled mass concentrations at moving points on the LS drift segment with $D$=0.5 m$^2$/s (Asante, 2014; Danko, 2014b; Danko, 2016; Danko and Asante, 2017)

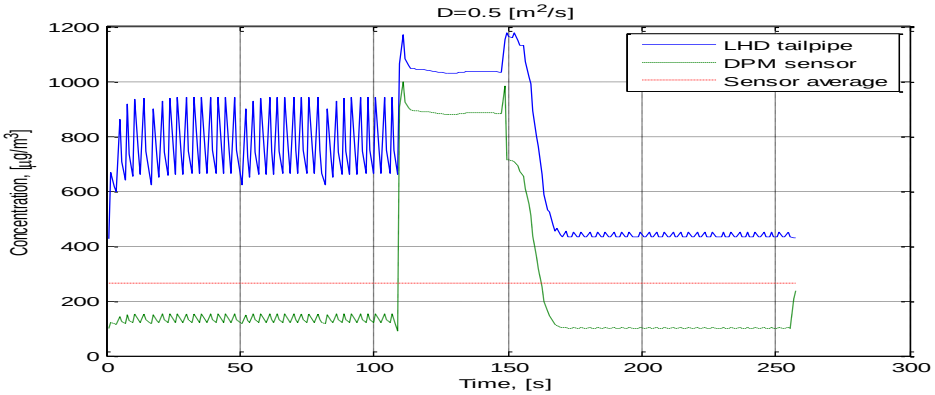


Figure 4-38. Sampled mass concentrations at moving points on the RS drift segment with $D$=0.5 m$^2$/s (Asante, 2014; Danko, 2014b; Danko, 2016; Danko and Asante, 2017)

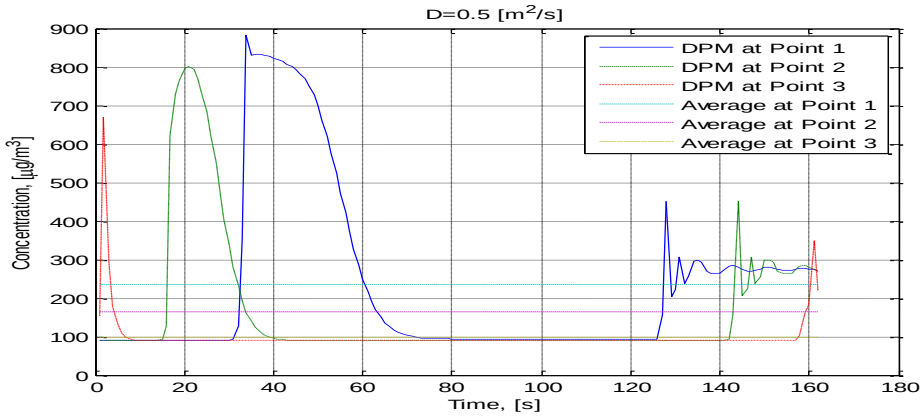


Figure 4-39. Sampled mass concentrations at fixed points on the LS drift segment with $D$=0.5 m$^2$/s (Asante, 2014; Danko, 2014b; Danko, 2016; Danko and Asante, 2017)

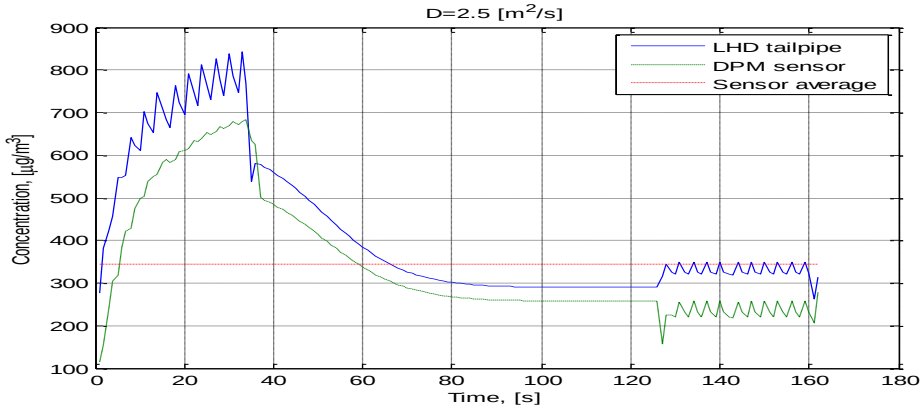


Figure 4-40. Sampled mass concentrations at moving points on the LS drift segment with $D$=2.5 m$^2$/s (Asante, 2014; Danko, 2014b; Danko, 2016; Danko and Asante, 2017)

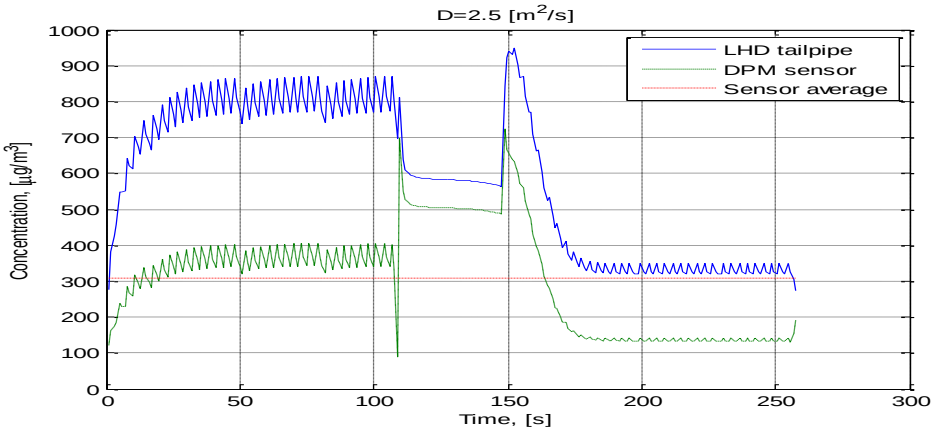


Figure 4-41. Sampled mass concentrations at moving points on the RS drift segment with $D$=2.5m$^2$/s (Asante, 2014; Danko, 2014b; Danko, 2016; Danko and Asante, 2017)

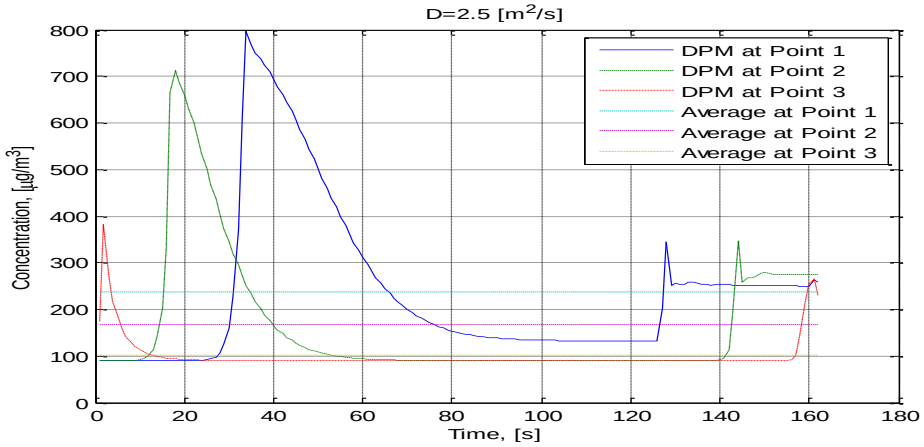


Figure 4-42. Sampled mass concentrations at fixed points on the LS drift segment with $D$=2.5 m$^2$/s (Asante, 2014; Danko, 2014b; Danko, 2016; Danko and Asante, 2017)

#### 4.3.5.1 LS, LHD tailpipe and moving sampler (sensor) concentration variations

The DPM concentration at the tailpipe exit point has a sawtooth-shape fluctuation for the *inby* section. The amplitude of fluctuation does not change with $D$=0.05 $m^2/s$, Figure 4-34. This can be attributed to a number of factors, (1) the low dispersion coefficient resulting in less spread of the contaminant; (2) the machine always encountering a portion of fresh air with background concentration at the time of entering a new airway section of which is then charged by the source term resulting in a near-constant $\Delta\omega$ (and corresponding volumetric concentration) change (Danko and Asante, 2017); and (3) the LHD machine speed being higher than that of the air causing partial dilution which introduces some additional pollutant source to the tailpipe fumes at the next section as the machine moves. The DPM concentration tends to move towards the background concentration as a starting source with decreasing variation in the amplitude of the sawtooth for higher dispersion (Figures 4-37 and 4-40). This is due to large spread of the contaminant transport.

The DPM concentration is shown to be sensed by the moving sensor very well over the entire length of the *inby* section in Figure 4-34, due to the favorable LHD movement direction for the exhaust plume in this section as illustrated in Figure 4-32, with the DPM sensor in the plume behind the tailpipe. It is assuring to see that the starting concentration of the moving sensor is at the background value and that the amplitude of the sawtooth variation is smaller, due to dispersion over a larger distance of the offset of 2.1 m that is larger than the value of $\Delta x = 1.3$ m. With increased dispersion shown in Figures 4-37 and 4-40, the DPM concentration from the moving sensor is getting smoother following very well the concentration of the tailpipe emission curve (Danko and Asante, 2017).

The DPM concentration at the tailpipe and the moving sensor in the LS drift section during the *outby* travel of the LHD are very different from that of the *inby* travel, as seen in Figure 4-34. The DPM concentration at the tailpipe appears to be smooth due to traveling against the air flow with low dispersion.

#### 4.3.5.2 RS, LHD tailpipe and moving sensor concentration variations

A similar phenomena as explained in the LS drift section are observed for the DPM concentration at the tailpipe exit point for the *inby* and *outby* sections of the RS drift section shown in Figures 4-35, 4-38, and 4-38 with dispersion coefficients of $D$=0.05 $m^2/s$, $D$=0.5 $m^2/s$, and $D$=2.5 $m^2/s$, respectively. However, the difference is that, unlike the LS, the DPM concentration is shown not to be sensed by the moving sensor very well over the entire length of the *inby* section. For the *outby* section, the moving sensor concentration slightly increases at the start of the section due to the LHD meeting the fume that is left behind by the tailpipe source as a result of the short dumping time and the late arrival time of the air flow. Similar trends can be seen with increased dispersion coefficients in Figures 4-38 and 4-41 (Danko and Asante, 2017).

#### 4.3.5.3 LS, stationary drift location sensors

The stationary drift sensors at the LS drift section show increasing concentrations in the *inby* section in Figure 4-36 as the LHD moves from the reference point to the loading point. This is due to the lower velocity of the air than that of the tailpipe DPM source. The sensors show a fluctuation in concentration with a reduced amplitude in the *outby* section in Figure 4-36 upon the return of the LHD. This is caused by the counter-direction of the air flow to

the LHD and the phenomena of the sampling effects upon the concentration variations with moving air and source explained in the foregoing (Danko and Asante, 2017).

The calculated cycle weighted averages (CWA) using weight factors of 162 seconds for LS and 258 seconds for the RS is as follows (Asante, 2014; Danko and Asante, 2017):

$$\mathrm{CWA} = \frac{\left(LS_{av}(\frac{\mu g}{m^3})\times 162s\right)+\left(RS_{av}(\frac{\mu g}{m^3})\times 258s\right)}{420s\ (Total\ Cycle\ Time)} \quad (4\text{-}1)$$

where:

$LS_{av}$ = Left side average concentration ($\mu g/m^3$)

$RS_{av}$ = Right side average concentration ($\mu g/m^3$)

The $RS_{av}$ used for the stationary sensors is 90 $\mu g/m^3$, which is the background concentration entered into the model. Table 1 summarizes the CWA obtained from the SFST model for the different dispersion coefficients.

As seen in Table 4-4, different dispersion coefficients in the model do not have much effect on the average concentration values.

Table 4-4. Summary of CWA from the SFST model for different dispersion coefficients (Asante, 2014)

| D= 0.05 $m^2/s$ | |
|---|---|
| | CWA ($\mu g/m^3$) |
| Moving sensor: | 384 |
| Fixed point 1($m_1$): | 144 |
| Fixed point 2($m_2$): | 118 |
| Fixed point 3($m_3$): | 93 |
| D= 0.5 $m^2/s$ | |
| Moving sensor: | 349 |
| Fixed point 1($m_1$): | 145 |
| Fixed point 2($m_2$): | 119 |
| Fixed point 3($m_3$): | 94 |
| D= 2.5 $m^2/s$ | |
| Moving sensor: | 321 |
| Fixed point 1($m_1$): | 147 |
| Fixed point 2($m_2$): | 119 |
| Fixed point 3($m_3$): | 94 |

Comparison of DPM measurement data with the SFST model simulation results is shown in Table 4-5 for different dispersion coefficients. The concentration values predicted by the SFST model for all different dispersion coefficients are in very good agreement with the measured concentration values from the mine. The model errors relative to the measured concentration are within acceptable range.

Table 4-5. Comparison of measurement data with model results using different dispersion coefficients (Danko and Asante, 2017)

| Sensor Location | Measured µg/m$^3$ | Model with *D*=0.05 m$^2$/s (CWA) µg/m$^3$ | Model with *D*=0.5 m$^2$/s (CWA) µg/m$^3$ | Model with *D*=2.5 m$^2$/s (CWA) µg/m$^3$ | Matching error between measurement and SFST simulation at D=0.05 m$^2$/s (%) | Matching error between measurement and SFST simulation at D=0.5 m$^2$/s (%) | Matching error between measurement and SFST simulation at D=2.5 m$^2$/s (%) |
|---|---|---|---|---|---|---|---|
| Moving Sensor | 330 | 384 | 349 | 321 | +16.4 | +5.8 | -2.7 |
| Point 1 | 140 | 144 | 145 | 147 | +2.9 | +3.6 | +5 |
| Point 2 | 88 | 118 | 119 | 119 | +34.1 | +35 | +35.2 |
| Point 3 | 103 | 93 | 94 | 94 | -9.7 | -8.7 | -8.7 |

### 4.3.6 Operator's DPM concentration exposure level estimation per cycle

The cycle is commenced by the machine operator traveling inside the enclosed cabin from the reference point to the loading point. Figure 4-43 depicts the schematic of operator's movement in and out from the enclosed cabin.

Upon reaching the loading area, the operator steps out from the cabin 4 m away from the machine and remotely operates the machine to load the material. After loading the material with the bucket of the machine the operator steps into the cabin and manually operates the machine to the dumping point. The cycle is repeated for 17 times for 2 hours with a cycle time of 7 minutes. The schematic of operator's movement in and out from the enclosed cabin with distance per cycle is shown in Figure 4-44 with Figure 4-45 demonstrating the schematic of operator's movement in and out from the enclosed cabin with time per cycle. During the travel time when the operator is inside the enclosed cabin, his DPM concentration exposure level is minimal due to the 90% average efficiency (Noll et al,

2008, 2011, and 2014) of the environmentally enclosed cabin in filtering DPM from the mine air. Therefore, with a tailpipe source term of 1000 µg/kg/s (833 µg/$m^3$/s) at full engine horse power, the operator will be exposed to 83.3 µg/$m^3$/s DPM concentration representing 10% of tailpipe fume concentration inside the cabin.

When the operator reaches the loading area, he stops and idles the engine and steps out for remote operation. Assuming the engine utilizes about 25% of the rated horse power for idling, then the DPM concentration is 208 µg/$m^3$/s which is 25% of tailpipe concentration (833 µg/$m^3$/s) at full engine power. Therefore, as the operator travels from the machine outside the cabin to fresh air to remotely operate the machine, he walks through the exhaust fumes for about 10 seconds his exposure level is 208 µg/$m^3$/s.

During the loading time, the operator is in fresh air all the time. Consequently, the only concentration he/she is exposed to is the background concentration which was measured during the mine experiment as 90 µg/$m^3$ (Asante, 2014).

During the traveling time from the loading point to the dumping point the operator is inside the cabin all the time until he returns to the loading point to repeat the cycle. His/her exposure level throughout this period is 83.3 µg/$m^3$/s. Table 4-6 shows the summary of machine operator's movement in and out of cabin and DPM exposure level for each section of the experimental drift.

Table 4-6. Summary of machine operator's movement in and out of cabin and DPM exposure level.

| Machine operator movement | Time of exposure (Seconds) | DPM concentration (833µg/m$^3$) |
|---|---|---|
| OPIC | 36 | 83.3 |
| OPOC | 10 | 208 |
| OPOC | 70 | 90 |
| OPOC | 10 | 208 |
| OPIC | 36 | 83.3 |
| OPIC | 110 | 83.3 |
| OPIC | 38 | 83.3 |
| OPIC | 110 | 83.3 |

OPIC: Operator Inside Cabin
OPOC: Operator Outside Cabin

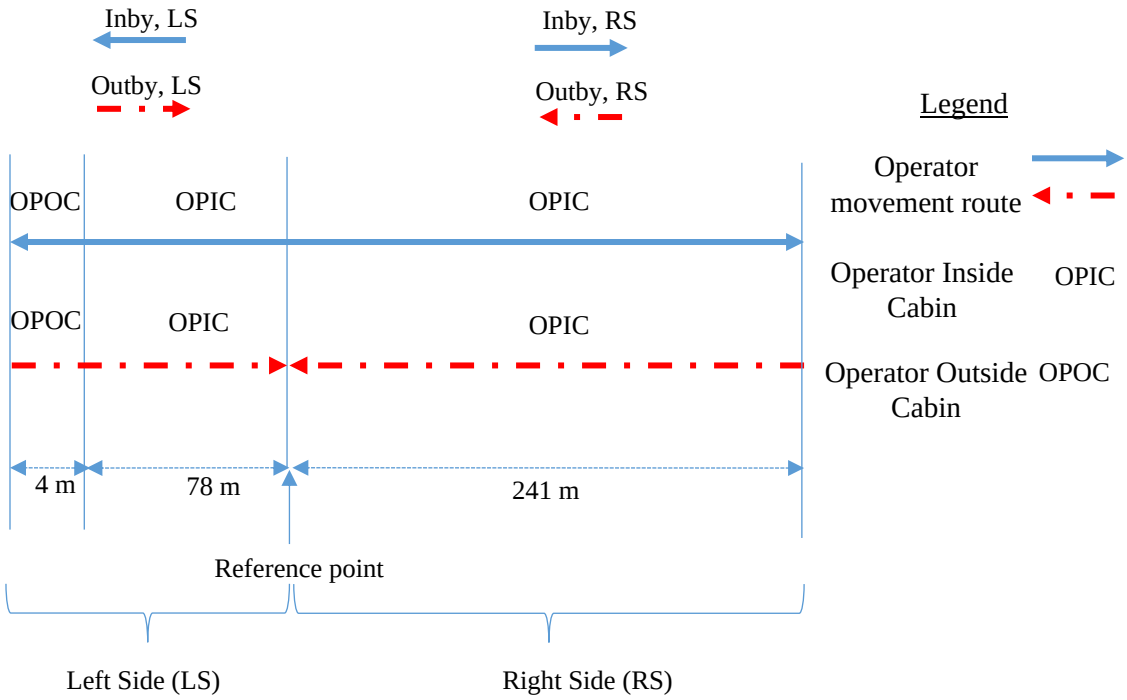


Figure 4-43. Schematic of operator's movement in and out from the enclosed cabin

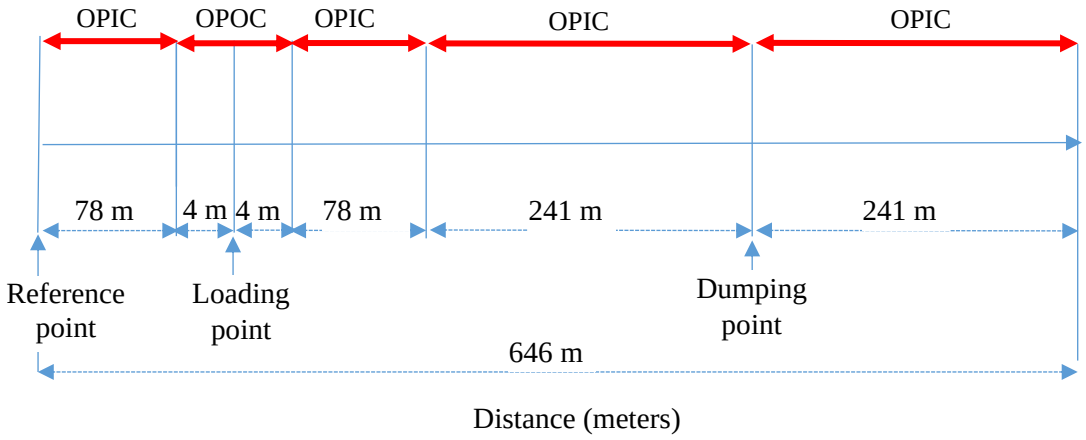


Figure 4-44. Schematic of operator's movement in and out from the enclosed cabin with distance per cycle

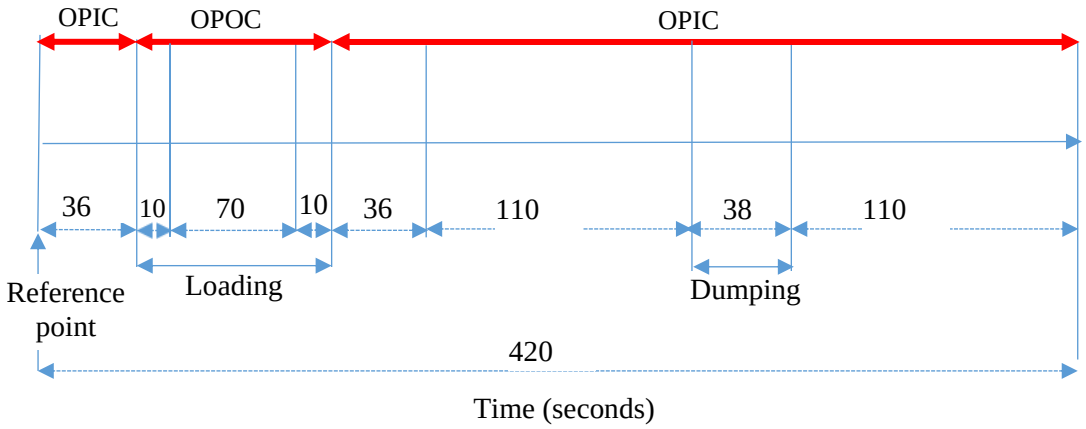


Figure 4-45. Schematic of operator's movement in and out from the enclosed cabin with time per cycle

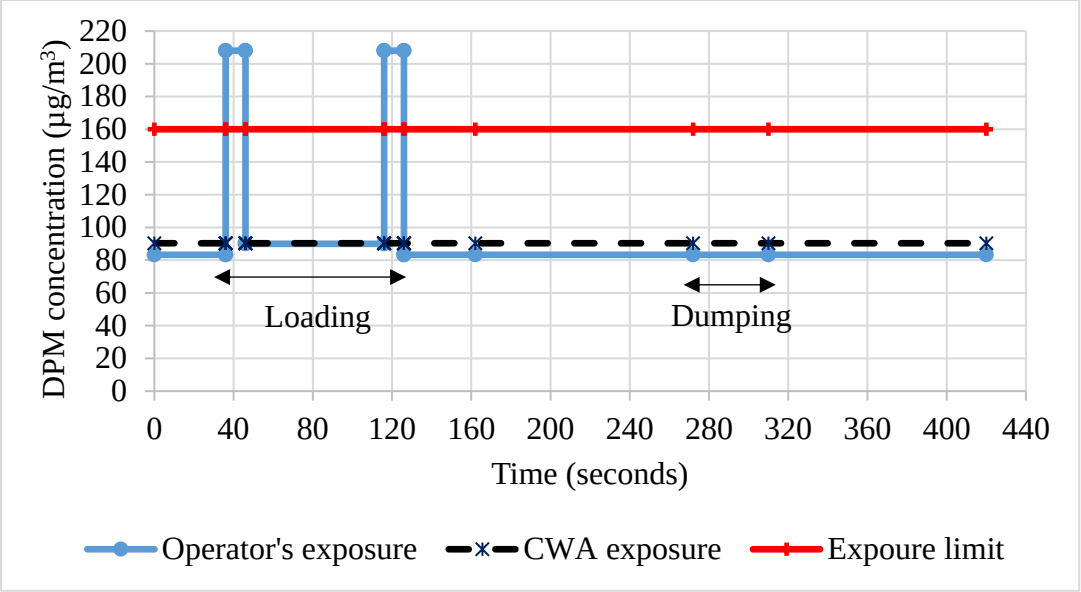


Figure 4-46. Operator's DPM concentration exposure level estimation per cycle time

### 4.3.7 Conclusions

- The estimated machine operator's DPM concentration level per cycle time is depicted in Figure 4-46. As shown, the average exposure level, CWA is about 90 µg/m$^3$ over an 8-hour time period, significantly below the allowable maximum value.
- The question must be kept unanswered weather a personal sampler could provide a more accurate way to determine the operator's exposure level than an averaging sampler used in the study until personal samplers are available for the operators. Due to the large concentration variations from the simulation with time, the dynamic response of any personal sensor will be certainly critical to the accuracy of the integrated result.

- Nevertheless, the model-based prediction is working and can be used as described during the design phase without experimenting with human subjects during real-time mining operations.
- Only the input data for the designed ventilation system (geometry and air flow rates) as well as for the selected LHD machine (tailpipe emission concentration and tailpipe flow rate of the exhaust fumes) are needed to map out the entire time-space DPM variation in the haulage route during the entire haulage operation.

## 5.0 Chapter 5- Research contributions

### 1. Forecast in space

Contaminant concentration monitoring in underground mines is typically performed at strategic places with few sensors. The problem is that a critical location which may have concentration increase that could lead to threshold crossing, and may not necessarily be monitored. To consider, a critical location may not be accessible; or it may not be known; or may not be enough sensors to monitor its location. An unmonitored, but critical location (which may be in between two monitored locations) can be checked with a well-matched model with correct dynamic behavior with time and in space. Critical concentrations in all locations in the mines must be checked for including the unmonitored locations. With a ventilation model, any future concentration increase at any location can be forward predicted and measures can be taken to mitigate imminent threshold crossing.

A new and innovative element is studied using sensor data at a monitored location to forward predict concentrations in all locations in mine examples. Using a numerical models, I evaluated the critical concentrations at all locations and matched the spatial distribution of the solution with those from synthetically generated model data as input at the available monitored concentrations. I analyzed the simulation results and proved that the new modeling approach is an improvement on the sensors' limitation in the current monitoring system which may hamper their direct usefulness in disaster avoidance. I concluded that data from the atmospheric monitoring system (AMS) as well as mine production data (MPD) are both needed for a forecast in space and time model, illustrated in Figure 5-1.

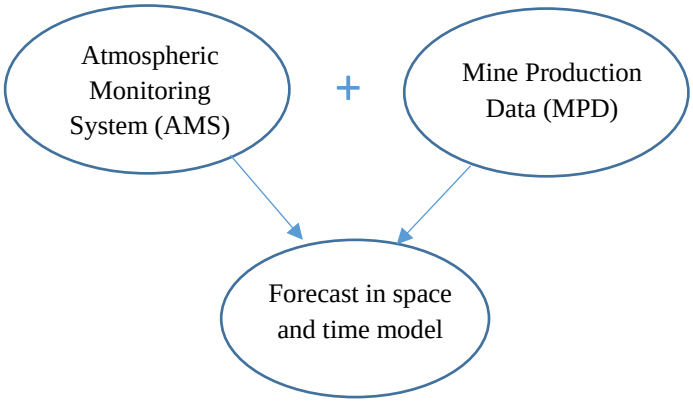


Figure 5-1. Forecast in space and time model inputs

**2. Delayed processes related to travel time**

A traveling concentration front may encounter another concentration build up from a distributed source. The traveling front leads to gas accumulation hazard with climbing slope of concentration due to delay time and may cross the threshold. In an underground mine, there are numerous distributed sources with different airflows and velocities which may contribute to gas accumulation at a downstream location. Therefore, the mixing equation becomes more complex and it is necessary to have a numerical model capable of handling such a problem.

I proved by numerical simulations that even if the individual gas concentration signals from sensors at fixed monitoring locations all stay below the threshold for safety, there may be dangerous concentrations due to accumulation from gas sources along the airway in other locations. Such critical points with likely safety threshold crossings can be forward-predicted by the Early-Warning Predictor of the Early-Warning System. The system can notify mine ventilation management of the nature of the hazard scenario for preventive action. Since high concentration fronts travel with the air velocity in the mine, precious time may be available to prevent the disaster from happening by timely intervention.

I analyzed and interpreted the signals from the simulation results to show that there is always a delay time in the signal regardless of threshold crossing which can be identified earlier on, proving the early-warning system concept. I identified the ranges of the delay time (7-29 minutes) in five scenarios and concluded that the delay time gives realistic time frame for preventive action by mine management.

**3. Delayed processes related to the effects of barometric pressure variations**

Barometric pressure changes result in pressure-driven methane liberation from the gob into the mine airway associated with response delay. I proved by numerical simulations that although no problem may be caused by methane release due to slow barometric pressure changes under normal weather conditions, sudden change induces methane liberation from the gob into the airway. It is very difficult to foresee a future concentration increase from the raw measurement data from a sensor. However, I have shown that time-dependent ventilation air model can indeed predict an increase in methane concentration variation in future time in response to a sudden pressure decrease in the mine.

I demonstrated that barometric pressure variation may become dangerous. However, accident-prone atmospheric conditions may be difficult to notice. It is necessary to use a ventilation and contaminant model in forward-predicting mode to foresee the outcome of real-time atmospheric pressure variation at future times. In one example, a gain time of 21 minutes is determined from the simulation results for the mine management to take action for the prevention of an imminent accident. I demonstrated the use of an innovative, forward-predicting model-element using the Numerical Transport Code Functionalization (NTCF) technique for strata and gob gas source simulation as a root-cause element of the early-warning system for predicting gas inflow to the ventilating air.

# 6.0 Chapter 6- Conclusions and Recommendations

## 6.1 Conclusions

- The research study shows promising results of the Early-Warning System in identifying hazard-causing atmospheric conditions in their evolution toward an accident in the mine ventilating air based on analyzing monitored data against a calibrated mine ventilation, heat and contaminant transport model.
- A powerful, forward-predicting simulator in the MULTIFLUX software is demonstrated as an Early-Warning Predictor with unprecedented speed and mine-size capacity.
- The early warning system is tested against typical simulated error signals for potential hazard scenarios under controlled conditions. The test results are conclusively positive. Significant time gain, in the order of 20 minutes is seen in the examples between the hazard detection time and the critical threshold crossing time at some critical locations.
- The early warning system can forward predict the concentration values downstream of monitored locations before hazardous changes get into critical threshold crossing, giving sufficient time to avoid the accident from happening.
- It is good to have a sensor that sounds an alarm at the threshold value but it is not good enough to wait for the threshold crossing when the mine has to stop operation or evacuate miners at the instant of violating that limit value. Lowering the threshold value at the sensor location to predict threshold crossing at another

location does not solve the problem correctly since the concentration curves take different shapes with time and not obey proportionality by a multiplying factor.

- A new, powerful, fully-implicit SFST solution is applied for interpreting measurement results for DPM contaminant concentration variations from a moving machine in an underground mine. The numerical model provides a link between the time-averaged and the peak DPM concentration values at the tailpipe. Very good match was obtained for all three stationary sensors in the haulage drift as well as the two moving sensors between in situ measurement results and the SFST model simulation results.
- It is shown that the DPM concentration variations with location and time in the air of the mine can be predicted from the known tailpipe DPM concentration from machine smog tests and the fuel consumption of the diesel machine.
- Therefore, the numerical model may be used to evaluate the average concentration exposure value of the DPM for compliance analysis without real-time, complicated DPM measurements, relying basically on tailpipe smog test, fuel consumption and the SFST contaminant transport model, incorporated in the mine ventilation model.
- With the simulation of total, accumulated DPM concentration at the working area, mining companies may be able to implement the appropriate ventilation strategies to reduce or eliminate harmful DPM exposure to mine workers.

## 6.2 Recommendations

- Continuous monitoring of atmospheric conditions together with the early warning system (EWS) software may be implemented by underground mines to forecast

possible future concentration increase and threshold crossing at downstream locations. The concept of using real-time atmospheric systems and mine production data with a predictive model for real-time early warning can be implemented in mines to gain time necessary for taking accident-preventive measures.

- A calibrated ventilation air model (VAM) is needed for achieving reliable predictive results from the EWS.
- The evaluation of the average diesel particulate matter (DPM) concentration with a numerical model could be advantageous in preventing over-exposure of mine workers to DPM concentrations and to maintain compliance to regulatory limit. This will help safe guard the health and safety of mine workers.

## 7.0 References


1. Asante, W., (2014), “Mine-wide Diesel Particulate Matter (DPM) Monitoring Applications.” M.S. Thesis, University of Nevada, Reno, p. 1-89.
2. ACGIH (1990), “Threshold limit values and biological exposure indices for 1990-1991.” American Conference of Governmental Industrial Hygienists, Cincinnati, Ohio, USA. Vol 35, p. 1-122.
3. Belle, B., (2014), “Evaluation of barometric pressure (BP) and cage effect on longwall tailgate gas levels.” Proceedings of the 10th International Mine Ventilation Congress. The Mine Ventilation Society of South Africa. Sun City, South Africa, p. 501-511.
4. Boyer, R.F., (1964), “Coal mine disasters: Frequency by month.” Science, vol. 144.19, p. 1447-1448.
5. Carter H.N., Durst C.S., (1955), “The influence of barometric changes on the emission of firedamp.” Trans Inst Mining Engineering. 115, p. 3–29.
6. Code of Federal Regulations, 30 CFR Part §75.351, (1996), “Atmospheric Monitoring Systems for coalmines.” Washington, DC: U.S. Government Printing Office, Office of the Federal Register. https://www.ecfr.gov/cgi-bin/text-idx?SID=df0024be22c993fd489a45e0195b102c&mc=true&node=se30.1.75_1351&rgn=div8. Accessed 04/10/17.
7. Code of Federal Regulations, 30 CFR Part §57.5060, (1996), “Limit on exposure to diesel particulate matter.” https://www.ecfr.gov/cgi-bin/text-

idx?SID=df0024be22c993fd489a45e0195b102c&mc=true&node=se30.1.57_15060&rgn=div8. Accessed 04/10/17.

8. Code of Federal Regulations, 30 CFR Part §57.22301, (1996), "Atmospheric Monitoring Systems for methane." https://www.ecfr.gov/cgi-bin/text-idx?SID=df0024be22c993fd489a45e0195b102c&mc=true&node=se30.1.57_122301&rgn=div8. Accessed 04/10/17.
9. Code of Federal Regulations, 30 CFR Part §75.323, (1996), "Actions for excessive methane." https://www.ecfr.gov/cgi-bin/text-idx?SID=9dac3448d68eb8a929c4fe85d6e80dfe&mc=true&node=se30.1.75_1323&rgn=div8. Accessed 04/10/17.
10. Code of Federal Regulations, 30 CFR Part §57.5001, (1996), "Exposure limits for airborne contaminants for metal and nonmetal mine." https://www.ecfr.gov/cgi-bin/textidx?SID=afe26224d95f953de95953247e8e288c&mc=true&node=se30.1.57_15001&rgn=div8. Accessed 04/10/17.
11. Code of Federal Regulations, 30 CFR Part §57.5005, (1996), "Control of exposure to airborne contaminants for metal and nonmetal mine." https://www.ecfr.gov/cgi-bin/textidx?SID=afe26224d95f953de95953247e8e288c&mc=true&node=se30.1.57_15005&rgn=div8. Accessed 04/10/17.
12. Code of Federal Regulations, 30 CFR Part §57.5002, (1996), "Exposure monitoring of airborne contaminants for metal and nonmetal mine." https://www.ecfr.gov/cgi-bin/textidx?SID=afe26224d95f953de95953247e8e288c&mc=true&node=se30.1.57_15002&rgn=div8. Accessed 04/10/17.

13. Code of Federal Regulations, 30 CFR Part §57.5071, (1996), "DPM Exposure monitoring." https://www.ecfr.gov/cgi-bin/text-idx?SID=6f4d0698c1e07d50eda128e8e05a1c75&mc=true&node=se30.1.57_15071&rgn=div8. Accessed 04/10/17.
14. Danko, G., (2006), "Functional or Operator Representation of Numerical Heat and Mass Transport Models." ASME J. of Heat Transfer, Vol. 128, p. 162-175.
15. Danko, G., (2008), "MULTIFLUX V5.0 Software Documentation Qualification Documents." Software Tracking Number: 1002-5.0-00, Software Management Office, Berkeley National Laboratory, p.1-1007, according to 10 CFR. Part 830.
16. Danko G., Birkholzer J., Bahrami D., (2008), "Coupled In-Rock and In-Drift Hydrothermal Model Study for Yucca Mountain." Nuclear Technology Vol. 163, p. 110-128.
17. Danko G., (2013), "Subsurface flow and transport process model for time dependent mine ventilation simulations." Institute of Materials, Minerals and Mining and the AusIMM. DOI 10.1179/147490013X13639459465691. Mining Technology 2013. Vol 122 No 3, p. 134-144.
18. Danko G., Bahrami D., 2008, "Application of MULTIFLUX for air, heat and moisture flow simulations." 12th U.S./North American Mine Ventilation Symposium, Reno, NV, p. 267-274.
19. Danko, G., (2012), "Ventilation and climate control of deep mines." McGraw-Hill 2012 Yearbook of Science and Technology, p. 296-299.

20. Danko G., (2014a), “Safety, Health, and Ventilation Cost Optimization with Simulation and Control.” Final Report submitted to NIOSH, Grant Number: 200-2009-30157, p. 1-228.
21. Danko G., (2014b), “Finite State-flux Network Model for the Conservative Solution of Advection and Diffusion Transport.” Manuscript, submitted to Journal of Engineering Mathematics, p. 1-22.
22. Danko, G., Bahrami, D., and Fox, J.E., (2013), “Modeling of strata gas liberation into the mine drifts with time-dependent ventilation.” 2013 SME Annual Meeting and Exhibition, Denver, CO, presentation.
23. Danko, G., and Bahrami, D., (2014), “Contaminant Species Modeling With Advection, Dispersion, and Stratification in Ventilation Networks.” 10th Int. Mine Ventilation Congress, August 2-8, 2014, Sun City, South Africa, p. 379-387.
24. Danko, G., Bahrami, D., Asante W., (2016), “Early-Warning Safety Hazard Predictor for Preventive Ventilation Management.” Final Report submitted to Alpha Foundation, Grant Number: 1321 114 09CV, p. 1-120.
25. Danko, G., (2016), “Model Elements and Network Solutions of Heat, Mass and Momentum Transport Processes.” Springer-Verlag GmbH, Germany, p. 1-256. Ebook http://link.springer.com/book/10.1007%2F978-3-662-52931-7.
26. Danko, G., Asante W., (2017), “Time-dependent contaminant transport in ventilating air from a moving source.” Applied Mathematics. Vol.8 No.5. p. 1-22.
27. EPA, (2001), “Nonroad diesel emission standards.” Staff technical paper. Washington, DC: U.S. Environmental Protection Agency, EPA420-R-01-052.

28. EPA, (2002), “Health assessment document for diesel engine exhaust.” Washington, DC: U.S. Environmental Protection Agency, EPA/600/8-90/057F.
29. Fauconnier CJ (1992), “Fluctuations in barometric pressure as a contributory factor to gas explosions in South African mines.” Journal of the South African Institute of Mining and Metallurgy. Vol. 92, No. 5, p. 131–147.
30. Gray, R.M., and Davisson, L.D., (2000), “An Introduction to Statistical Signal Processing.” Book, Cambridge University Press, p. 1-475.
31. Griffin K. R., (2013), “Utilization and Implementation of Atmospheric Monitoring Systems in United States Underground Coal Mines and Application of Risk Assessment.” A dissertation submitted to the faculty of Virginia Polytechnic Institute and State University in partial fulfillment of the requirements for the degree of Doctor of Philosophy in Mining Engineering, p. 1-178.
32. Hartman H. L, Mutmansky J.M, Ramani R. V, Wang Y.J., (1997), “Mine ventilation and air conditioning.” New York: John Wiley and Sons.
33. International Agency for Research on Cancer, (2012), “Diesel Engine Exhaust Carcinogenic.” Press release. www.iarc.fr/en/mediacentre/pr/2012/pdfs/pr213_E.pdf.
34. International Agency for Research on Cancer, (1989), “IARC Monographs on the Evaluation of Carcinogenic Risks to Humans.” Diesel and Gasoline Engine Exhausts and Some Nitroarenes, Monograph 46, p. 41-57.
35. Jianqing F., and Qiwei, Y., (2003), “Nonlinear Time Series-Nonparametric and Parametric Methods.” Springer-Verlag, New York, Berlin, Heidelberg. ISBN 0-387-95170-9, p. 1-88.

36. Jong E. C., Luxbacher, K. D., Karmis, M. E., and Westman, E. C., (2013), "Field test of a perfluoromethylcyclohexane (PMCH) permeation plug release vessel (PPRV) using a dual tracer deployment in an underground longwall mine." Department of Mining and Minerals Engineering Holden Hall, Virginia Tech, personal communications.
37. Karacan, C. Ö., (2008), "Modeling and Prediction of Ventilation Methane Emissions of U. S. Longwall Mines Using Supervised Artificial Neural Networks." National Institute for Occupational Safety and Health, Pittsburgh Research Laboratory, Pittsburgh, PA, 15236, United States. https://www.cdc.gov/niosh/mining/works/coversheet1790.html. Accessed 05/04/17.
38. Kittleson D.D., (1998), "Engines and Nanoparticles: a review." Journal of Aerosol Science, Vol 29, p. 575-588.
39. Lolon S., Brune J., Gilmore R., Bogin J., Grubb J., Saki S., Juganda A., (2016) "CFD Studies on the Phenomenon of Gob Breathing Induced by Barometric Pressure Fluctuations." SME Annual Meeting, Phoenix, AZ. Preprint 16-154. p. 1-5.
40. McIntosh C. B. (1957), "Atmospheric Conditions and Explosions in Coal Mines." Geographical Review, Vol. 47, No. 2. p. 155-174.
41. McPherson M.J., (1993), "Subsurface ventilation and environmental engineering." London: Chapman and Hall, p.1-948.
42. Mischler S.E., and Colinet J.F., (2009), "Controlling and Monitoring Diesel Emissions in Underground Mines in the United States." Centers for Disease Control

and Prevention. Proceedings of the Ninth International Mine Ventilation Congress, New Delhi, India, Panigrahi DC, ed., New Delhi, India: Oxford & IBH Publishing Co. Pvt. Ltd., p. 879-888.

43. MSHA, (2009), "DPM Overview, DPM Emission Reduction Methods, and DPM Control Strategies." Presentation. Seminar on DPM, Accessed 1/09/2012. http://www.msha.gov/01995/dieselpartmnm.htm
44. NIOSH, (1988), "Carcinogenic effects of exposure to diesel exhaust." Current Intelligence Bulletin 50, August 1988.
45. NIOSH Method 5040, (2003), "Diesel Particulate Matter (As Elemental Carbon) from NIOSH Manual of Analytical Methods (NMAM)." Fourth Edition. https://www.cdc.gov/niosh/docs/2003-154/pdfs/5040.pdf.
46. Noll J. D., Patts L., and Grau R., (2008), "The effects of ventilation controls and environmental cabs on diesel particulate matter concentrations in some limestone mines." Proceedings of the 12th U.S. North American Mine Ventilation Symposium, Reno, Nevada, 2008. Reno, p. 463-468.
47. Noll J.D., Cecala A.B., Organiscak J.A., (2011), "The Effectiveness of Several Enclosed Cab Filters and Systems for Reducing Diesel Particulate Matter." SME Annual Meeting, Denver, Colorado, Preprint 11-011. Englewood, CO Society of Mining, Metallurgy, and Exploration, Inc.
48. Noll J.D., Cecala A.B., Organiscak J.A., and Rider J.P., (2014), "Effects of MERV 16 filters and routine work practices on enclosed cabs for reducing respirable dust

and DPM exposures in an underground limestone mine." Mining engineering Journal, 66(2), p. 45-52.

49. NTP, (2000), "Report on Carcinogens." Ninth Edition. Department of Health and Human Services.
50. NTP (2011), "Report on Carcinogens." Twelfth Edition. Department of Health and Human Services.
51. Page, N.G., Caudill, S.D., Godsey, J.F., Moore, A.D., Phillipson, S.E., Steffey, D.A., Stoltz, R.T., Watkins, T.R., Cripps, D.R., Maggard, C.J., Morley, T.A., Sherer, H.E., Stephan, C.R., Vance, J.W., and Brown, A.L., (2012), "Fatal Underground Mine Explosion, 2010." Report of Investigation, Upper Big Branch Mine-South, Performance Coal Company, Montcoal, Raleight County, West Virginia, ID No. 46-08436. US Dept. of Labor, MSHA, Coal Mine Safety and Health.
52. Press W.H, Teukolsky S.A., Vetterling W.T., Flannery B.P., (1988), "Numerical Recipes in C: The Art of Scientific Computing." Second Edition (ISBN 0-521-43108-5). Copyright (C) 1988-1992 by Cambridge University Press, p. 650-655.
53. Ren T. X. and Edwards J. S., (2000), "Three-dimensional computational fluid dynamics modelling of methane flow through permeable strata around a longwall face." Transactions, Institution of Mining and Metallurgy, p. A41-A48.
54. Schatzel, S. J., Karacan, C, Ö, Krog, R. B., Esterhuizen, G. S., and Goodman, G. V., (2008), "Guidelines for the Prediction and Control of Methane Emissions on Longwalls." National Institute for Occupational Safety and Health, DHHS (NIOSH) Publication No. 2008-114, Information Circular 9502, p. 1-83.

55. Shumway, R. H., and Stoffer, D. S., (2010), “Time Series Analysis with Applications.” 3nd edition, Springer, New York, Dordrecht, Heidelberg, London, DOI 10.1007/978-1-4419-7865-3, ISBN 978-1-4419-7864-6.
56. Taylor, G., (1954), “The Dispersion of Matter in Turbulent Flow through a Pipe.” Proc. R. Soc. London, 223, p. 446-468.
57. Time Series, http://en.wikipedia.org/wiki/Time_series, Accessed April, 2015.
58. U.S. Patent No. 7610183B2, (2008), U.S. Patent No. Patent 8396693 B2 (2013), "Multiphase physical transport modeling method and modeling system.”
59. Toraño J, Torno S, Menendez M, Gent M, Velasco J., (2009), “Models of methane behavior in auxiliary ventilation of underground coal mining.” International Journal of Coal Geology 80, p. 35–43.
60. Stevenson JW [1968]. Effects of bleeder entries during atmospheric pressure changes. Mining Engineering Journal: 61–64.
61. Vensim, (2016) Ventsim Visual User Guide, Ventsim Software by Chasm Consulting, PO Box 2006 Aitkenvale Qld 4814, http://www.ventsim.com.
62. VnetPC (2007) VnetPC 2007 User’s Manual and Tutorial, Mine Ventilation Services, Inc. 1625 Shaw Ave #103, Clovis, CA 93611, USA, http://www.mvsengineering.com
63. Wasilewski, S., (2014), “Influence of barometric pressure changes on ventilation conditions in deep mines.” Arch. Min. Sci., Vol. 59, No. 3, Warsaw, Poland, p. 621-639.
64. WHO, (1996), “Diesel Fuel and Exhaust Emissions. International Program on Chemical Safety.” World Health Organization, Geneva.

65. 71 Fed. Reg. 28924 (2006), “Mine Safety and Health Administration: 30 CFR 57-Diesel Particulate matter exposure of underground metal and nonmetal miners. Limit on Concentration of diesel particulate matter.” Code of Federal Regulations. Washington, DC: U.S. Government Printing Office, Office of the Federal Register.

# 8.0 Appendices

## Appendix 1. Model comparison for APPS model qualification and validation

### A1-1 Test example 1 for matching APPS model and VAM model for airflow predictions

This model is a longwall coal mine which has 762 branches and 3 fans. Figure A1-1 shows the for airflow differences between VnetPC and MULTIFLUX models for mine example 1 (coal mine). The difference between the models in the average airflow is 0.42m$^3$/s. The difference between the models in average pressure is 5.6Pa. Figure A1-2 illustrates fan working point's comparison between VnetPC and MULTIFLUX models for the three fans. The maximum difference in pressure and airflow are 72.8Pa and 5.6m$^3$/s, respectively, as depicted in Figure A1-3.

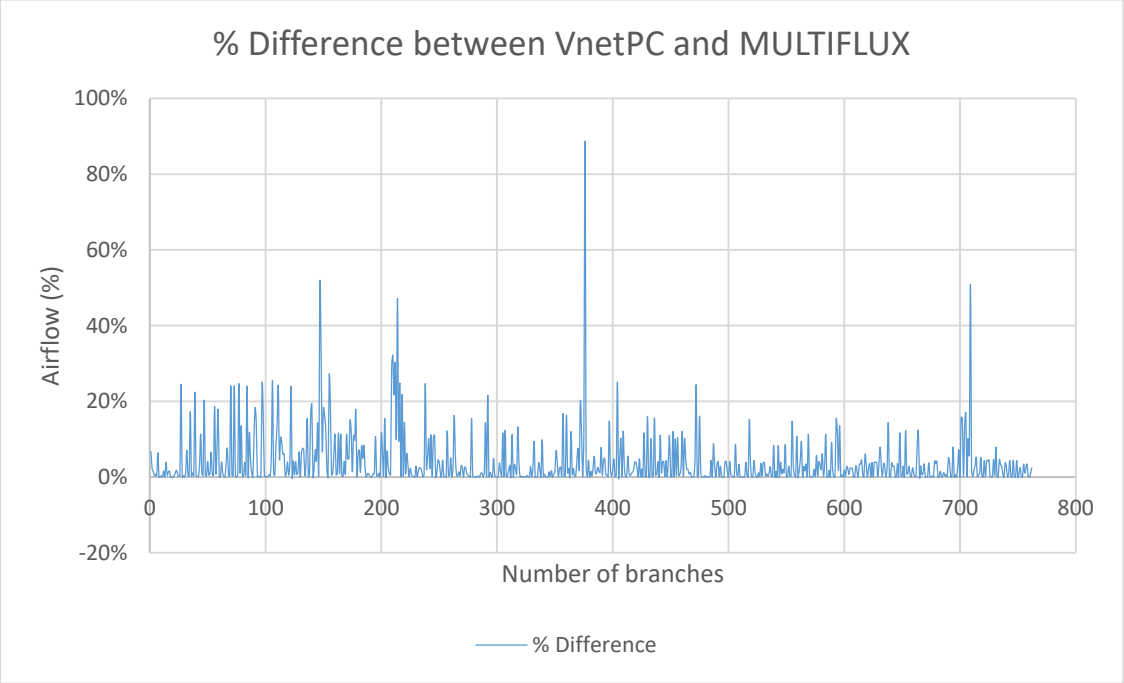


Figure A1-1. Airflow % difference between VnetPC and MULTIFLUX models for mine example 1 (coal mine).

The differences in branch flow rate and pressure averages are insignificant, however, the percentage differences may be significant in airways with low pressure loss and/or air flow rate. The same observation may be made from comparing the fan working points in the VnetPC and MULTIFLUX models.

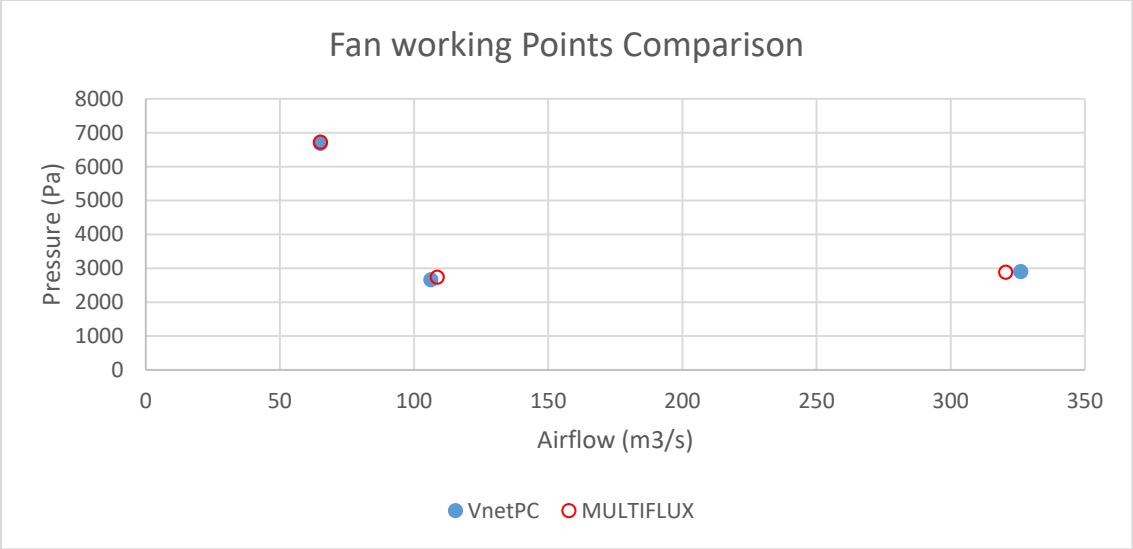


Figure A1-2. Fan working points comparison between VnetPC and MULTIFLUX models for mine example 1 (coal mine).

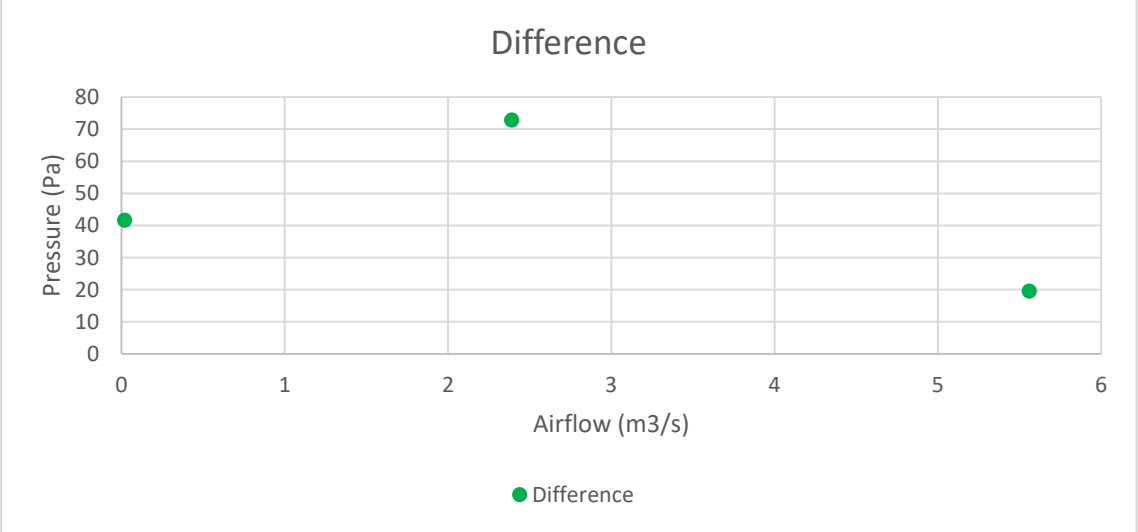


Figure A1-3. Difference for fan working points between VnetPC and MULTIFLUX models for mine example 1 (coal mine).

**A1-2 Test example 2 for matching APPS model and VAM model for airflow predictions**

This is a large model of a metal mine which has 2272 branches with 62 fans. Figure A1-4 shows airflow differences between the VnetPC and the MULTIFLUX models for mine example 2. The difference in average airflow between the models is 0.02m$^3$/s. The difference in average pressures between the models is 7.65Pa. Figures A1-5 and A1-6, respectively, illustrate the fan pressures and fan airflow rates comparison between VnetPC

and MULTIFLUX for the working points of all the fans in the model. The differences in the fan pressures and airflow rates between the two models are, respectively depicted in Figures A1-7 and 1-.8.
The fan working points (WP) for most critical two fans where differences are the highest between the VnetPC and MULTIFLUX are shown in Figures A1-9 and A1-10. As depicted, these fans are not in their proper working range, a problem with the VAM model, which must be accepted.

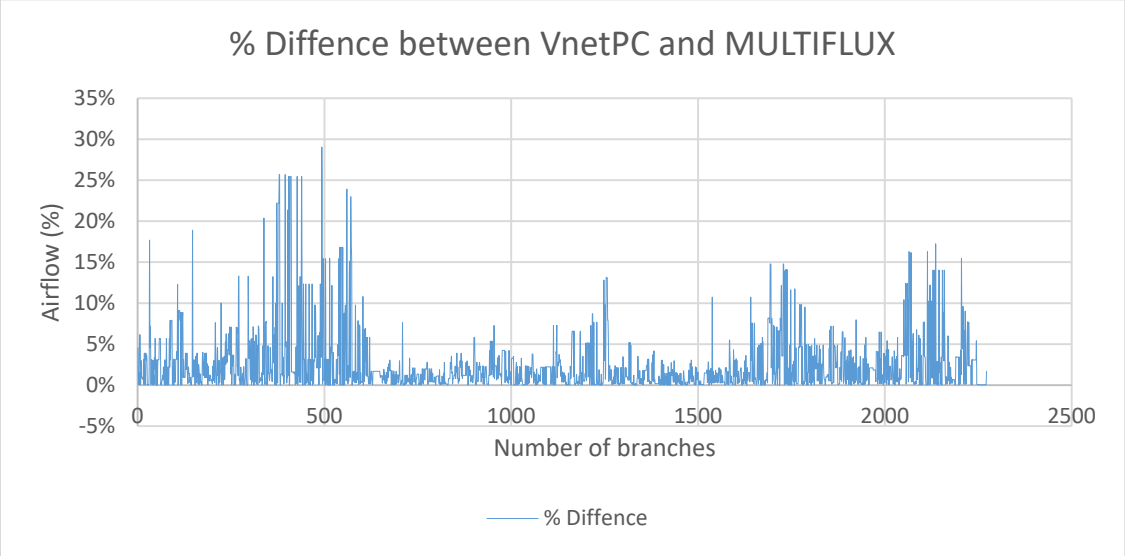


Figure A1-4. Airflow % difference between VnetPC and MULTIFLUX models for mine example 2 (metal mine).

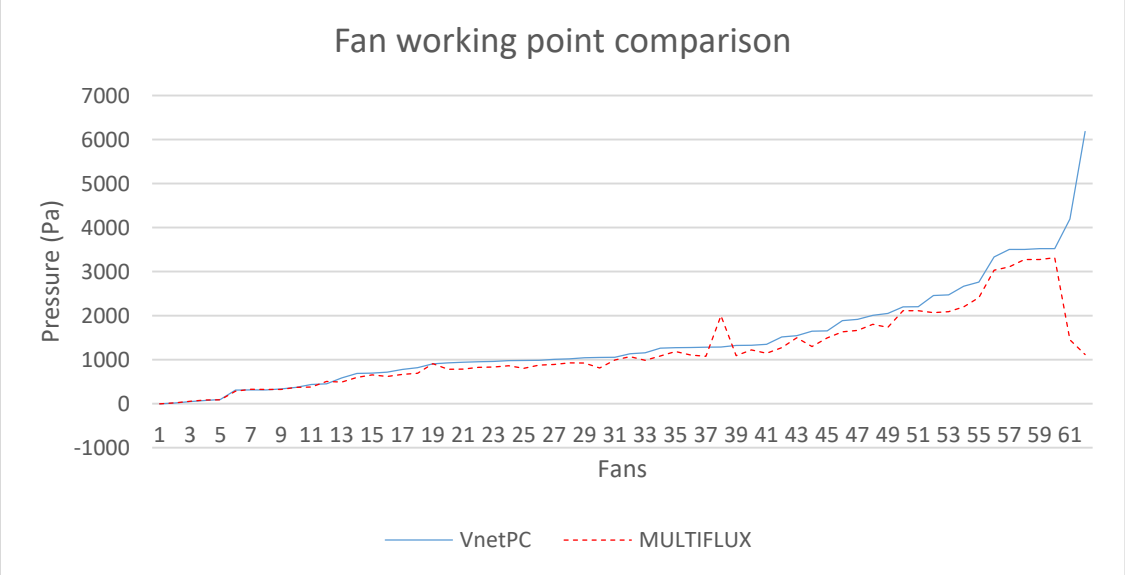


Figure A1-5. Fan pressure comparison between VnetPC and MULTIFLUX.

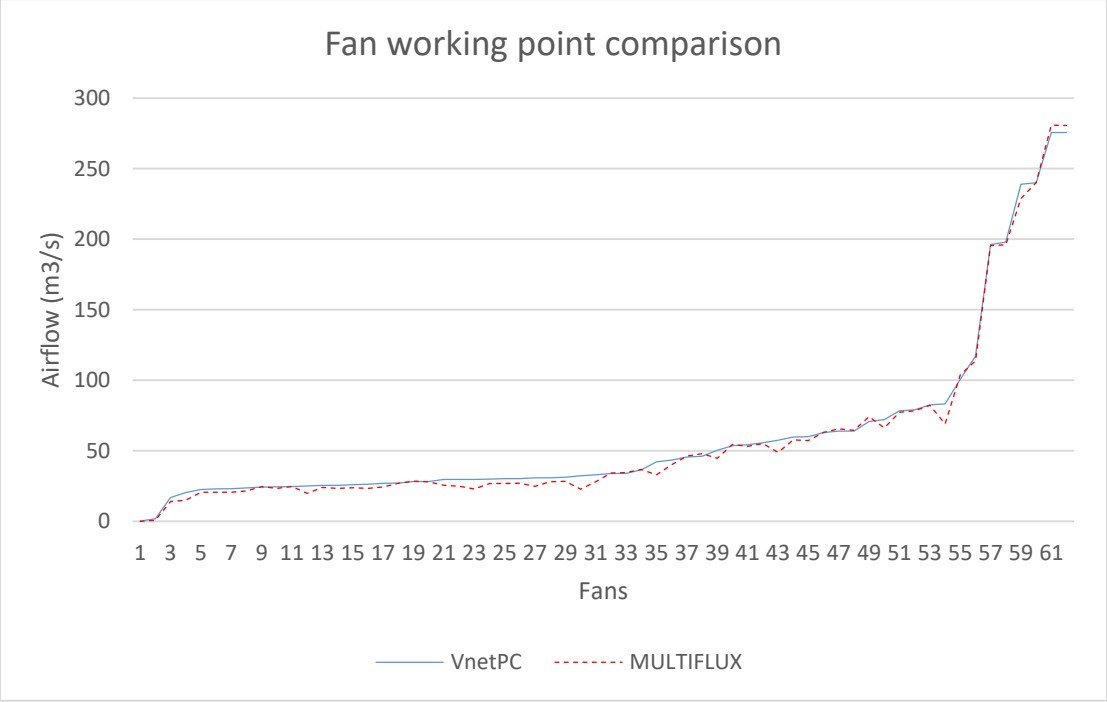


Figure A1-6. Fan airflow rate comparison between VnetPC and MULTIFLUX.

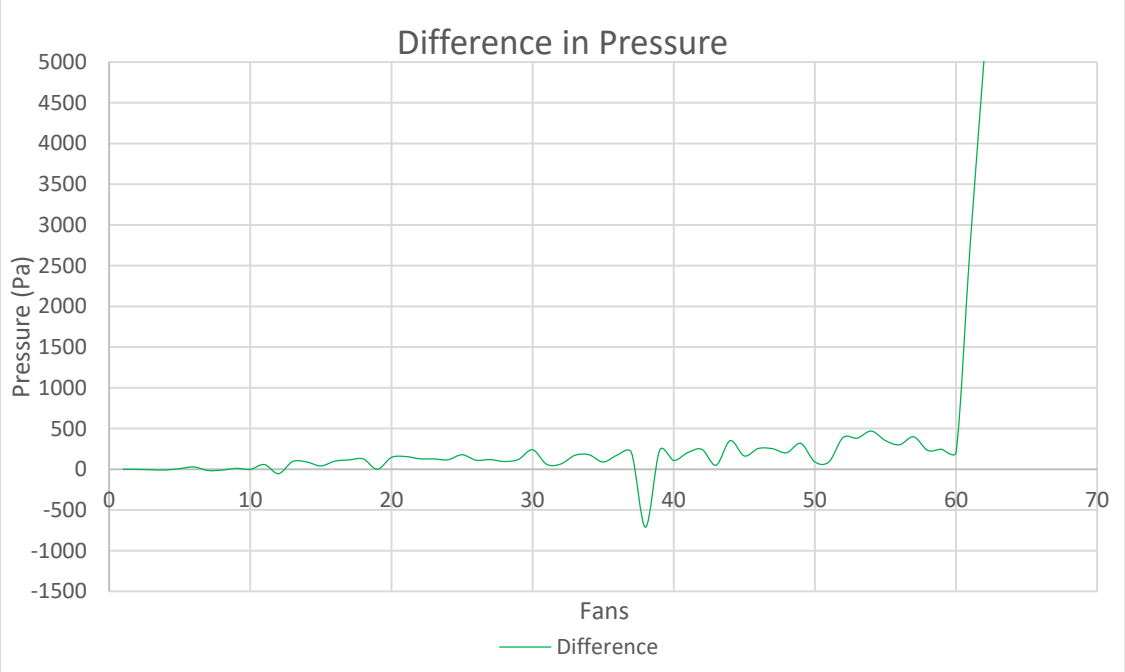


Figure A1-7. Fan pressure difference between VnetPC and MULTIFLUX.

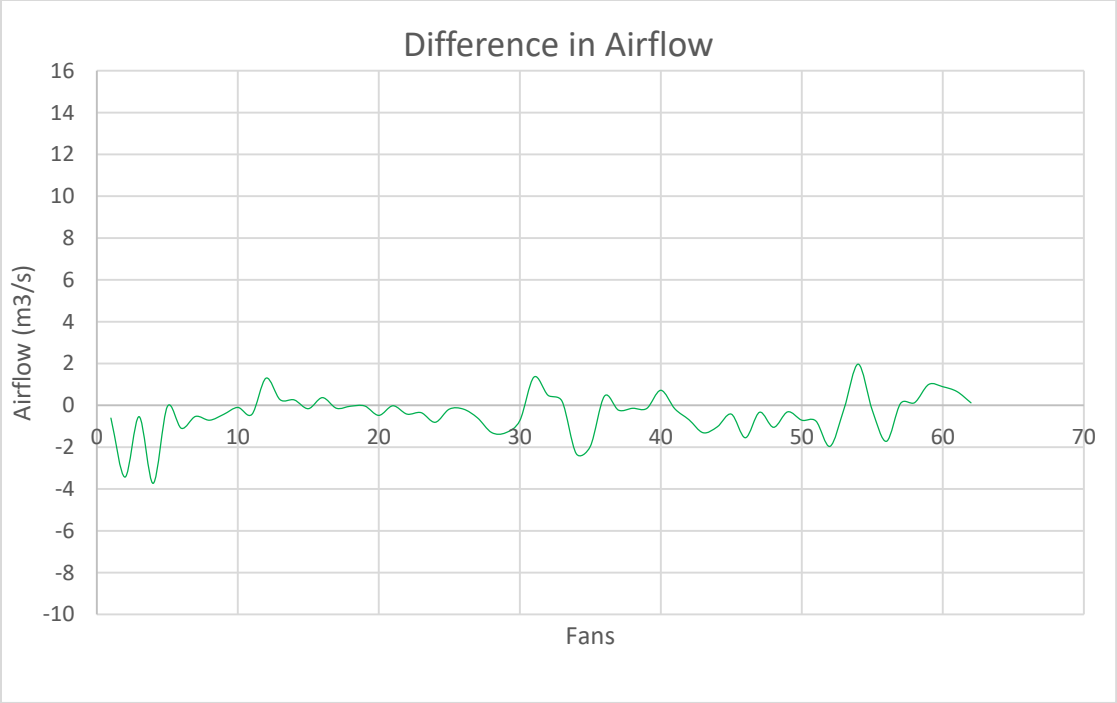


Figure A1-8. Fan airflow rate difference between VnetPC and MULTIFLUX.

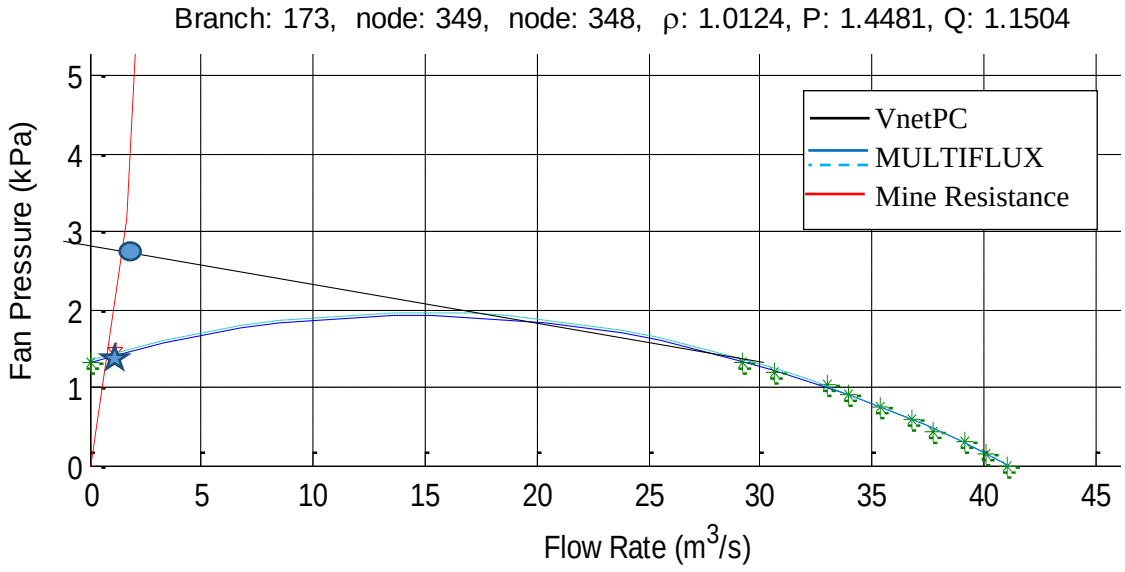


Figure A1-9. Fan curve comparison difference between VnetPC and MULTIFLUX for fan number 61.

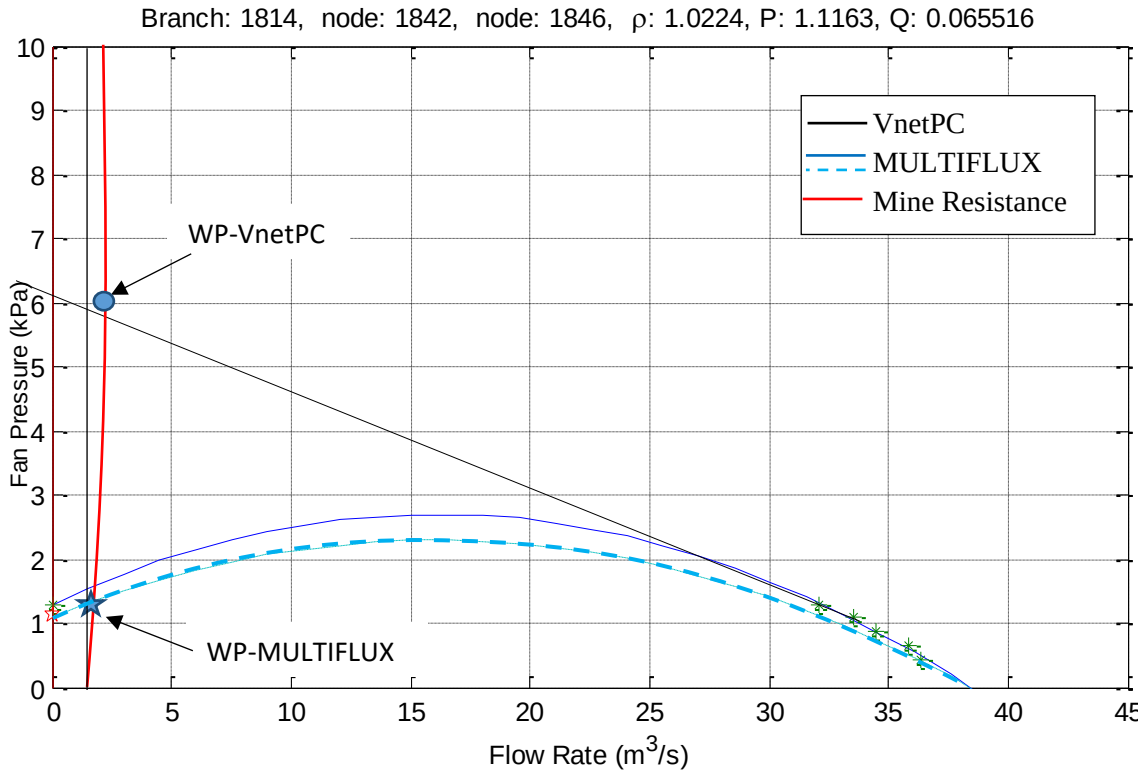


Figure A1-10. Fan curve comparison difference between VnetPC and MULTIFLUX for fan number 62.

**A1-3 Test example 3 for matching APPS model and VAM model for airflow predictions**

This model is a metal mine example from VnetPC which has 60 branches and one working fan. Figure A1-11 depicts the airflow differences between the VnetPC and MULTIFLUX models for mine example 3 (metal mine example from VnetPC). The difference in the average airflow between the models is 1.29m$^3$/s. Figure A1-12 demonstrates the fan working point's comparison between VnetPC and MULTIFLUX models. The difference in pressure and airflow are 6Pa and 2.99m$^3$/s, respectively, as illustrated in Figure A1-13.

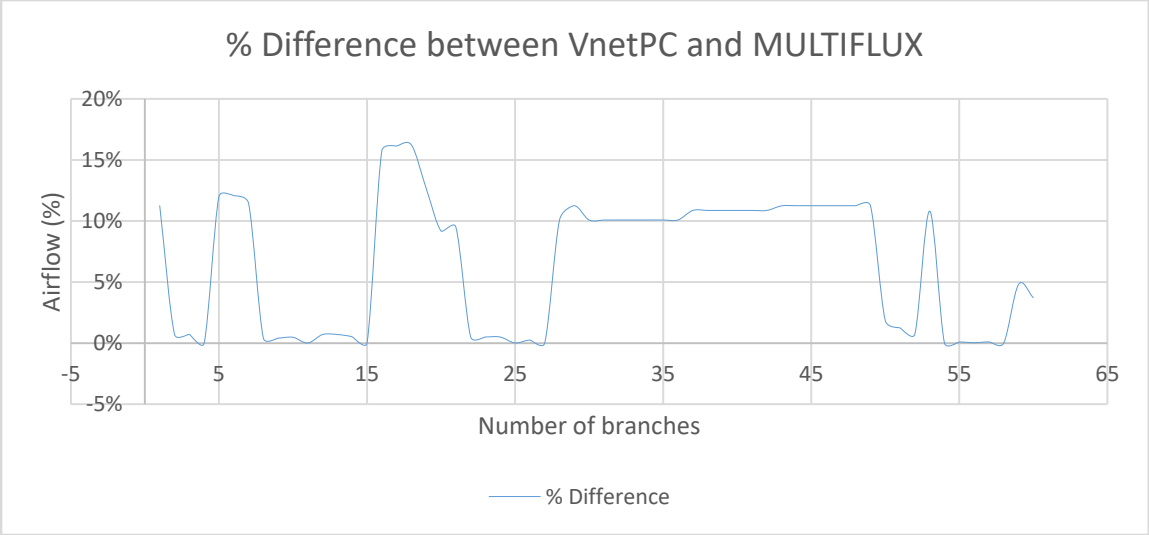


Figure A1-11. Airflow difference comparison between VnetPC and MULTIFLUX models for mine example 3 (metal mine example from VnetPC).

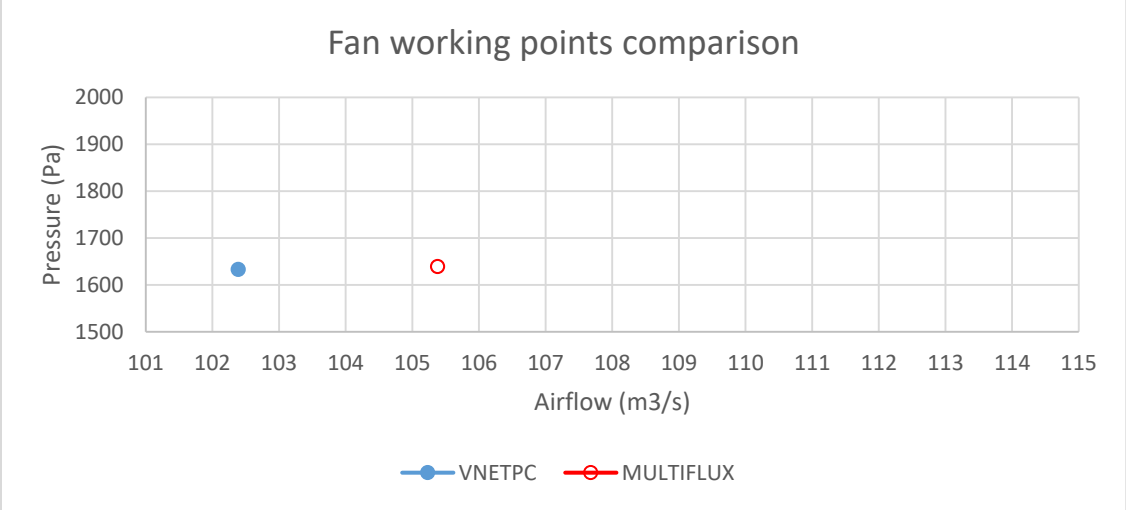


Figure A1-12. Fan working points comparison between VnetPC and MULTIFLUX models for mine example 3 (metal mine example from VnetPC).

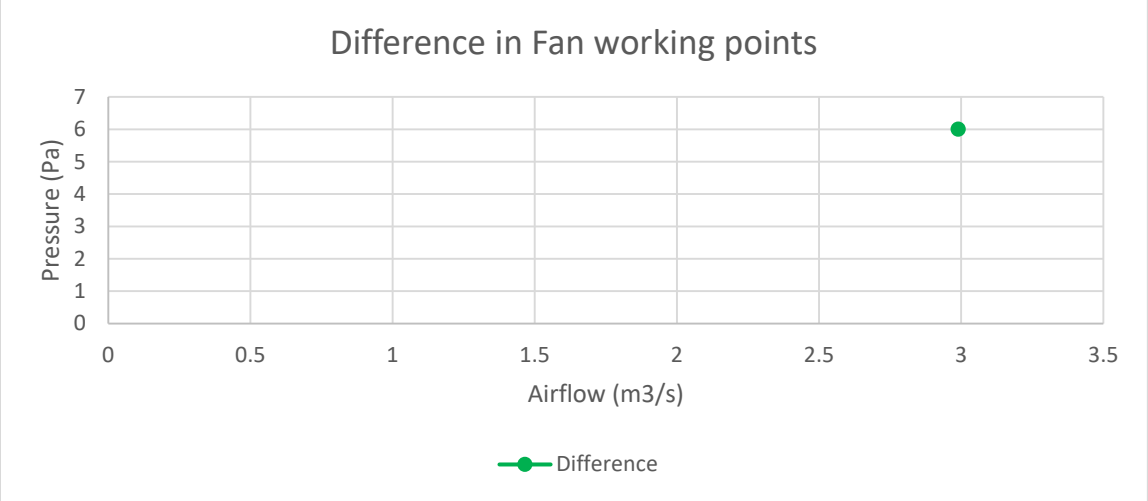


Figure A1-13. Difference in fan working points between VnetPC and MULTIFLUX models for mine example 3 (metal mine example from VnetPC).

**A1-4 Test example 4 for matching APPS model and VAM model for airflow predictions**

This model is a longwall coal mine from VnetPC which has 247 branches and 1 fan. Figure A1-14 shows the airflow differences between VnetPC and MULTIFLUX models. The difference in the average airflow between the models is 0.17$m^3$/s. The difference in the average pressures between the models is 4.8Pa. Figure A1-15 illustrates the fan working point's comparison between VnetPC and MULTIFLUX. The difference in pressure and airflow are 12.5Pa and 0.41$m^3$/s, respectively, as depicted in Figure A1-16.

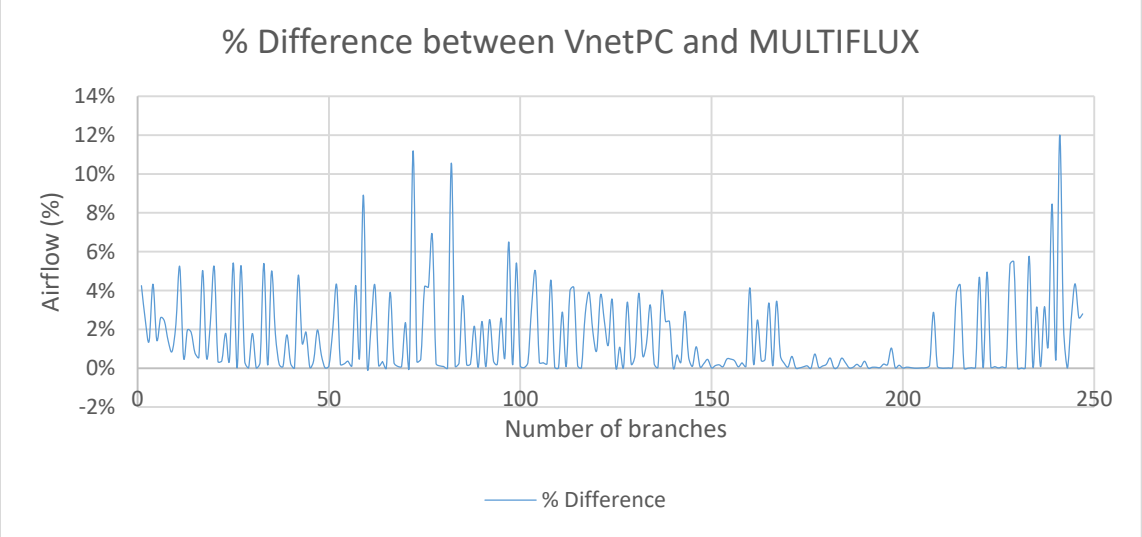


Figure A1-14. Airflow % difference comparison between VnetPC and MULTIFLUX models for mine example 4 (coal mine example from VnetPC).

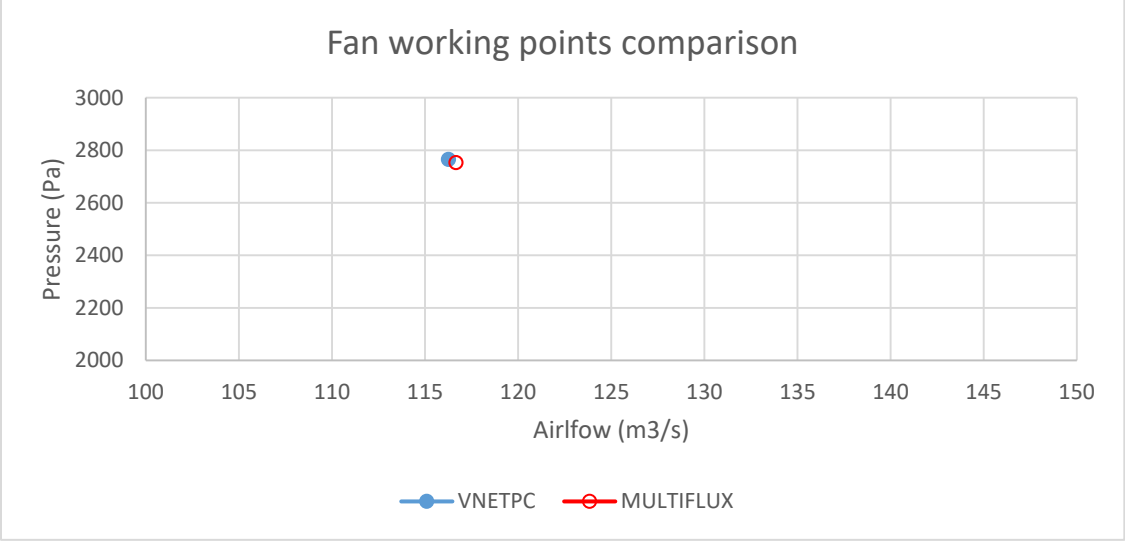


Figure A1-15. Fan working points comparison between VnetPC and MULTIFLUX for mine example 4 (coal mine example from VnetPC).

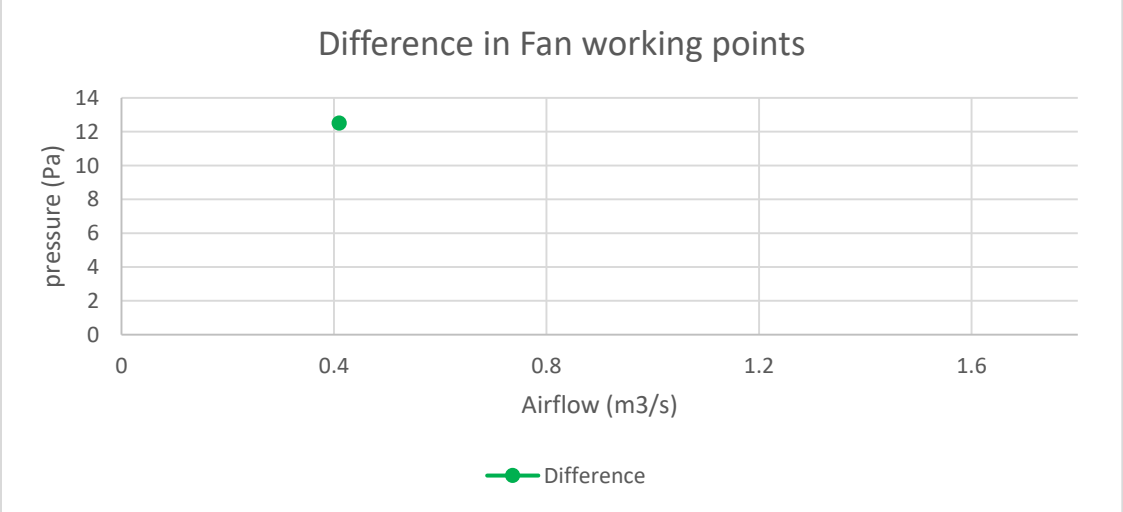


Figure A1-16. Difference for fan working points between VnetPC and MULTIFLUX for mine example 4 (coal mine example from VnetPC).

**A1-5 Test example 5 for matching APPS model and VAM model for airflow predictions**

This model is a metal mine which has 447 branches. It has two shafts, one for intake and one for exhaust with 3 working fans located underground. Figure A1-17 depicts the airflow differences between the Ventsim and MULTIFLUX models for mine example 5. The difference in the average airflow rate between the models is 0.17m$^3$/s. The difference in the average pressures between the models is 12.1Pa. Figure A1-18 shows the fan working

point's comparison between Ventsim and MULTIFLUX for the three fans. The maximum difference in pressure and airflow are 13.4Pa and 3.02m$^3$/s as illustrated in Figure A1-19. The difference can be attributed to the Ventsim fans being off-curve for small airflow rates.

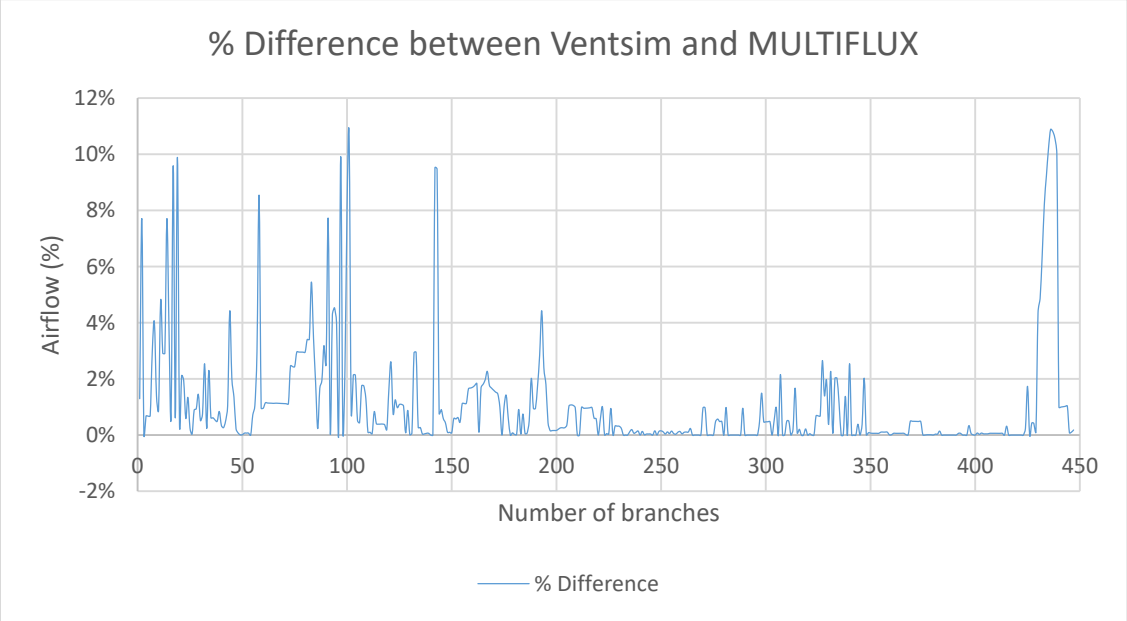


Figure A1-17. Airflow % difference comparison between Ventsim and MULTIFLUX models for mine example 5 (metal mine).

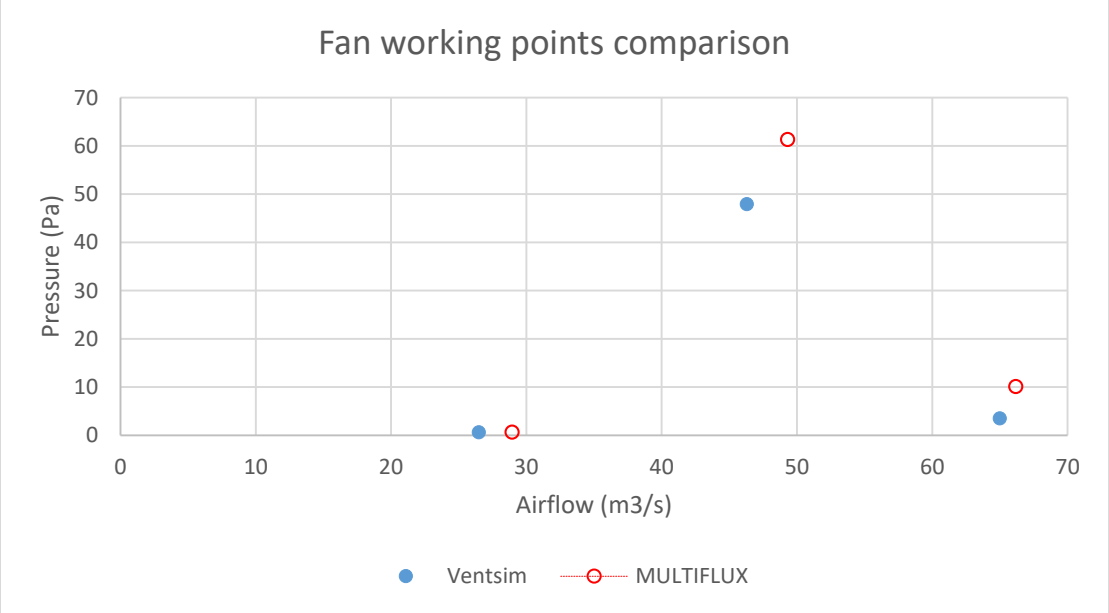


Figure A1-18. Fan working points comparison between Ventsim and MULTIFLUX models for mine example 5 (metal mine).

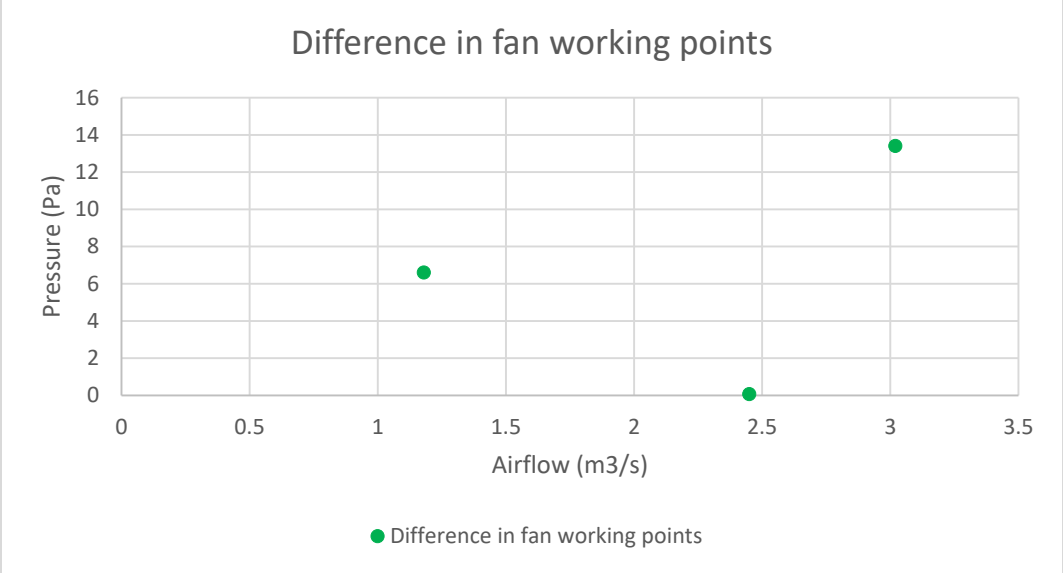


Figure A1-19. Difference for fan working points between Ventsim and MULTIFLUX models for mine example 5 (metal mine).

## Appendix 2. Examples of system properties identification

Figure A2.1 depicts a typical sensor data, X, over a period of 30 minutes, generated from a second order system, see Eq. (1), considered for proof of the concept and implemented as part of the EWP system to analyze the signal and system properties.

$$A_2^* \frac{\partial^2 X}{\partial t^2} + A_1^* \frac{\partial X}{\partial t} + A_0^* X = B \qquad (1)$$

Where $A_0^*$ , $A_1^*$, and $A_2^*$ are system properties; X is sensor data; *t* is time, and B is the constant. The Eq. (1) can be normalized to eliminate the need for constant *B*.

$$A_2 \frac{\partial^2 X}{\partial t^2} + A_1 \frac{\partial X}{\partial t} + A_O X = 1 \qquad (2)$$

Figures A2-2 and A2-3 demonstrate the first and second derivatives of the signal, respectively, revealing any linear and second order trends in the signal data. Figures A2-4 through A2-6 show the three system properties $A_0$, $A_1$, and $A_2$ of the system used in this example, respectively. The system constants are fairly unchanged until a disturbance causes a change in the system properties causing the system constants to be significantly different from the ordinary operating condition.

Figure A2-7 illustrates the signal used in the first exercise with a linear trend added. Figures A2-8 and A2-9 show the first and second derivatives of the signal, respectively, revealing any linear and second order trends in the signal data. The linear trend can be detected by the average first derivative curve being nearly constant positive indicating positive slope in the trend. Figures A2-10 through A2-12 depicts the three system constants $A_0$, $A_1$, and $A_2$ of the system used in this example. The system constants are fairly

unchanged until a disturbance causes a change in system properties causing the system constants to be significantly different from the ordinary operating condition.

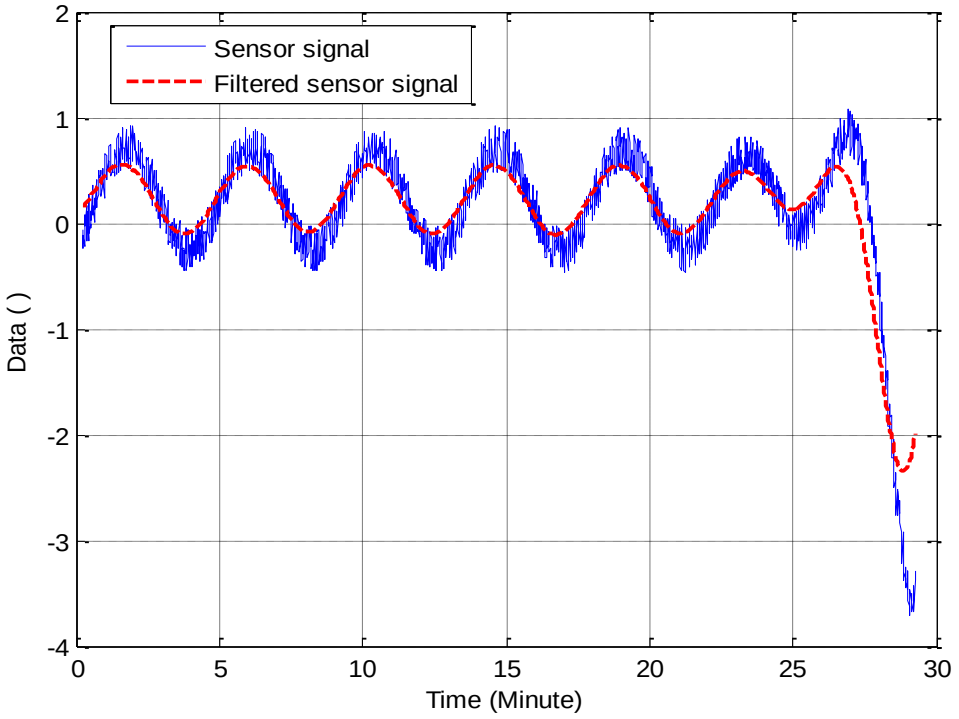


Figure A2-1. Signal data together with the filtered data.

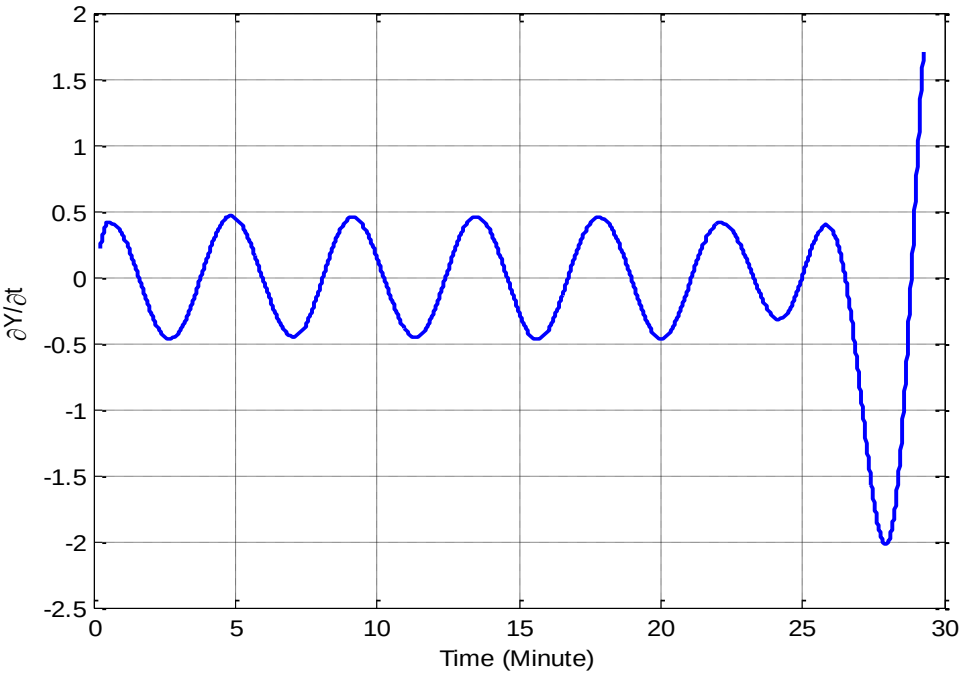


Figure A2-2. Signal data first derivative.

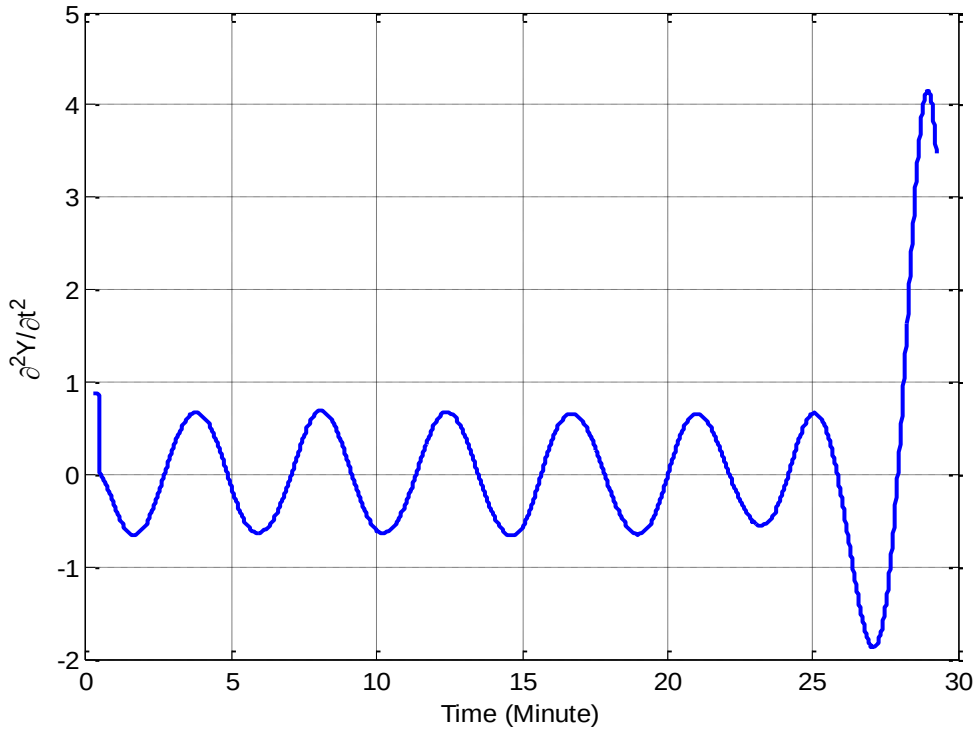


Figure A2-3. Signal data second derivative.

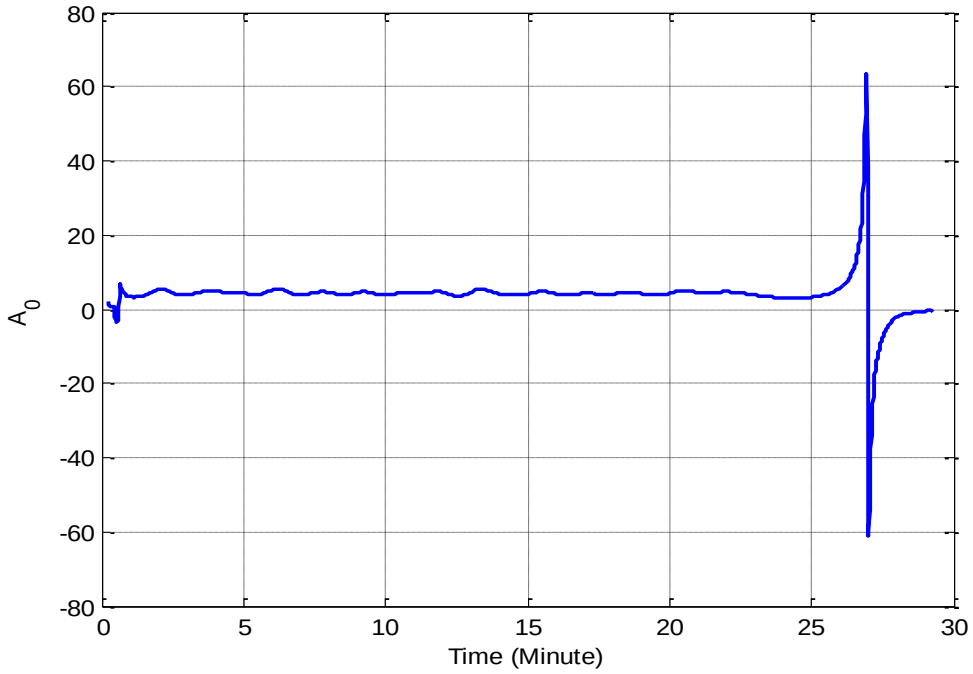


Figure A2-4. Signal system properties, $A_0$ constant.

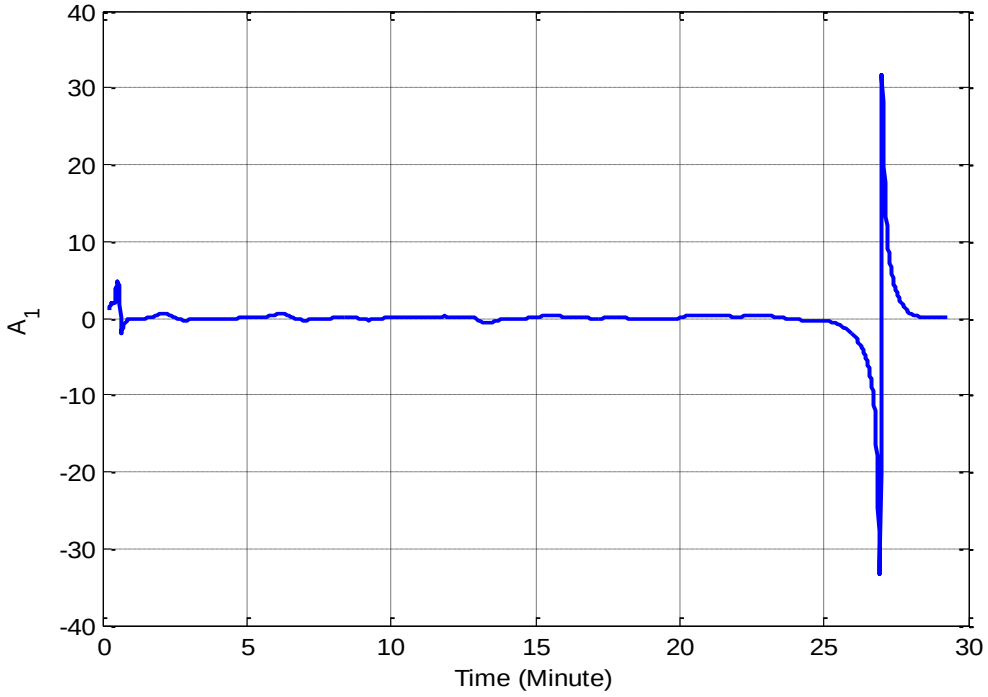


Figure A2-5. Signal system properties, $A_1$ constant.

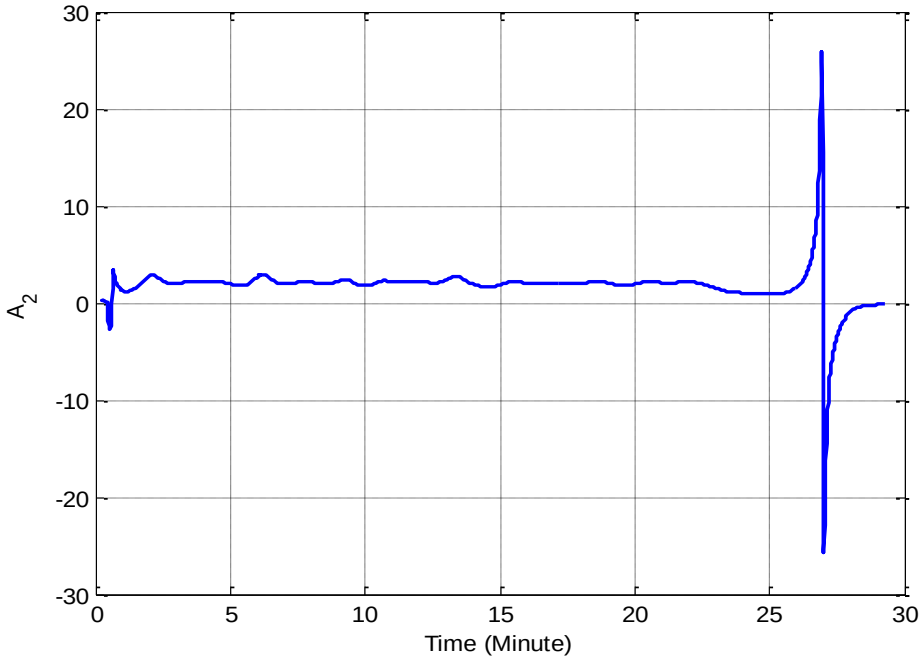


Figure A2-6. Signal system properties, $A_2$ constant

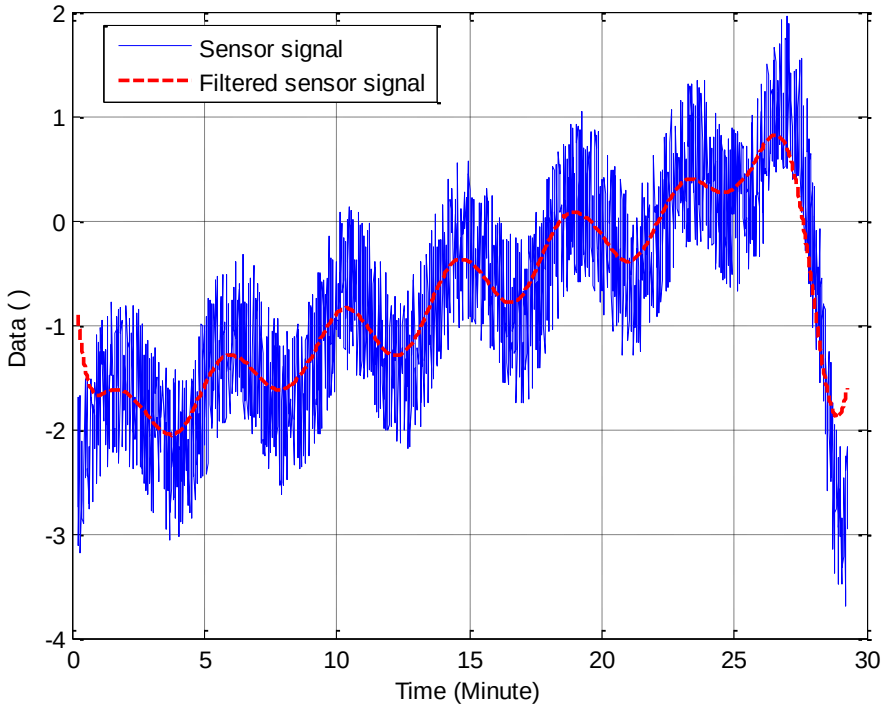


Figure A2-7. Signal data together with the filtered data.

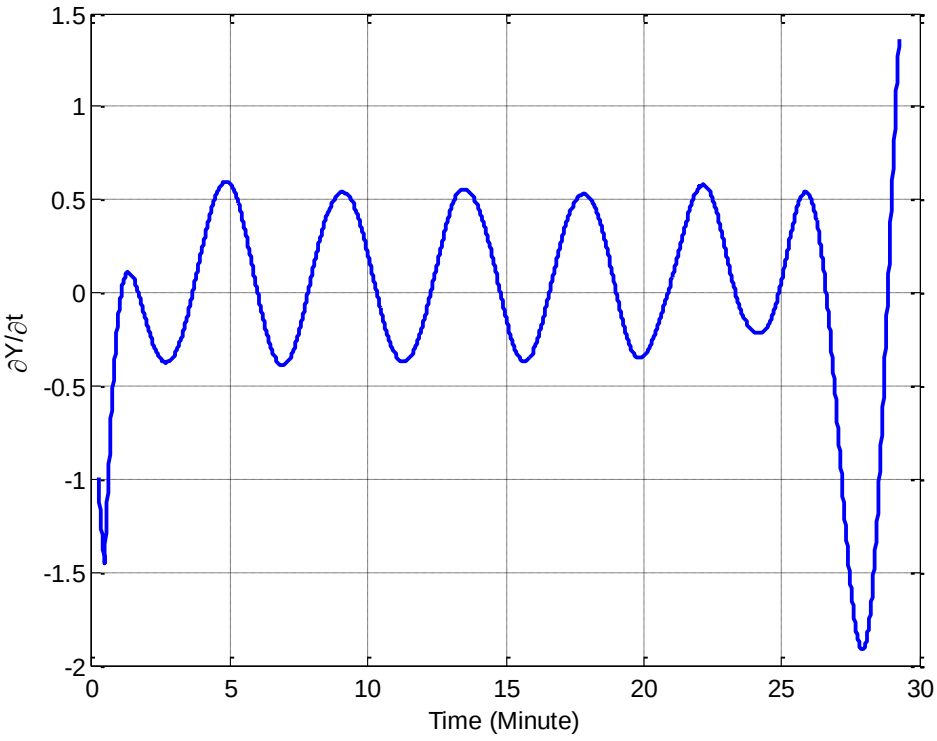


Figure A2-8. Signal data first derivative.

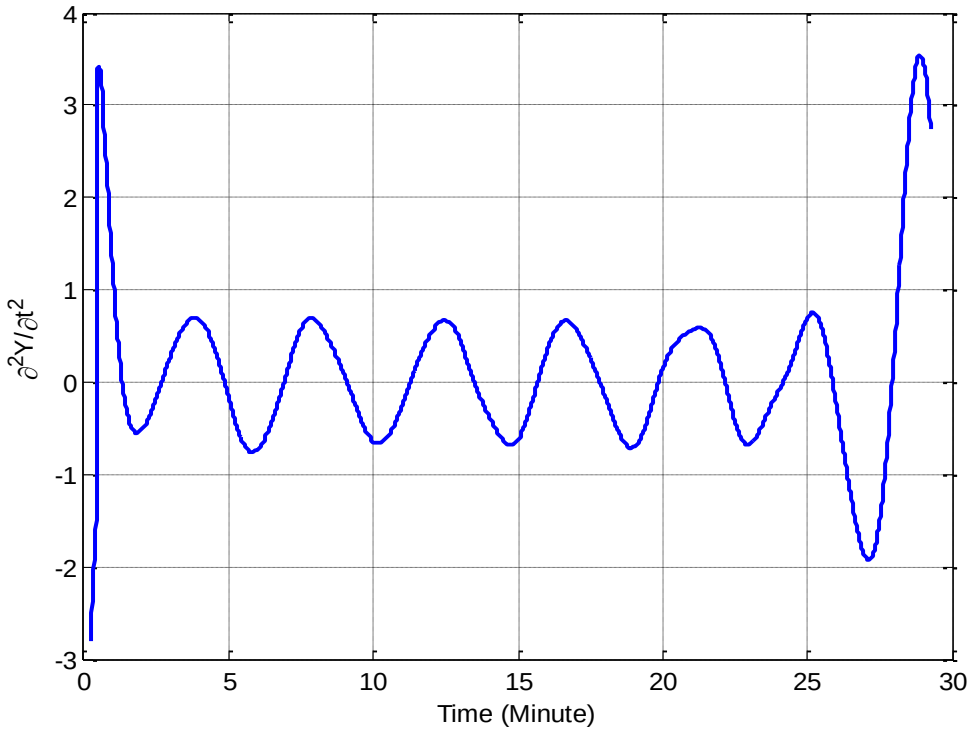


Figure A2-9. Signal data second derivative.

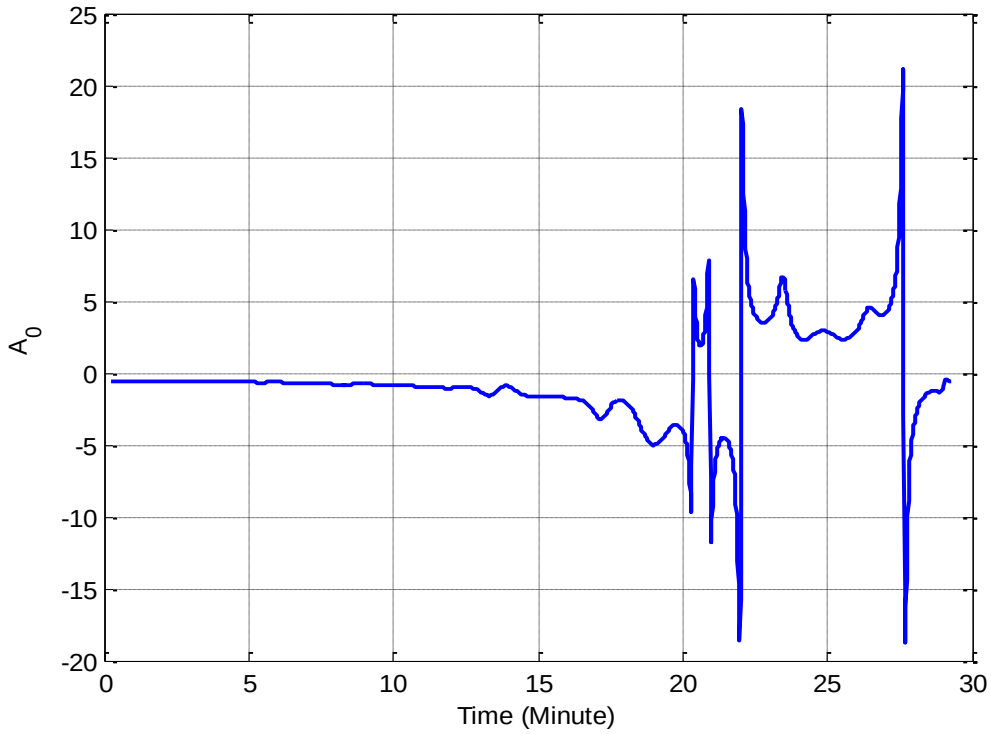


Figure A2-10. Signal system properties, $A_0$ constant.

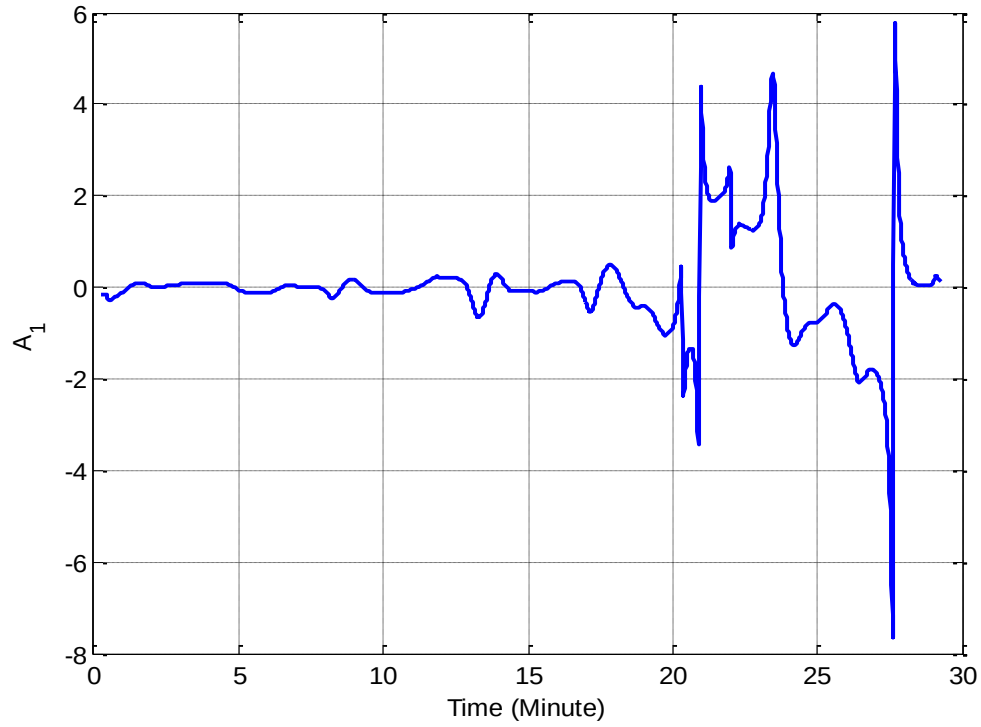


Figure A3. A2-11. Signal system properties, $A_1$ constant.

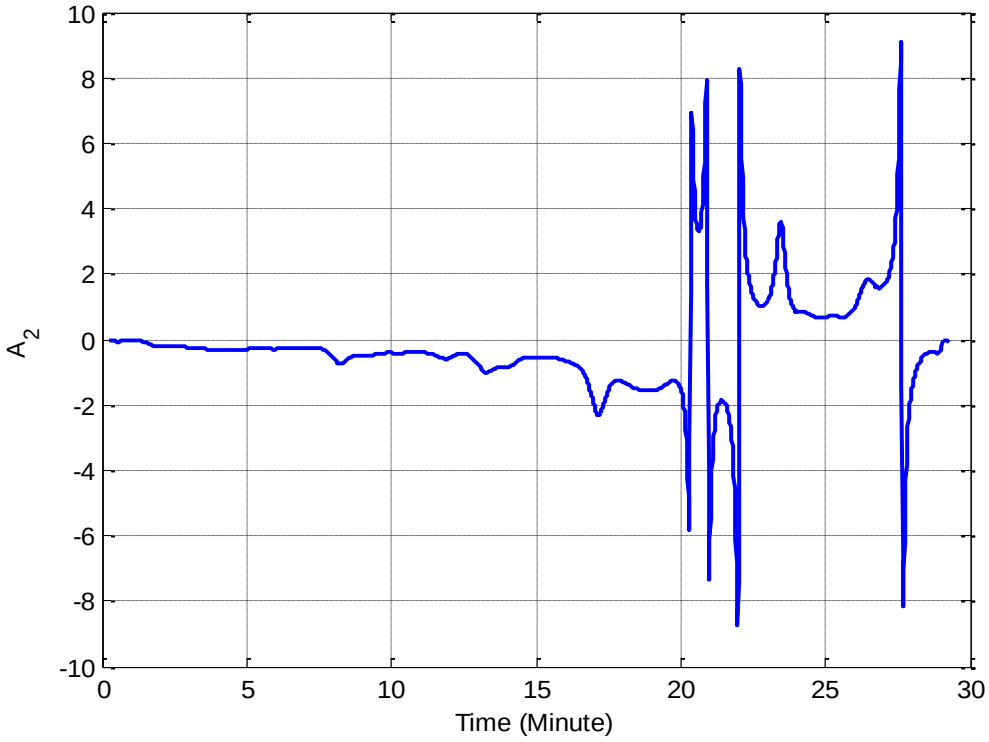


Figure A2-12. Signal system properties, $A_2$ constant.

## Appendix 3. Atmospheric barometric pressure variations effects on methane inflow

A large volume of porous and fractured methane coal seam under pressure variations, shown in Figure A3-1, may release a large amount of methane by Darcy flow. Gob, strata, and partially sealed off dead zones, are examples of such a volume. Figures A3-2 and A3-3illustrate the layout of longwall section and the 3D section of the gob as one of the example of such situation. Half of the gob size contains a volume of 240,000 $m^3$ methane. The barometric pressure changes induce flow of air in and out of the gob called barometric pressure pumping as depicted in Figure A3-4. This is modeled in the MULTIFLUX gob model and it establishes a methane concentration profile demonstrated in Figures A3-5 and A3-6. Darcy flow moves methane in and out of the gob and mixes air and methane inside the gob. The MULTIFLUX Air-$CH_4$ flow model shows that the mixing process results in a gradual methane profile close to linear and this is indicated in Figure A3-7. The effect of this scenario is the liberation of gas mixing into the air resulting in methane concentration increase which may cross threshold value. The root cause of pressure variations may be detected from outside barometric pressure decrease, pressure decrease in the airway or blockage of airway.

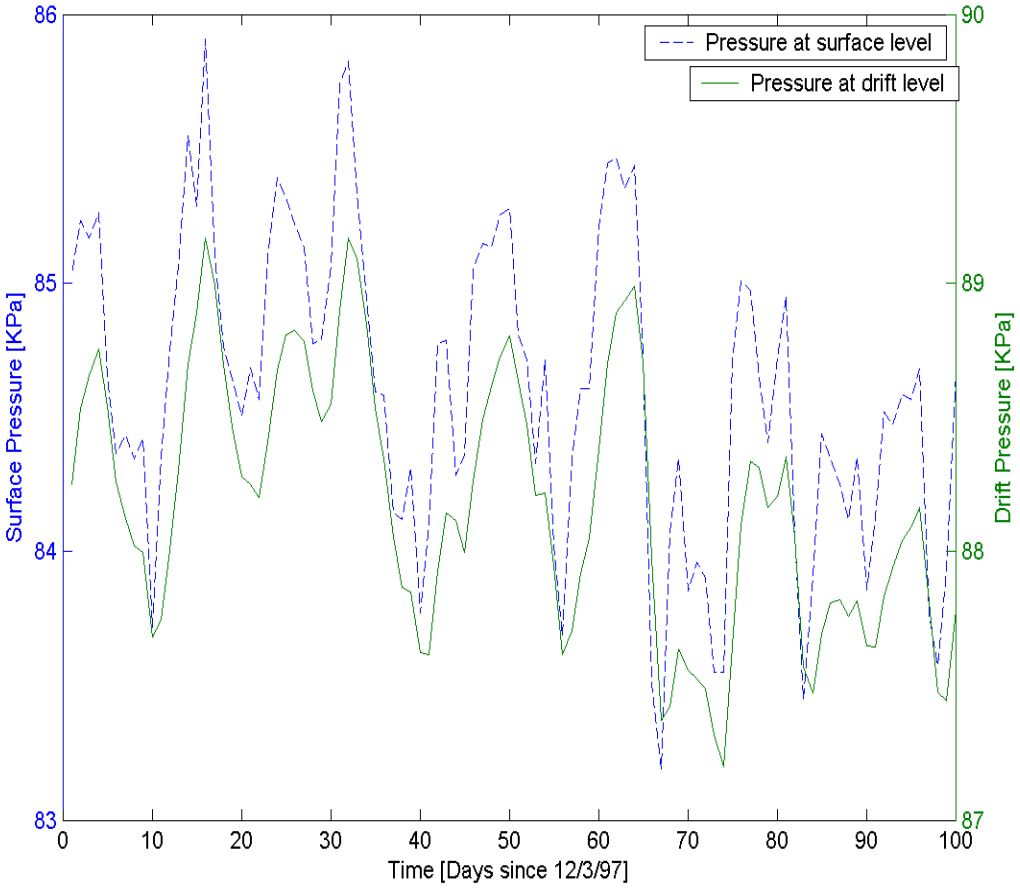


Figure 3-1. Typical Barometric Pressure, Pb, variation in Nevada (Danko et al, 2013).

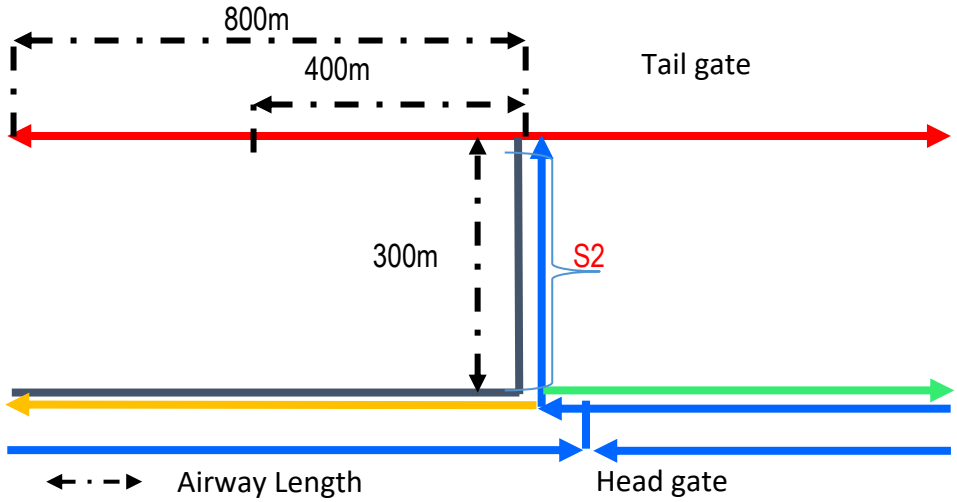


Figure A3-2. Layout of the longwall.

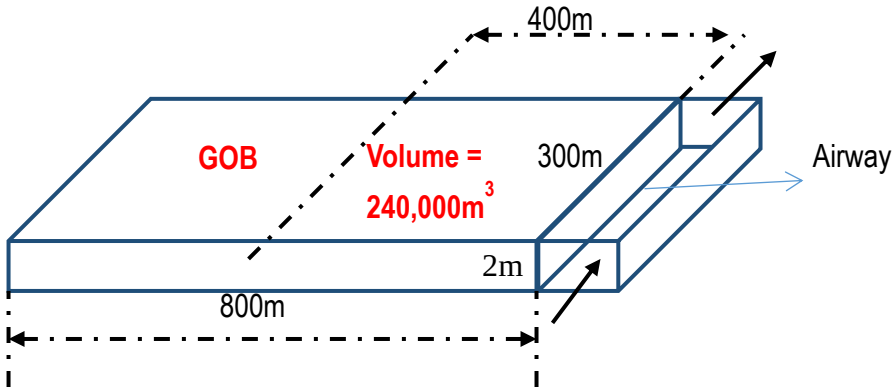


Figure A3-3. 3D section of the Gob.

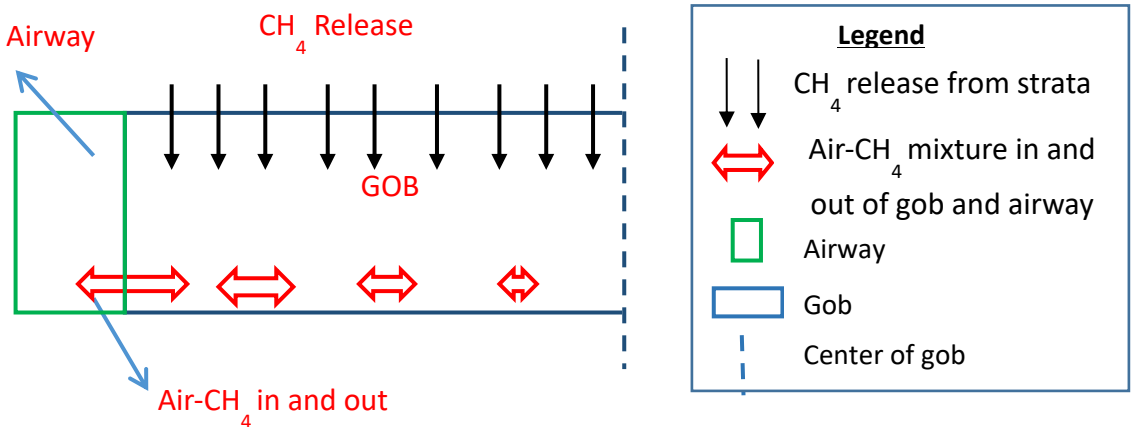


Figure A3-4. Layout of flow of Air-$CH_4$ mixture in and out of the airway due to barometric pressure drop.

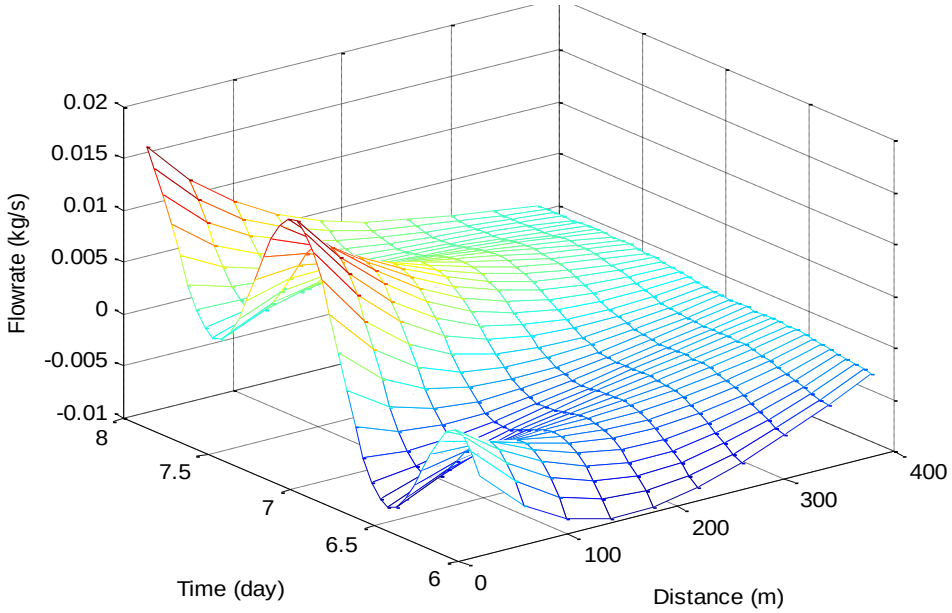


Figure A3-5. 3D Flow of Air- $CH_4$ mixture in and out of the airway.

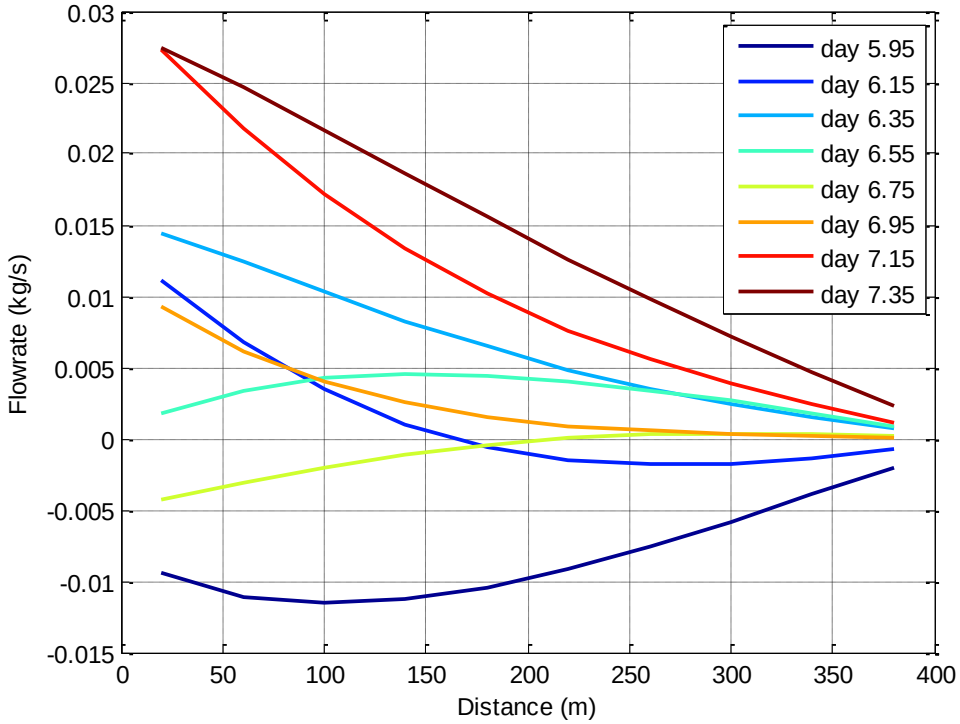


Figure A3-6. 2D Flow profile of Air- $CH_4$ mixture in and out of the airway for selected time divisions.

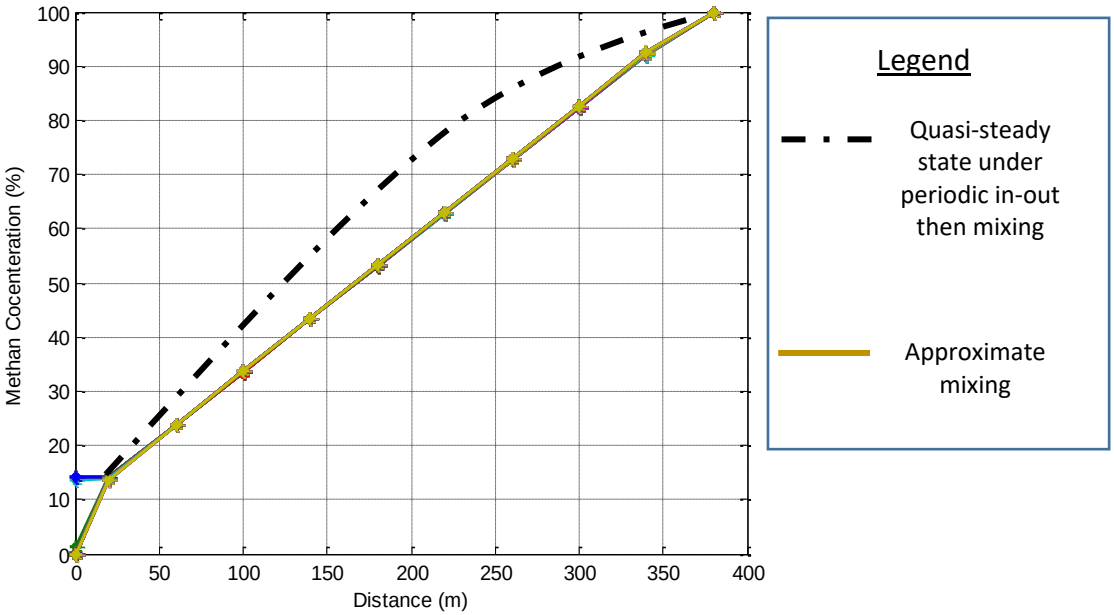


Figure A3-7. Methane concentration profile from Air-$CH_4$ mixing in the gob.

## Appendix 4. Fan characteristics in fan malfunctioning scenario

The base points of the fan characteristics used in the scenario are given in table A4-1.

Table A4-1 Fan points.

| ORIGINAL | | REDUCED | |
|---|---|---|---|
| Quantity ($m^3/s$) | Fan static pressure (Pa) | Quantity ($m^3/s$) | Fan static pressure (Pa) |
| 50 | 7500 | 50 | 3675 |
| 55 | 7000 | 55 | 3430 |
| 60 | 6500 | 60 | 3185 |
| 65 | 6000 | 65 | 2940 |
| 70 | 5500 | 70 | 2695 |
| 75 | 5000 | 75 | 2450 |
| 79.9 | 4484 | 79.9 | 2197.16 |
| 85 | 4000 | 85 | 1960 |
| 90 | 3500 | 90 | 1715 |
| 95 | 3000 | 95 | 1470 |

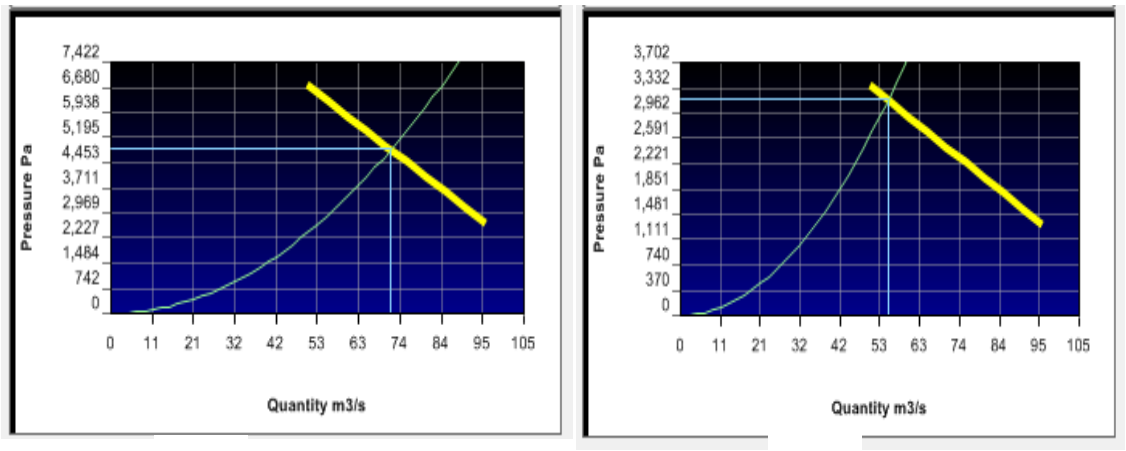


(a) (b)

Figure A4-1. Fan curves for original (a) and reduced (b) fan points.

## Appendix 5. Fan power comparison

### A5-1. Comparison of fan power for scenarios 1A, 1B, 2, and 3 modeled in example 1.

Table A5-1 shows the comparison between the fan powers for the various scenarios modeled in mine example 1. The table indicates that there is no difference between the fan power for scenarios 1A and 1B. There is a slight increase in the fan power for scenario 2 compared to the Base scenario 1A. The fan power of scenario 3 decreases slightly compared to the Base scenario 1A. Therefore, fan power measurements are conclusive only in the case of the fan malfunction.

Table A5-1. Fan power for various scenarios modeled in mine example 1.

| | Base Scenario 1A-2 sources | | Scenario 1B-3 sources | | Scenario 2-airway blockage | | Scenario3-Pressure drop2000Pa | |
|---|---|---|---|---|---|---|---|---|
| Fan ID | shaft Power | electrical Power | shaft Power | electrical Power | shaft Power | electrical Power | shaft Power | electrical Power |
| | (kW) | (kW) | (kW) | (kW) | (kW) | (kW) | (kW) | (kW) |
| 319 | 1864.5 | 1962.6 | 1864.5 | 1962.7 | 1867.2 | 1965.5 | 1836.8 | 1933.4 |
| 313 | 582.5 | 613.2 | 582.5 | 613.1 | 582.6 | 613.2 | 568.9 | 598.8 |
| 308 | 532.3 | 560.3 | 532.3 | 560.3 | 535.5 | 563.7 | 524.7 | 552.3 |

### A5-2 Comparison of fan power for scenarios 1C, 4, and 5 modeled in example 2.

Table A5-2 shows the fan power for various scenarios modeled in mine example 2. There is a slight increase in the fan power for scenario 5 compared to the Base scenario 1C. The fan power of scenario 4 for the fan with reduced rpm (fan ID=230) decreases significantly compared to the Base scenario 1C.

Table A5-2. Fan power for various scenarios modeled in mine example 2.

| Fan ID | Base Scenario 1C- 3 sources | | Scenario 4-fan malfunction | | Scenario 5- belt fire | |
|---|---|---|---|---|---|---|
| | shaft Power | electrical Power | shaft Power | electrical Power | shaft Power | electrical Power |
| | (kW) | (kW) | (kW) | (kW) | (kW) | (kW) |
| 234 | 444.3 | 467.7 | 434.9 | 457.8 | 458.8 | 483 |
| 230 | 469.9 | 494.6 | 253.4 | 266.7 | 486.1 | 511.7 |

**Appendix 6. Laboratory analytical request form**

1401437

DATA CHEM LABORATORIES INC (ALS)

ALS Laboratory Group
ANALYTICAL CHEMISTRY & TESTING SERVICES
Environmental Division

# ANALYTICAL REQUEST FORM 1401437

1. [X] REGULAR Status

[ ] RUSH Status Requested - ADDITIONAL CHARGE
RESULTS REQUIRED BY _____ DATE
CONTACT ALS DATACHEM LABS PRIOR TO SENDING SAMPLES

Date: 01/10/2014 Purchase Order No. CC (Bahrami)

3. Company Name University of Nevada, Reno
Address 1664 N. Virginia Street
Reno, NV 89557. MS/0173
Person to Contact DAVOOD BAHRAMI
Telephone 775-527-8403
Fax Telephone
E-mail Address dbahrami@unr.edu
Billing Address (if different from above)

4. Quote No.
ALS Project Manager Rand Potter

5. Sample Collection
Sampling Site: Barrick Goldstrike
Industrial Process
Date of Collection: 1/8/2014 & 1/9/2014
Time Collected: 3:00pm - 5:00pm (1/8/2014)
11:30am - 1:00pm (1/9/2014)
Chain of Custody No.

6. How did you first learn about ALS DataChem?
From SKC website.

7. REQUEST FOR ANALYSES

| Laboratory Use Only | Client Sample Number | Matrix* | Sample Volume | ANALYSES REQUESTED - Use method number if known | Units** |
|---|---|---|---|---|---|
| | A120306 | DPM | 0.000 | NIOSH 5040 | 5 |
| | A120332 | DPM | 205.020 | NIOSH 5040 | 5 |
| | A120364 | DPM | 145.160 | NIOSH 5040 | 5 |
| | A120359 | DPM | 204.840 | NIOSH 5040 | 5 |
| | A120292 | DPM | 199.444 | NIOSH 5040 | 5 |
| | A120263 | DPM | 202.836 | NIOSH 5040 | 5 |
| | A120352 | DPM | 201.544 | NIOSH 5040 | 5 |
| | A120325 | DPM | 207.179 | NIOSH 5040 | 5 |
| | A120373 | DPM | 204.66 | NIOSH 5040 | 5 |
| | A120354 | DPM | 164.832 | NIOSH 5040 | 5 |
| | A117499 | DPM | 161.738 | NIOSH 5040 | 5 |
| | A117474 | DPM | 164.880 | NIOSH 5040 | 5 |
| | A117516 | DPM | 160.313 | NIOSH 5040 | 5 |
| | | | | | |
| | | | | | |

** 1. µg/sample 2. mg/m³ 3. ppm 4. % 5. µg/m³ 6. ____ (other) Please indicate one or more units in the column entitled Units**

Comments **Please send results to both emails:** dbahrami@unr.edu
eponition@yahoo.com and kgrandy@barrick.com

Possible Contamination and/or Chemical Hazards

7. Chain of Custody (Optional)

| | | | |
|---|---|---|---|
| Relinquished by | Gwilliam Asante | Date/Time | 01/10/2014 |
| Received by | [signature] | Date/Time | 01-14-14 0953 |
| Relinquished by | | Date/Time | |
| Received by | | Date/Time | |

960 West LeVoy Drive / Salt Lake City, UT 84123 800-356-9135 or 801-266-7700 / FAX: 801-268-9992